



**UNIVERSIDAD NACIONAL AUTÓNOMA DE MEXICO**  
Posgrado en Ciencias Físicas

Cosmología

RECONSTRUCTING THE DARK ENERGY

TESIS  
QUE PARA OPTAR POR EL GRADO DE:  
DOCTOR EN CIENCIAS (FÍSICA)

PRESENTA:  
LUIS ADRIÁN ESCAMILLA TORRES

TUTOR PRINCIPAL:  
DR. JOSÉ ALBERTO VÁZQUEZ GONZÁLEZ  
ICF, UNAM.

MIEMBROS DEL COMITÉ TUTOR:  
DR. JUAN CARLOS HIDALGO CUÉLLAR, ICF.  
DR. CÉSAR FERNÁNDEZ RODRÍGUEZ, ICN.

LUGAR, MES Y AÑO EN QUE SE REALIZÓ EL EXAMEN:  
ICF-UNAM, MARZO, 2024



# UNIVERSIDAD NACIONAL AUTÓNOMA DE MÉXICO

## PROGRAMA DE POSGRADO EN CIENCIAS FÍSICAS

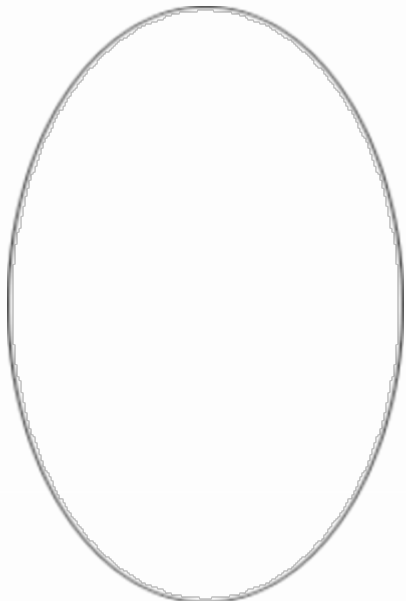
En la Universidad Nacional Autónoma de México, a través de un **AULA VIRTUAL UNIVERSITARIA**, a las **11:00** horas del día 18 de abril de 2024, el alumno de nacionalidad mexicana

### LUIS ADRIÁN ESCAMILLA TORRES

cuya fotografía aparece al margen, se presentó con el fin de sustentar el examen para obtener el grado de

### ACTA DE GRADO

No. de cuenta  
**520014079**



### DOCTOR EN CIENCIAS (FÍSICA)

en la modalidad de graduación por **TESIS**, con el trabajo titulado: **Reconstructing the Dark Energy**, del cual fue tutor principal el **DR. JOSÉ ALBERTO VÁZQUEZ GONZÁLEZ**.

El alumno cursó sus estudios en el período **2020-1** a **2023-2**, y cumplió con los requisitos académicos señalados en el plan de estudios **5204** aprobado por el Consejo Universitario.

El jurado resolvió otorgarle la calificación de

le hizo saber el resultado de su examen y le tomó la Protesta Universitaria.

El jurado estuvo integrado por:

**Presidenta:** Dra. Mariana Vargas Magaña

**Secretario:** Dr. José Alberto Vázquez González

**Vocal 1:** Dr. Alejandro Avilés Cervantes

**Vocal 2:** Dr. Jorge Luis Cervantes Cota

**PRESIDENTA DEL JURADO**

**VOCAL 1 DEL JURADO**

**VOCAL 2 DEL JURADO**

**SECRETARIO DEL JURADO**

El suscrito coordinador del programa constató que las firmas corresponden al jurado designado

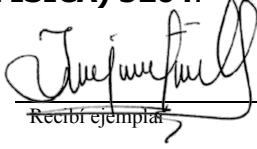
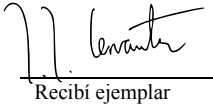



No. Folio del Programa  
5204092012430

**"POR MI RAZA HABLARÁ EL ESPÍRITU"**  
**DR. ALBERTO GÚIJOSA HIDALGO**  
**COORDINADOR DEL PROGRAMA**



**Estimado (a) Colega:**

El **Comité Académico** del **Posgrado en Ciencias Físicas** en sesión del **28 de noviembre de 2023** ha designado como Jurado del alumno **Luis Adrián Escamilla Torres**, con número de cuenta **520014079** para dictaminar si el trabajo desarrollado como Tesis Titulada: **"Reconstructing the Dark Energy"**, dirigida por el Dr. José Alberto Vázquez González, tiene los méritos para realizar el Examen al Grado de **DOCTOR EN CIENCIAS (FÍSICA)** conforme al Plan de Estudios de **DOCTORADO EN CIENCIAS (FÍSICA) 5204**.

<b>Propietario:</b>	Dr. José Alberto Vázquez González	 Recibí ejemplar	8-12-2023 fecha
<b>Propietario:</b>	Dr. Jorge Luis Cervantes Cota	 Recibí ejemplar	8-12-2023 fecha
<b>Propietario:</b>	Dra. Mariana Vargas Magaña	 Recibí ejemplar	8-12-2023 fecha
<b>Propietario:</b>	Dr. Tonatiuh Matos Chassin	 Recibí ejemplar	30-01 fecha
<b>Propietario</b>	Dr. Alejandro Avilés Cervantes	 Recibí ejemplar	8-12-2023 fecha

**ATENTAMENTE**  
**"POR MI RAZA HABLARÁ EL ESPÍRITU"**  
Ciudad Universitaria, Cd. Mx., a 05 de Diciembre de 2023.

**EL COORDINADOR**

**DR. ALBERTO GÚIJOSA HIDALGO**



**PROTESTA UNIVERSITARIA DE INTEGRIDAD Y  
HONESTIDAD ACADÉMICA Y PROFESIONAL  
(Graduación con trabajo escrito)**

De conformidad con lo dispuesto en los artículos 87, fracción V, del Estatuto General, 68, primer párrafo, del Reglamento General de Estudios Universitarios y 26, fracción I, y 35 del Reglamento General de Exámenes, me comprometo en todo tiempo a honrar a la Institución y a cumplir con los principios establecidos en el Código de Ética de la Universidad Nacional Autónoma de México, especialmente con los de integridad y honestidad académica.

De acuerdo con lo anterior, manifiesto que el trabajo escrito titulado:

**"Reconstructing the Dark Energy"**

que presenté para obtener el grado de ----Doctorado---- es original, de mi autoría y lo realicé con el rigor metodológico exigido por mi programa de posgrado, citando las fuentes de ideas, textos, imágenes, gráficos u otro tipo de obras empleadas para su desarrollo.

En consecuencia, acepto que la falta de cumplimiento de las disposiciones reglamentarias y normativas de la Universidad, en particular las ya referidas en el Código de Ética, llevará a la nulidad de los actos de carácter académico administrativo del proceso de graduación.

Una firma manuscrita en tinta negra, que parece ser la del Sr. Luis Adrián Escamilla Torres.

**Atentamente**

Luis Adrián Escamilla Torres  
Número de cuenta: 520014079

**(Nombre, firma y Número de cuenta de la persona alumna)**



# Agradecimientos

Quiero comenzar expresando mi gratitud a las personas sin las cuales esto no hubiera sido posible: mis padres y hermanos. Su constante apoyo, independientemente de la distancia, siempre ha estado presente, y sé que seguirá estándolo sin importar la decisión que tome sobre mi futuro en el mundo de la ciencia.

Al profe Beto, quien nunca dejó de creer en mí desde mi maestría. Ha sido un asesor excepcional, siempre ve por sus alumnos y muchas veces ha brindado apoyo más allá de lo que sus deberes como asesor exigían. Estoy seguro de que seguiremos colaborando a futuro. A todos mis colegas académicos y compañeros de cuarto: Padilla, Isidro, Jazhiel, Tadeo, Gabriela, Ian, Prado y Pedro. Más que simples compañeros de piso ó de trabajo temporales, los considero amistades que trascienden lo académico. A mis amigos LA y Chris que sé que puedo contar con ellos y me lo han demostrado desde que nos conocimos. A mis amigos y familia en Nuevo León, quienes, sin importar cuánto tiempo pase, sé que seguirán estando allí para recibirme como si nunca me hubiera ido. A los profesores y personal de la UNAM que siempre se han mostrado amables a la hora de enseñar y ayudar.

Al profesor Özgür, con quien he colaborado en numerosas ocasiones y quien siempre ha mostrado paciencia y una extraordinaria disposición. A la Dra. Eleonora, por haberme permitido realizar una estancia con ella y por su amabilidad constante, siempre mostrando una sonrisa y su disposición para ayudarme más allá de lo que le correspondía. También por mostrarme que aún tengo mucho camino por recorrer en el ámbito académico.

Por último agradezco al Consejo Nacional de Humanidades, Ciencias y Tecnologías (CONAH-CyT) por el apoyo durante mi doctorado. También agradezco al proyecto del PAPIIT “Cosmología observacional y estadística de la energía oscura” por el apoyo a la obtención de mi grado académico y al Programa de Apoyo a Proyectos de Investigación e Innovación Tecnológica (PAPIIT) de la UNAM IN117723.



# Abstract

This thesis is centered around reconstruction methods and their application to the study of the Dark Energy. It starts with an introduction to some important equations and concepts in its first chapter. In the second chapter the focus shifts to answering the question what is a reconstruction, its types and everything necessary to perform one. Chapter 3 is centered in a type of parameterization named Graduated Dark Energy, whose main defining feature consists on a DE density that can switch sign at a certain redshift. This DE model is then reconstructed and analyzed. Chapter 4 deals with some model-independent reconstructions for DE and provides some insights on some behaviours preferred by the datasets used, some of them being similar as the ones found within the gDE model of Dark Energy. The fifth chapter introduces the possibility of a weakly interacting Dark Sector (Dark Energy and Dark Matter), then some model-independent reconstructions are used to analyze this interaction to characterize it. Some interesting findings are made which also present some familiarity with previous chapters, even when the underlying approaches to reconstruction used are different. Finally in chapter 6 the conclusions are presented with some discussion regarding the findings of this work.



# Preface

The research contained in this thesis was carried out at the Instituto de Ciencias Físicas, UNAM. Chapter 1 contains an introduction to cosmology. Chapter 2 focuses on the theoretical background and is partly based on:

Luis E. Padilla, Luis O. Tellez, **Luis A. Escamilla** and J. A. Vazquez, “*Cosmological Parameter Inference with Bayesian Statistics*”, Universe 7 (2021) 7, 213.

The next chapters are based on the following papers:

- Chapter 3: Özgür Akarsu, John D. Barrow, **Luis A. Escamilla** and J. A. Vazquez, “*Graduated Dark Energy: Observational hints of a spontaneous sign switch in the cosmological constant*”, Phys.Rev.D 101 (2020) 6, 063528.
- Chapter 4: **Luis A. Escamilla** and J. A. Vazquez, “*Model Selection applied to reconstructions of the Dark Energy*”, Eur.Phys.J.C 83 (2023) 3, 251.
- Chapter 5: **Luis A. Escamilla**, Özgür Akarsu, Eleonora Di Valentino and J. A. Vazquez, “*Model-independent reconstruction of the Interacting Dark Energy Kernel: Binned and Gaussian process*”, JCAP 11 (2023) 051.

And finally Chapter 6 contains the conclusions and final remarks regarding the overall work in this thesis.

Other works:

- Tonatiuh Matos, **Luis A. Escamilla**, Maribel Hernández, J. A. Vázquez, “*Cosmology on a Gravitational Wave Background*”, arxiv:2309.09989.
- **Luis A. Escamilla**, William Giaré, Eleonora Di Valentino, Rafael C. Nunes, Sunny Vagnozzi, “*The state of the dark energy equation of state circa 2023*”, arxiv:2307.14802.



# List of Figures

1.1	Tension in the estimation of the parameter $H_0$ . It is observed that as the data becomes more precise the difference between estimations grows. Image from [51]	30
2.1	Bin graph with 8 nodes, 8 bins and two values of $\xi$ for the bins. It is easy to observe the difference in smoothness with a bigger $\xi$ for the bins. . . . .	42
3.1	$\Omega_{m,0} = 0.30$ is used and, for gDE-CDM, $\gamma = -0.03$ along with $\lambda = -10$ (green). $H(z)/(1+z)$ vs. $z$ for the gDE-CDM (green) and $\Lambda$ CDM (black). $H_0 = 70\text{km s}^{-1}\text{Mpc}^{-1}$ (solid) and $H_0 = 73\text{km s}^{-1}\text{Mpc}^{-1}$ (dashed). $H_0 = 69.8 \pm 0.8\text{ km s}^{-1}\text{Mpc}^{-1}$ from the TRGB $H_0$ [109], $H(z = 0.57) = 97.9 \pm 3.4\text{ km s}^{-1}\text{Mpc}^{-1}$ [27], and $H(z = 2.34) = 222.4 \pm 5.0\text{ km s}^{-1}\text{Mpc}^{-1}$ from the latest BAO data [90]. $H_0 = 73.52 \pm 1.62\text{ km s}^{-1}\text{Mpc}^{-1}$ is independent measurement from Gaia parallaxes [200]. . . . .	55
3.2	1D marginalised posterior distributions for the graduated $\gamma$ parameter (top left panel), $\Psi \equiv 3\gamma(1 - \lambda)$ (right) and the redshift location of the pole (if present) given by Eqn. (3.13). For a better display some particular cases of $\lambda$ values are included. . . . .	58
3.3	Top panel: 1D marginalised posterior distributions of $\Psi$ , along with (bottom panel) 2D posterior distributions of $\{\Psi, h_0\}$ colour coded by the $\gamma$ parameter. . .	60
3.4	Means values along with $1\sigma$ error bars from the 1D marginalised posterior distributions of $H_0[\text{km s}^{-1}\text{Mpc}^{-1}]$ . Green error bars are associated with the peak containing $\Psi \sim 0$ ( $\Lambda$ CDM), whereas red with the new peak stable at $\Psi \sim -0.86$ .	61



3.5 Graduated Dark energy model with varying the  $\lambda$  parameter. Left panel: 3D marginalised posterior distributions for the graduated  $\lambda$  and  $\Psi$  parameters, coloured coded by the  $\gamma$  parameter. Right panel: 1D marginalised posterior of the redshift position given by the pole. The vertical line is the mean value  $z_* = 2.32$ . . . . . 62

3.6  $Om h^2$  diagnostic for the graduated dark energy model with  $\lambda = -20$  using three redshifts  $\{z_1, z_2\}$  (left),  $\{z_1, z_3\}$  (middle) and  $\{z_2, z_3\}$  (right). The colour code indicates the value of  $\gamma$  parameter, where the yellow points mimic the  $\Lambda$ CDM behaviour and the pink ones the new feature introduced by the gDE model. . . . 63

3.7 Top panel:  $\rho_{\text{gDE}}/\rho_{\text{c0}}$  versus redshift  $z$  for  $\lambda = -20$  displays the maximum predicted that  $\rho_{\text{gDE}}$  changes sign at  $z \sim 2.3$ . Bottom:  $H(z)/(1+z)$  function. Include the latest BAO data points [34] (blue bars) where  $H_0 = 67.3 \pm 1.1$ , the Planck 2018 [6]  $H_0 = 67.4 \pm 0.5$  data (red bar) and the TGRB model independent [109]  $H_0 = 69.8 \pm 0.8$  data (green bar). Black dashed line corresponds to best-fit values of gDE and solid black line corresponds to  $\Lambda$ CDM. We note that, due to the jump at  $z \sim 2.3$ , the gDE model is not in tension with the BAO Ly- $\alpha$  data from  $z = 2.34$  in contrast to  $\Lambda$ CDM model and also gDE gives larger  $H_0$  values w.r.t.  $\Lambda$ CDM model and thereby relaxes  $H_0$  tension. . . . . 65

4.1 In this graph the differences in the  $\Delta\chi^2$  and the Bayes factor between  $\Lambda$ CDM and the reconstructions for  $w_{\text{DE}}(z)$  and  $\rho_{\text{DE}}/\rho_{\text{c},0}$  are shown. The green shades show the strength-of-evidence according to the Jeffrey's scale and the orange shades show the 1 to 4- $\sigma$  levels of statistical significance  $S/N \equiv \sqrt{|\Delta\chi^2|}$ . Ideally one wants the upper markers to stay as close as possible to the black line at 0 (preferably to cross it), which it is an indication of a better Bayes' factor, and the lower ones to be far away from zero, which indicates a better fit to the data. The stars indicate the fitness of the reconstruction of the CPL EoS (top) and the energy density with a sigmoid (bottom), the crosses indicate the internal  $z_i$  reconstructions and the triangles the reconstructions with 20 bins plus correlation function. The binning reconstructions are plotted with blue lines, whereas the nodal with red lines. . . . 78

4.2	These plots show the functional posterior probability: the probability of $w_{\text{DE}}(z)$ or $\rho_{\text{DE}}(z)/\rho_{\text{c},0}$ as normalised in each slice of constant $z$ , with colour scale in confidence interval values. The 68% ( $1\sigma$ ) and 95% ( $2\sigma$ ) confidence intervals are plotted as black lines. From left to right: parameterized equations of state for $w\text{CDM}$ and CPL, phenomenological sigmoid and 1-bin energy density reconstructions. The dashed black line corresponds to the standard $\Lambda\text{CDM}$ values. . . . .	79
4.3	From top to bottom: reconstructed $w_{\text{DE}}(z)$ with bins (and nodes), reconstructed $\rho_{\text{DE}}(z)/\rho_{\text{c},0}$ with bins (and nodes). It is easy to observe there is more structure (more apparent features) in the reconstructions as the number of parameters increases (from left to right). . . . .	80
4.4	From left to right: reconstructions with 20 bins, 20 bins with correlation function, internal $z_i$ -bins and internal $z_i$ -nodes. Purple figures correspond to the EoS whereas green to the energy density. . . . .	81
4.5	Derived functions for the reconstructed $w_{\text{DE}}(z)$ and $\rho_{\text{DE}}(z)/\rho_{\text{c},0}$ with 20 bins plus correlation function. The red dotted line in the derived $w_{\text{DE}}(z)$ corresponds to the best-fit values. . . . .	81
4.6	Applying the principal component technique to the reconstructions of the EoS and the energy density with 20 bins. By eliminating 5 PCs (which add up to about 5% of the total variance for each reconstruction) one obtains the orange figures with slightly overestimated errors localized in $z > 1.5$ . . . . .	85
4.7	Visual representation of the possibility of underfitting data with more parameters. . . . .	86
4.8	Functional posteriors of the EoS reconstruction, from up to down, with 4, 5 and 6 bins using only Hubble parameter data. . . . .	87
5.1	Comparison between a Gaussian Process for interpolation and a step function approach. The influence of the smoothness parameter $\xi$ in the Binning scheme is also shown. . . . .	94

5.2 Functional posterior probability of the reconstruction by using a Gaussian Process and  $w = -1$ . The probability as normalised in each slice of constant  $z$ , with colour scale in confidence interval values (see color bar at the right). The 68% ( $1\sigma$ ) and 95% ( $2\sigma$ ) confidence intervals are plotted as black lines. From left to right in the upper part: the rescaling function  $I_Q(z)$ , the Hubble Parameter, the deceleration parameter and the effective EoS parameter for DE. In the lower part: the effective EoS parameter for DM, the density for DM and DE respectively and the dimensionless interaction kernel  $\Pi_{DE}$ . The dashed black line corresponds to the standard  $\Lambda$ CDM values and the dotted line in the  $\Pi_{DE}(z)$  plot corresponds to the  $\Omega_m H(z)^2/H_0^2$  curve. . . . . 97

5.3 Functional posterior probability of the reconstruction by using a Gaussian Process and  $w = w_0$ . The probability as normalised in each slice of constant  $z$ , with colour scale in confidence interval values. The 68% ( $1\sigma$ ) and 95% ( $2\sigma$ ) confidence intervals are plotted as black lines. From left to right in the upper part: the rescaling function  $I_Q(z)$ , the Hubble Parameter, the deceleration parameter and the effective EoS parameter for DE. In the lower part: the effective EoS parameter for DM, the density for DM and DE respectively and the dimensionless interaction kernel  $\Pi_{DE}$ . The dashed black line corresponds to the standard  $\Lambda$ CDM values and the dotted line in the  $\Pi_{DE}(z)$  plot corresponds to the  $\Omega_m H(z)^2/H_0^2$  curve. . . . . 100

5.4 Functional posterior probability of the reconstruction by using a Binning scheme and  $w = -1$ . The probability as normalised in each slice of constant  $z$ , with colour scale in confidence interval values. The 68% ( $1\sigma$ ) and 95% ( $2\sigma$ ) confidence intervals are plotted as black lines. From left to right in the upper part: the rescaling function  $I_Q(z)$ , the Hubble Parameter, the deceleration parameter and the effective EoS parameter for DE. In the lower part: the effective EoS parameter for DM, the density for DM and DE respectively and the dimensionless interaction kernel  $\Pi_{DE}$ . The dashed black line corresponds to the standard  $\Lambda$ CDM values and the dotted line in the  $\Pi_{DE}(z)$  plot corresponds to the  $\Omega_m H(z)^2/H_0^2$  curve. . . . . 101

5.5	Functional posterior probability of the reconstruction by using a Binning scheme and $w = w_0$ . The probability as normalised in each slice of constant $z$ , with colour scale in confidence interval values. The 68% ( $1\sigma$ ) and 95% ( $2\sigma$ ) confidence intervals are plotted as black lines. From left to right in the upper part: the rescalation function $I_Q(z)$ , the Hubble Parameter, the deceleration parameter and the effective EoS parameter for DE. In the lower part: the effective EoS parameter for DM, the density for DM and DE respectively and the dimensionless interaction kernel $\Pi_{DE}$ . The dashed black line corresponds to the standard $\Lambda$ CDM values and the dotted line in the $\Pi_{DE}(z)$ plot corresponds to the $\Omega_m H(z)^2 / H_0^2$ curve.	102
5.6	Triangle plot of every model-independent reconstruction. The parameter $w_0$ is only present in two of the reconstructions and it is correlated with $\Pi_{DE,1}$ when using a GP to perform the interpolation.	103



# List of Tables

2.1	Jeffreys' scale. Using the convention from <a href="#">228</a> .	35
2.2	Cosmic Chronometer Hubble parameter measurements with their errors.	45
3.1	Mean values along with $1\sigma$ constraints on the set of parameters used to describe the gDE-CDM parameters. For one-tailed distributions the upper limit 95% C.L. is given. For two-tailed the 68% C.L. is shown. The last column, $-2\ln(\mathcal{L}_{\Lambda,\max}/\mathcal{L}_{\text{gDE},\max})$ , is used to compute best-fit differences of gDE-CDM from $\Lambda$ CDM ( $-2\ln\mathcal{L}_{\Lambda,\max} = 73.44$ ) based on the improvement in the fit alone.	57
3.2	Mean values along with $1-\sigma$ constraints on the set of parameters that describe <i>Om</i> diagnostic.	63
4.1	Additional parameters and their flat prior range.	73
4.2	Mean values, and standard deviations, for the cosmological parameters. For each model, the last two columns present the Bayes Factor, and the $\Delta\chi^2 = \chi_{\Lambda\text{CDM}}^2 - \chi_i^2$ for fitness comparison. The datasets used are BAO+H+SN. Here $\ln E_{\Lambda\text{CDM}} = -530.79(0.12)$ .	76
5.1	Mean values, and standard deviations, for the parameters used throughout the reconstructions. For each model, the last two columns present the Bayes Factor, and the $-2\Delta\ln\mathcal{L}_{\max} \equiv -2\ln(\mathcal{L}_{\max,\Lambda\text{CDM}}/\mathcal{L}_{\max,i})$ for fitness comparison. The datasets used are BAO+H+SN. Here $-2\ln\mathcal{L}_{\max,\Lambda\text{CDM}} = 1429.7$ , $\ln E_{\Lambda\text{CDM}} = -721.35(0.14)$ .	99
5.2	Constraints at 68% CL of the parameters for the model-independent reconstructions. The values for $\Pi_4$ are unconstrained for some of the cases, and for $\Pi_5$ every case, which is expected given the lack of data in this redshift.	99





# Contents

<b>List of Figures</b>	<b>9</b>
<b>List of Tables</b>	<b>15</b>
<b>1 Introduction</b>	<b>19</b>
1.1 Some important calculations	19
1.1.1 Cosmic Components	24
1.1.2 The Accelerated expansion and Dark Energy	26
1.2 The Standard Model of Cosmology	27
1.2.1 Problems with the standard model	28
<b>2 Theoretical Framework</b>	<b>31</b>
2.1 How to attack the issues?	31
2.2 Bayesian Statistics	32
2.3 Reconstructions	36
2.3.1 Parametric Reconstructions	36
2.3.2 Non-parametric reconstructions	37
2.3.3 Model-independent Reconstruction	39
2.4 Data	43
2.4.1 Hubble parameter	44
2.4.2 Type Ia supernovae	44
2.4.3 Baryon Acoustic Oscillations	46
2.4.4 Cosmic Microwave Background	47
<b>3 A model with Negative Energy Density: Graduated Dark Energy</b>	<b>49</b>
3.1 Introduction	49

3.2	Graduated dark energy	52
3.3	Constraints from the latest cosmological data	56
3.4	Spontaneous sign switch in the cosmological constant	64
<b>4</b>	<b>Model Independent Reconstructions of the Dark Energy</b>	<b>69</b>
4.1	Introduction	69
4.2	Reconstruction methodology	70
4.3	Theory and datasets	71
4.4	Results	75
4.5	Capturing features with the right amount of parameters	85
<b>5</b>	<b>Interacting Dark Energy in a Model Independent way</b>	<b>89</b>
5.1	Introduction	89
5.2	Interacting DM-DE Model	91
5.3	Binned and Gaussian Process interpolations	94
5.4	Datasets and Methodology	95
5.5	Results	96
<b>6</b>	<b>Conclusions</b>	<b>105</b>
6.1	Graduated DE	105
6.2	Model-independent EoS and DE density	106
6.3	Interacting DE with bins and GP	108
6.4	Concluding remarks	108
<b>7</b>	<b>Bibliography</b>	<b>111</b>

# Chapter 1

## Introduction

### 1.1 Some important calculations

When studying cosmology, we always begin with the same fundamental concept: the cosmological principle. According to this principle, the universe exhibits homogeneity and isotropy on large scales (approximately 100 Megaparsecs), implying that there is no preferred location in space. This principle forms the foundation for defining the geometry and dynamics of celestial objects within the universe. Building upon the notion of a homogeneous and isotropic universe, we can describe it as a sequence of three-dimensional surfaces arranged in a temporal order, each possessing a specific curvature. These surfaces maintain homogeneity and isotropy. The curvature can assume one of three values: zero curvature, positive curvature, or negative curvature.

- Zero curvature: also known as “flat space”, it corresponds to Euclidean space where the line element is given by:

$$dl^2 = dx^2 = \delta_{ij} dx^i dx^j, \quad (1.1)$$

and it is invariant under translations and rotations.

- Positive curvature: also called “spherical geometry”, it represents space as a 3-sphere where the line element is given by:

$$dl^2 = dx^2 + du^2, \quad x^2 + u^2 = a^2, \quad (1.2)$$

with  $a$  being the radius of the 3-sphere. This geometry is homogeneous and isotropic under 4-dimensional rotations.

- Negative curvature: also known as “hyperbolic geometry”, it is represented by a hyperboloid where the line element is given by:

$$dl^2 = dx^2 - du^2, \quad x^2 - u^2 = -a^2, \quad (1.3)$$

with  $a$  being an arbitrary constant. Homogeneity and isotropy arise from the symmetry of the line element under 4-dimensional pseudo-rotations (Lorentz transformations, where  $u$  corresponds to time).

If we rescale  $x \rightarrow xa$  and  $u \rightarrow ua$  in spherical and hyperbolic geometries, we can rewrite them as:

$$dl^2 = a^2(dx^2 \pm du^2), \quad x^2 \pm u^2 = \pm 1, \quad (1.4)$$

from which we can see that

$$udu = \mp \bar{x} \cdot d\bar{x}, \quad (1.5)$$

so

$$dl^2 = a^2 \left( dx^2 \pm \frac{(\bar{x} \cdot d\bar{x})^2}{1 \mp x^2} \right), \quad (1.6)$$

and by generalizing for flat space, we obtain

$$dl^2 = a^2 \left( dx^2 + k \frac{(\bar{x} \cdot d\bar{x})^2}{1 - kx^2} \right), \quad (1.7)$$

where  $k = -1, 0, 1$ . If  $k = -1$ , we have hyperbolic geometry, if  $k = 1$ , it is spherical geometry, and for  $k = 0$ , it is flat space. Because of this,  $k$  is referred to as “curvature”.

Rewriting it in spherical coordinates with  $dx^2 = dr^2 + r^2(d\theta^2 + \sin^2 \theta d\phi^2)$  and thus  $\bar{x} \cdot d\bar{x} = r dr$ , we have:

$$dl^2 = a^2 \left( \frac{(dr)^2}{1 - kr^2} + r^2 d\Omega^2 \right), \quad d\Omega^2 \equiv d\theta^2 + \sin^2 \theta d\phi^2, \quad (1.8)$$

and from this result, we obtain the Friedmann-Lemaitre-Robertson-Walker (FLRW) metric:

$$ds^2 = dt^2 - a^2(t) \left( \frac{(dr)^2}{1 - kr^2} + r^2 d\Omega^2 \right), \quad (1.9)$$

where  $a$  is now a function of time referred to as the “scale factor” and it quantifies the extent to which the universe expands or contracts. By convention, we set  $a(t_0) = 1$ , where  $t_0$  represents the current time. This metric reveals how the line element behaves in spacetime. Its importance lies in the fact that it provides an exact solution to Einstein’s equations of general relativity.

We can now define how particles move in this metric. Since they are considered to be in free fall, the trajectory they follow is determined by a geodesic. A geodesic is a curve that minimizes the proper time  $\Delta s/c$  between two points in spacetime (where  $\Delta s$  is the line element). The equation for these curves can be expressed as:

$$\frac{dU^\mu}{ds} + \Gamma_{\alpha\beta}^\mu U^\alpha U^\beta = 0, \quad (1.10)$$

Here,  $U^\mu \equiv \frac{dX^\mu}{ds}$  represents the four-velocity, and  $\Gamma_{\alpha\beta}^\mu$  denotes the Christoffel symbols:

$$\Gamma_{\alpha\beta}^\mu \equiv \frac{1}{2} g^{\mu\lambda} (\partial_\alpha g_{\beta\lambda} + \partial_\beta g_{\alpha\lambda} - \partial_\lambda g_{\alpha\beta}), \quad \partial_\alpha \equiv \frac{\partial}{\partial X^\alpha}, \quad (1.11)$$

In the above expression,  $g_{\alpha\beta}$  corresponds to the metric, which satisfies  $g^{\beta\lambda} g_{\lambda\alpha} = \delta_\beta^\alpha$ . By using the chain rule

$$\frac{dU^\mu}{ds} = \frac{dX^\alpha}{ds} \frac{\partial U^\mu}{\partial X^\alpha} = U^\alpha \frac{\partial U^\mu}{\partial X^\alpha}, \quad (1.12)$$

we arrive to

$$U^\alpha \left( \frac{\partial U^\mu}{\partial X^\alpha} + \Gamma_{\alpha\beta}^\mu U^\beta \right) = 0, \quad (1.13)$$

with the term in parenthesis being the covariant derivative of  $U^\mu$ , which let us rewrite it as

$$U^\alpha \nabla_\alpha U^\mu = 0, \quad (1.14)$$

using the definition of the 4-momentum  $P^\mu = mU^\mu$ , being  $m$  the mass, we can further rewrite it as

$$P^\alpha \left( \frac{\partial P^\mu}{\partial X^\alpha} + \Gamma_{\alpha\beta}^\mu P^\beta \right) = 0. \quad (1.15)$$

Defining  $\gamma_{ij} \equiv \delta_{ij} + k \frac{x_i x_j}{1 - k(x_k x^k)}$  we can write the metric as

$$ds^2 = dt^2 - a^2(t) \gamma_{ij} dx^i dx^j. \quad (1.16)$$

The Christoffel symbols that are different from zero will be:

$$\Gamma_{ij}^0 = a\dot{a}\gamma_{ij}, \quad \Gamma_{0j}^i = \frac{\dot{a}}{a}\delta_j^i, \quad \Gamma_{jk}^i = \frac{1}{2}\gamma^{il}(\partial_j\gamma_{kl} + \partial_k\gamma_{jl} - \partial_l\gamma_{jk}). \quad (1.17)$$

Now we can start working with Einstein equations:

$$G_{\mu\nu} = 8\pi GT_{\mu\nu}, \quad (1.18)$$

where  $G_{\mu\nu}$  represents the Einstein tensor, which describes the curvature of spacetime, and  $T_{\mu\nu}$  represents the energy-momentum tensor, which describes the matter content of the universe.

Since we are taking the Cosmological Principle as a starting point the energy-momentum tensor must satisfy the conditions of homogeneity and isotropy. It can be modeled using the tensor of a perfect fluid, therefore,

$$T_{\mu\nu} = (\rho + P)U_\mu U_\nu - P g_{\mu\nu}, \quad (1.19)$$

$$T_{00} = \rho(t), \quad T_{i0} = 0, \quad T_{ij} = -P(t)g_{ij}(t, x), \quad (1.20)$$

$$T_\nu^\mu = g^{\mu\lambda}T_{\lambda\nu} = \begin{pmatrix} \rho & 0 & 0 & 0 \\ 0 & -P & 0 & 0 \\ 0 & 0 & -P & 0 \\ 0 & 0 & 0 & -P \end{pmatrix}, \quad (1.21)$$

where  $\rho$  is the energy density,  $P$  is the pressure of the fluid (not to be confused with the four-momentum  $P^\mu$ ), and  $g_{\alpha\beta}$  is the metric. However, energy and momentum must be conserved, so the density must satisfy the continuity equation  $\dot{\rho} = -\partial_i\pi^i$  (where  $\pi^i \equiv T^{i0} = 0$ ), and the evolution of the momentum density must obey the Euler equation  $\dot{\pi}_i = \partial_i P$ . Using this two conservation equations we obtain

$$\partial_\mu T_\nu^\mu = 0, \quad (1.22)$$

and using the covariant derivative

$$\nabla_\mu T_\nu^\mu = \partial_\mu T_\nu^\mu + \Gamma_{\mu\lambda}^\mu T_\nu^\lambda - \Gamma_{\mu\nu}^\lambda T_\lambda^\mu = 0, \quad (1.23)$$

for the energy density we use  $\nu = 0$ , which gives us

$$\partial_\mu T_0^\mu + \Gamma_{\mu\lambda}^\mu T_0^\lambda - \Gamma_{\mu 0}^\lambda T_\lambda^\mu = 0, \quad (1.24)$$

since we suppose isotropy we have  $T_0^i = 0$ , then

$$\frac{d\rho}{dt} + \Gamma_{\mu 0}^\mu \rho - \Gamma_{\mu 0}^\lambda T_\lambda^\mu = 0, \quad (1.25)$$

which finally gives us the continuity equation

$$\dot{\rho} + 3\frac{\dot{a}}{a}(\rho + P) = 0. \quad (1.26)$$

Now we need to calculate the Einstein tensor  $G_{\mu\nu}$  from the Einstein equation. In general relativity, we have the following equation:

$$G_{\mu\nu} = R_{\mu\nu} - \frac{1}{2}Rg_{\mu\nu}, \quad (1.27)$$

where  $R_{\mu\nu} \equiv \partial_\lambda \Gamma_{\mu\nu}^\lambda - \partial_\nu \Gamma_{\mu\lambda}^\lambda + \Gamma_{\lambda\rho}^\lambda \Gamma_{\mu\nu}^\rho - \Gamma_{\mu\lambda}^\rho \Gamma_{\nu\rho}^\lambda$  represents the Ricci tensor, and  $R = g^{\mu\nu} R_{\mu\nu}$  denotes the Ricci scalar. Due to the isotropy of the FLRW metric,  $R_{i0} = R_{0i}$  must be zero. Thus, we obtain:

$$R_{00} = -3\frac{\ddot{a}}{a}, \quad R_{ij} = -\left(\frac{\ddot{a}}{a} + 2\left(\frac{\dot{a}}{a}\right)^2 + 2\frac{k}{a^2}\right)g_{ij}, \quad R = -6\left(\frac{\ddot{a}}{a} + \left(\frac{\dot{a}}{a}\right)^2 + \frac{k}{a^2}\right), \quad (1.28)$$

and the non-zero components of the Einstein tensor  $G_\nu^\mu \equiv g^{\mu\lambda} G_{\lambda\nu}$ .

$$G_0^0 = 3\left(\left(\frac{\dot{a}}{a}\right)^2 + \frac{k}{a^2}\right), \quad G_j^i = \left(2\frac{\ddot{a}}{a} + \left(\frac{\dot{a}}{a}\right)^2 + \frac{k}{a^2}\right)\delta_j^i, \quad (1.29)$$

using this result and [1.21](#) in the Einstein Equations [1.18](#) we obtain the **Friedmann Equations**

$$\left(\frac{\dot{a}}{a}\right)^2 = \frac{8\pi G}{3}\rho - \frac{k}{a^2}, \quad (1.30)$$

$$\frac{\ddot{a}}{a} = -\frac{4\pi G}{3}(\rho + 3P). \quad (1.31)$$

These equations govern the expansion of the universe (homogeneous and isotropic). Equation [1.30](#) is commonly expressed in terms of the Hubble parameter  $H \equiv \frac{\dot{a}}{a}$ , and  $\rho$  and  $P$  represent the total density and pressure contributions from all components of the universe (matter, radiation, etc.). The critical density at the present day (denoted by the subscript 0) is defined as  $\rho_{\text{crit}} = \frac{3H^2}{8\pi G}$ , from which the dimensionless density parameters are defined:



$$\Omega_i \equiv \frac{\rho_i}{\rho_{crit}}, \quad (1.32)$$

which for the curvature  $k$  takes the form  $\Omega_k \equiv \frac{-k}{(aH)^2}$ . We can then rewrite [1.30](#) as

$$H^2(a) = H_0^2 \left[ \Omega_{total} + \Omega_{k,0} \left( \frac{1}{a} \right)^2 \right], \quad (1.33)$$

where the subscript 0 means its value today (by convention we have  $a = 1$  at present time). Now we will delve a little deeper into which elements constitute  $\Omega_{total}$ .

### 1.1.1 Cosmic Components

We begin with **matter**. In cosmology, matter refers to any component with a pressure much smaller than its density, which allows us to approximate  $P \approx 0$  in equation [1.26](#). By doing so, we obtain:

$$\frac{\dot{\rho}}{\rho} = -3 \frac{\dot{a}}{a}. \quad (1.34)$$

From here, we find:

$$\rho \propto a^{-3}, \quad (1.35)$$

which is expected since the density of matter is inversely proportional to the volume of the universe. This density is primarily composed of two types of matter:

- Baryonic matter: Observable (luminous) matter such as nuclei and electrons.
- Dark matter: An unknown type of matter that does not interact with light. We will discuss it further later.

Let's now examine the next component in the cosmos: **radiation**. In cosmology, radiation refers to a component whose pressure is one-third of its density, i.e.,  $P = \frac{1}{3}\rho$ . Thus, equation [1.26](#) yields:

$$\frac{\dot{\rho}}{\rho} = -4 \frac{\dot{a}}{a}. \quad (1.36)$$

Consequently,  $\rho \propto a^{-4}$ . This behavior applies to a gas of relativistic particles (where the momentum of the particles is much greater than their mass). The density decreases with  $a^4$  due to the change in volume ( $a^3$ ) and a phenomenon known as "redshift". To fully comprehend

the meaning of the extra  $a$  (compared to matter) we need to explain the concept of redshift in Cosmology. Starting from the **Hubble's law**:

$$v(t) = Hr(t), \quad (1.37)$$

which states that distant objects (relative to us) recede from us at a velocity proportional to their distance, where  $v(t)$  represents the recession velocity of an object (the rate at which it moves away from us),  $H$  is the Hubble parameter, and  $r(t)$  is the object's position relative to us. Now, if we consider  $dv = Hdr$ , and since  $H = \frac{\dot{a}}{a}$ , we have:

$$dv = \frac{\dot{a}}{a} dr. \quad (1.38)$$

However, when considering the light reaching us from the object, we need to account for the Doppler effect due to the object's motion. For this effect, we have:

$$\frac{\lambda_r - \lambda_e}{\lambda_e} = \frac{d\lambda}{\lambda_e} = \frac{dv}{c}, \quad (1.39)$$

where  $c$  represents the speed of light in vacuum,  $\lambda_r$  is the wavelength received by the observer, and  $\lambda_e$  is the wavelength emitted by the object. Now, since we are dealing with light, we have  $c = \frac{dr}{dt}$ , and considering all of this, we obtain:

$$\frac{d\lambda}{\lambda_e} = \frac{\dot{a}}{a} dt = \frac{da}{a}, \quad (1.40)$$

this implies  $\lambda \propto a$ . Therefore, we define the **redshift**  $z$  as:

$$1 + z = \frac{\lambda_r}{\lambda_e} = \frac{a(t_r)}{a(t_e)}, \quad (1.41)$$

using the convention that at the present time  $t_0$ , we have  $a(t_0) = 1$ , we obtain:

$$z = \frac{1}{a} - 1. \quad (1.42)$$

As observed in [1.40](#), we have  $\lambda \propto a$ , and since the energy of a wave is inversely proportional to its wavelength, an increase in wavelength leads to a proportional decrease in energy with respect to  $a$ . This accounts for the 4 in the relation  $\rho \propto a^{-4}$ , 3 corresponds to a spatial expansion and 1 accounts for the redshift. Radiation is primarily composed of:

- Photons: Electromagnetic radiation (light).
- Neutrinos: Particles with extremely small masses but very high kinetic energy.

Lastly, we will delve into the component that forms the central focus of this work: the enigmatic entity known as Dark Energy.

### 1.1.2 The Accelerated expansion and Dark Energy

By Taylor-expanding the scale factor  $a(t)$  we obtain

$$a(t) = a(t_0) + \dot{a}(t_0)[t - t_0] + \frac{1}{2}\ddot{a}(t_0)[t - t_0]^2 + \dots, \quad (1.43)$$

where  $t_0$  is the present epoch. We divide by  $a(t_0)$  and we can define the deceleration parameter at epoch  $t_0$

$$q_0 = \frac{\ddot{a}(t_0)}{a(t_0)H_0^2}, \quad (1.44)$$

which can be generalized for a time  $t$  as

$$q(t) = \frac{\ddot{a}}{aH^2}. \quad (1.45)$$

The deceleration parameter provides valuable insights into the expansion of the universe, enabling us to discern whether it is undergoing an accelerated expansion ( $q < 0$ ) or a decelerated one ( $q > 0$ ) at a particular point in time. This parameter serves as a crucial diagnostic tool to understand the dynamics and evolution of the cosmos. If we now use the strong energy condition, which states that the sum of the energy density ( $\rho$ ) and three times the pressure ( $3p$ ) in all spatial directions must be non-negative ( $\rho + 3p \geq 0$ ) for the components of the universe, in the Friedmann equation [\[1.31\]](#) we obtain  $\ddot{a} < 0$ , which then implies  $q > 0$ .

At this point, we might be inclined to conclude that the universe is likely experiencing a gradually slower expansion over time. However, a groundbreaking discovery in 1998 shattered this prevailing notion. Observations of type Ia supernovae (SN1a) revealed the startling truth: the universe is expanding at an accelerated pace [\[201\]](#). This finding has been reproduced by several other cosmological probes [\[100, 99, 24, 2\]](#), consistently confirming that our universe underwent a transition from decelerated expansion to accelerated expansion at a redshift of approximately  $z \approx 0.5$ .

With this discovery fully cemented a formidable challenge arises: trying to find out the driving force of the accelerated expansion. To address this problem, scientists developed the idea of a new type of energy, later named Dark Energy (DE) for its elusive and unknown nature. But how do we add this new component to our current Cosmological model? Let's start by assuming that the DE is a perfect barotropic fluid which has a density  $\rho_{\text{DE}}$  and a pressure  $p_{\text{DE}}$  that are related via the equation of state

$$w = \frac{p_{\text{DE}}}{\rho_{\text{DE}}}. \quad (1.46)$$

Using the continuity equation [1.26](#) for DE we obtain

$$\Omega_{\text{DE}}(a) = \Omega_{\text{DE},0} e^{-3 \int_1^a \frac{da'}{a'} (1+w)}, \quad (1.47)$$

By employing the density parameters, we can reformulate the Friedmann equation. By taking into account how each component evolves with time, we arrive at the following expression:

$$H^2(a) = H_0^2 \left[ \Omega_{r,0} \left(\frac{a_0}{a}\right)^4 + \Omega_{m,0} \left(\frac{a_0}{a}\right)^3 + \Omega_{k,0} \left(\frac{a_0}{a}\right)^2 + \Omega_{\text{DE},0} e^{-3 \int_1^a \frac{da'}{a'} (1+w)} \right], \quad (1.48)$$

where  $\Omega_{m,0}$  is the contribution due to dust-like matter,  $\Omega_{r,0}$  is the contribution of radiation and  $\Omega_{k,0}$  is the contribution due to curvature.

Given the strong energy condition for the other components we know that DE should be exotic enough so that  $\rho + 3p < 0$  (which implies a negative density or pressure) to have an accelerated universe. We also know that the density parameters by definition should fulfill

$$\sum_i \Omega_i = 1. \quad (1.49)$$

Finally, the effective equation of state of the universe can be expressed as

$$w_{\text{eff}} = \frac{p_r + p_{\text{DE}}}{\rho_m + \rho_r + \rho_{\text{DE}}}, \quad (1.50)$$

and, together with Friedmann equation [1.31](#) we can see that the last condition for an accelerated universe is  $w_{\text{eff}} < -\frac{1}{3}$ .

So far we have painted an interesting picture: a cosmological model that pretends to explain how the universe evolves taking into account its main components along with an exotic new one. But still we do not know what this new energy is or if it even exists as a component of the universe.

## 1.2 The Standard Model of Cosmology

In 1917, Albert Einstein introduced the famous cosmological constant  $\Lambda$  into his field equations, which makes them take the form:

$$G_{\mu\nu} + \Lambda g_{\mu\nu} = 8\pi G T_{\mu\nu}. \quad (1.51)$$

He did this with the belief that the universe was static. However, in 1929, Edwin Hubble's discovery shattered this notion. Hubble found compelling evidence that the universe was, in fact, expanding, challenging the static universe hypothesis. Although the introduction of the cosmological constant  $\Lambda$  initially aimed to achieve a static universe, it can be considered as a

contribution to the energy content of the universe. With a specific value, it emerges as a viable candidate to explain the observed accelerated expansion. This new component would have a density  $\rho_\Lambda = \Lambda/8\pi G$ , and for  $\rho_\Lambda$  to be a constant we require  $p_\Lambda = -\rho_\Lambda$ , which means that  $w_\Lambda = -1$ . By using this equation of state in [1.47](#) we arrive at

$$\Omega_\Lambda(z) = \Omega_\Lambda = \text{const.} \quad (1.52)$$

which then gives us the Friedmann Equation

$$H^2(a) = H_0^2 \left[ \Omega_{r,0} \left( \frac{a_0}{a} \right)^4 + \Omega_{m,0} \left( \frac{a_0}{a} \right)^3 + \Omega_\Lambda + \Omega_{k,0} \left( \frac{a_0}{a} \right)^2 \right]. \quad (1.53)$$

The combination of the concept of a cosmological constant as a representation for the DE with a Cold Dark Matter (CDM) gives birth to the  $\Lambda$ CDM model, considered to be the standard model in cosmology. It earns this status by being the simplest and most parsimonious model, involving the least number of parameters while encompassing the essential concepts of DE and DM in their rudimentary forms. Furthermore, the model finds its roots in the fundamental principles of cosmology, namely The Cosmological Principle and Einstein's General Relativity, which serve as the bedrock for contemporary cosmological understanding.

### 1.2.1 Problems with the standard model

While the  $\Lambda$ CDM model has achieved significant success, it encounters a growing number of challenges as increasingly precise observational data becomes accessible. An immediate and fundamental challenge lies in the fact that we have very little knowledge about the true nature of Dark Energy and Dark Matter. This is particularly worrisome, considering that nearly all observational evidence suggests that these two components should constitute approximately 95% of the total energy content of the universe.

Some efforts were made to relate the DE to some sort of vacuum energy, but this does not agree with the theoretical predictions found by quantum field theory of vacuum [203](#), which is  $10^{123}$  times larger than the one observed in cosmology. Its origin is still a mystery. The standard model explains some observations very well, but as more cosmological data become available, several problems begin to arise [57, 105](#). One of the most studied is that of the tension arising from finding the value of the Hubble constant  $H_0$  (Figure [1.1](#)) using data from the CMB from the Planck telescope [75](#) or from the BOSS collaboration [8](#) and comparing it with the value obtained from SN1a or the distance ladder [105](#). It is quite a strong tension and as the observations become more precise it seems that it is only increasing [105, 261](#).

This poses a significant issue because all these observations were expected to be consistent within the framework of the  $\Lambda$ CDM model. However, it's possible that this isn't the case, and these issues may be pointing towards the need for a paradigm shift in our cosmological model. Along these problems we have other concerning the CDM part of  $\Lambda$ CDM, but many of these relate to smaller scales [144] such as the “missing satellites problem”, which says that the standard model predicts more small-scale structures (dwarf galaxies, etc.) in the universe than are observed. It is also important to mention that these problems may be due to statistical fluctuations [212] or systematic errors in the data still to be found, although it is interesting that these tensions have only increased in statistical significance over time instead of decreasing.

These issues serve as powerful motivation for physicists and cosmologists to explore alternative models and innovative solutions, and the main goal of this thesis is to explore a particular approach called “Reconstructions”, which will be explored in greater detail in the following chapter.

# flat – $\Lambda$ CDM

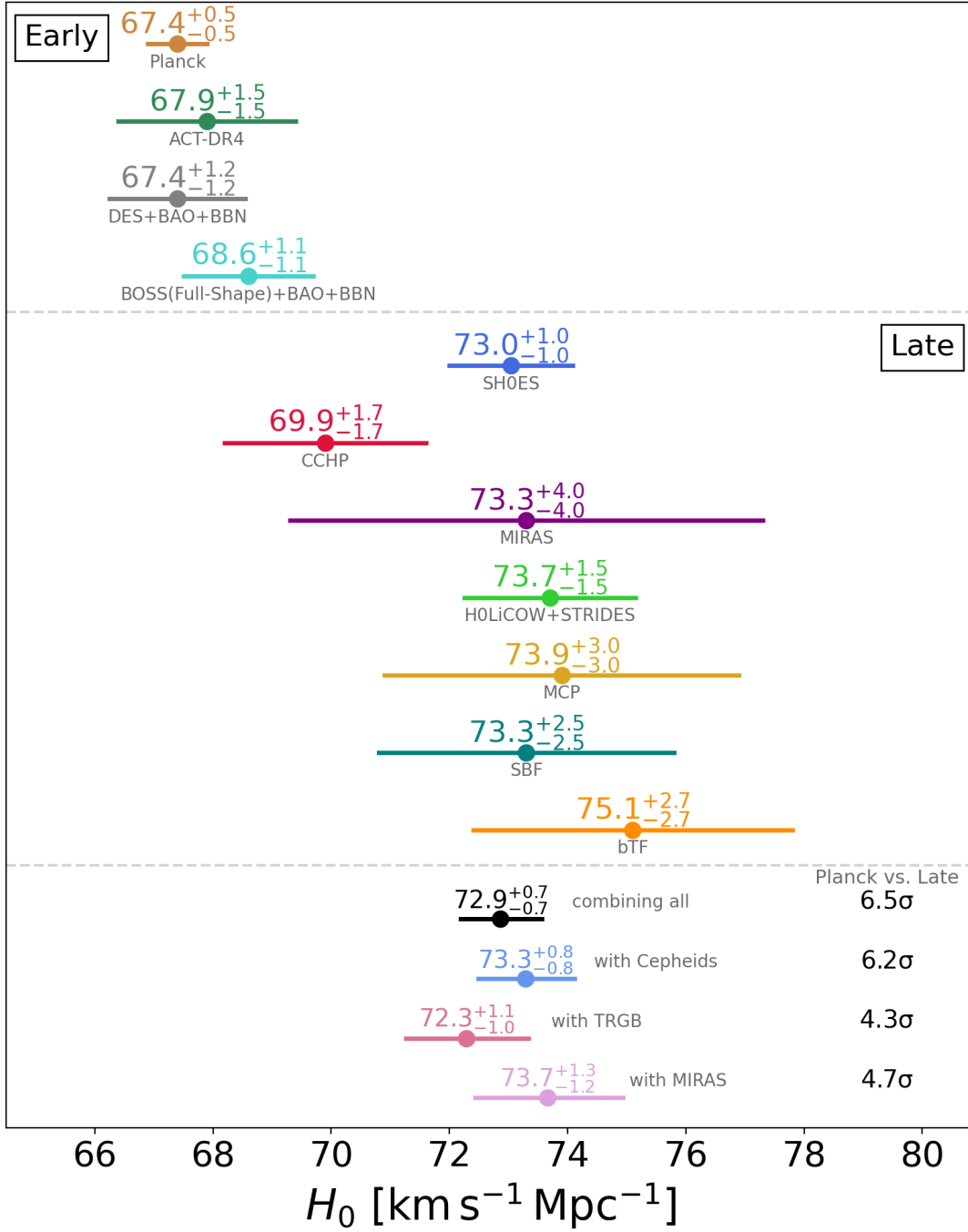


Figure 1.1: Tension in the estimation of the parameter  $H_0$ . It is observed that as the data becomes more precise the difference between estimations grows. Image from [51]



## Chapter 2

# Theoretical Framework

In this chapter, the focus will be on explaining essential concepts that underpin the research done in this work. The theoretical, numerical, and statistical tools that will be employed throughout this work will be defined and explored. Understanding these tools is crucial to ensuring the accuracy and reliability of the findings.

### 2.1 How to attack the issues?

If one intends to find an approach to the problems of the standard model mentioned in the previous chapter there are a variety of options, which can broadly be categorized into two: either considering that the underlying theory is flawed or questioning the accuracy of the data. If one assumes that the data is wrong there is limited recourse at the individual researcher-level apart from conducting statistical analyses of the data or patiently awaiting updated and more accurate data sets released by large collaborations. When considering the theory itself as the potential issue we have a lot of alternatives.

As explained in the previous chapter the  $\Lambda$ CDM model uses the constant  $\Lambda$  (Lambda) to denote the dark energy contribution to the total energy in the universe, but given that this approach presents some issues, there are some alternatives that propose some sort of dynamic DE (redshift dependency). Some options are the dark energies with Phantom [61], Quintessence [60] or Quintom scalar fields [122]. As a consequence of these scalar fields the equation of state (EoS) for DE is different than  $-1$  and can even cross this value (upwards or downwards depending on the field) in the case of the Quintom scalar field, opposite of the  $\Lambda$ CDM model in which the EoS is assumed to be a constant. A model known as “Early Dark Energy”, which

proposes a DE that behaves as a Cosmological Constant at early times, has been studied to solve this tension and reconciles the  $H_0$  values pretty well [192], further proving that our DE may in fact be of a dynamic nature. Alternatives known as modified gravity [171] are also proposed, these alternatives attempt to explain DE as a geometric phenomenon or correction to the Einstein's equations instead of an unknown component to the energy of the universe. Here we have from theories known as  $f(R)$  (since they propose a function that depends on the Ricci scalar  $R$ ) [172] to theories with extra dimensions such as brane world cosmology [133, 56].

The main approach to be used in this thesis will be that of a dynamical DE. By allowing the DE to be redshift-dependent one can expect to alleviate the tensions in the parameter values and attempt to solve the problems underlying the DE proposal, but if one is primarily interested in the behavior of DE and not in its nature there is a very interesting approach. Before we dive into this approach, it is essential to clarify a fundamental concept that forms the basis for it: Bayesian Statistics.

## 2.2 Bayesian Statistics

This section is mainly based on [182].

At its core, the primary distinction between Bayesian and Frequentist statistics lies in their definition of probability. In the Frequentist perspective, probability is interpreted in the context of repeated measurements, given by

$$P = \frac{n}{N}, \tag{2.1}$$

where  $n$  represents the number of favorable outcomes and  $N$  stands for the total number of trials. Frequentist statistics defines the probability  $P$  as the limit when the number of independent trials tends towards infinity. In the realm of Frequentist statistics, probabilities are inherently tied to the frequencies of events. In contrast, Bayesian statistics broadens the notion of probability to encompass the level of confidence we have in a statement. Bayesian statistics connects probabilities with our understanding of an event.

Now we need some important concepts and definitions to fully grasp how Bayesian Statistics works. Consider a random variable  $x$  associated with a specific event, and let  $P(x)$  represent its corresponding probability distribution. In both scenarios, the identical rules of probability govern the situation:

$$P(x) \geq 0, \tag{2.2}$$

$$\int_{-\infty}^{\infty} dx P(x) = 1. \quad (2.3)$$

When having mutually exclusive events:

$$P(x_1 \cup x_2) = P(x_1) + P(x_2), \quad (2.4)$$

but, in general

$$P(x_1 \cup x_2) = P(x_1) + P(x_2) - P(x_1 \cap x_2).$$

These rules can be summarized as follows: The first condition (2.2) ensures positive probabilities for events. The second rule (2.3) normalizes probabilities, indicating certainty in obtaining one outcome. In the third point (2.4), mutually exclusive events' probability is the sum of individual probabilities. Finally, if one event depends on another, their joint probability  $P(x_1 \cap x_2)$  is the product:

$$P(x_1 \cap x_2) = P(x_1)P(x_2|x_1). \quad (2.5)$$

where  $P(x_2|x_1)$  is the conditional probability of  $x_2$  happening if  $x_1$  has already happened.

If two events  $x_1$  and  $x_2$  are mutually exclusive, then

$$P(x_1 \cap x_2) = 0 = P(x_2 \cap x_1). \quad (2.6)$$

These rules of probability distributions must be fulfilled by both Frequentist and Bayesian statistics. Now, we can introduce Bayes' Theorem, a cornerstone of Bayesian Statistics. Following Equation (2.5), it's necessary that  $P(x_1 \cap x_2) = P(x_2 \cap x_1)$  holds without loss of generality. The following relation then applies:

$$P(x_2|x_1) = \frac{P(x_1|x_2)P(x_2)}{P(x_1)}. \quad (2.7)$$

This equation is known as **the Bayes' theorem** and, as shown, is a direct consequence of the axioms of probability. It can be defined also in the context of a model with parameters to explain data in the following way: for a given model (or hypothesis)  $H$ , where  $x_1 \rightarrow D$  represents data and  $x_2 \rightarrow \theta$  represents the parameter vector of that hypothesis, we can reformulate the above equation as

$$P(\theta|D, H) = \frac{P(D|\theta, H)P(\theta|H)}{P(D|H)}, \quad (2.8)$$

where  $P(\theta|D, H)$  is called the **posterior** probability of the model,  $L(D|\theta, H) \equiv P(D|\theta, H)$  is called the **likelihood**,  $\pi(\theta) \equiv P(\theta|H)$  is called the **prior** and expresses how much we know  $a$

*priori* about our model and  $\mathcal{Z} \equiv P(D|H)$  is the evidence of the model, usually referred to as the **Bayesian Evidence**.

When selecting a prior some options are possible; nonetheless, a frequently used approach is the uniform (also referred to as flat or agnostic) prior  $\pi(\theta) \propto \text{const.}$ , which tells us that every parameter value is equally probable. Regarding the likelihood, by disregarding the prior given that it is flat, we can relate the posterior to the likelihood:  $P(\theta|D, H) \propto L(D|\theta, H)$ . Consequently, by maximizing this expression, we can determine the most plausible parameter set for a given model in light of the available data. The likelihood can be expressed as a multi-variable likelihood given by

$$L(D|\theta) = L(D|\theta_0) \exp \left[ -\frac{1}{2}(\theta_i - \theta_{0i})H_{ij}(\theta_j - \theta_{0j}) \right], \quad (2.9)$$

where

$$H_{ij} = -\frac{\partial^2 \ln L}{\partial \theta_i \partial \theta_j}, \quad (2.10)$$

is named the **Hessian matrix**, which controls whether the estimates of  $\theta_i$  and  $\theta_j$  are correlated. When considering the Gaussian approximation as presented in Equation (2.9), it becomes evident that the likelihood reaches its maximum when the quantity

$$\chi^2 \equiv (\theta_i - \theta_{0i})H_{ij}(\theta_j - \theta_{0j}), \quad (2.11)$$

is minimized. This quantity, commonly referred to as the **chi-square**, is directly linked to the Gaussian likelihood through  $L = L_0 e^{-\chi^2/2}$ . Consequently, maximizing the Gaussian likelihood is essentially equivalent to minimizing the chi-square. It is important to highlight that under certain circumstances the likelihood may not follow a Gaussian distribution.

When considering the Bayesian Evidence, it becomes evident that it functions as a normalization factor. It represents the average of the likelihood:

$$P(D|H) = \int d^N \theta P(D|\theta, H)P(\theta|H), \quad (2.12)$$

where  $N$  signifies the dimensionality of the parameter space. In many cases, this quantity is overlooked due to practical reasons, such as when assessing the parameter space of a singular model. However, the Bayesian evidence assumes a pivotal role when comparing models, guiding the identification of the most suitable one to accurately represent the data. This procedure is commonly referred to as *model selection*. To simplify calculations, the ratio of two evidences can be defined:

$$K \equiv \frac{P(D|H_0)}{P(D|H_1)} = \frac{\int d^{N_0} \theta_0 P(D|\theta_0, H_0)P(\theta_0|H_0)}{\int d^{N_1} \theta_1 P(D|\theta_1, H_1)P(\theta_1|H_1)} = \frac{\mathcal{Z}_0}{\mathcal{Z}_1}, \quad (2.13)$$

$\ln B_{0,1}$	Odds	Probability	Strength of evidence
$< 1.0$	$<3:1$	$<0.75$	Inconclusive
1.0	$\sim 3:1$	0.750	Weak evidence
2.5	$\sim 12:1$	0.923	Moderate evidence
5.0	$\sim 150:1$	0.993	Strong evidence

Table 2.1: Jeffreys’ scale. Using the convention from [228].

where  $\theta_i$  is a parameter vector (with dimensionality  $N_i$ ) for the hypothesis  $H_i$  and  $i = 0, 1$ . Or alternatively, the difference in the log evidence,  $\ln \mathcal{Z}_0 - \ln \mathcal{Z}_1$ , is often referred to as the **Bayes factor**  $B_{0,1}$ :

$$B_{0,1} = \ln \frac{\mathcal{Z}_0}{\mathcal{Z}_1}, \quad (2.14)$$

which provides an idea on how well model 0 may fit the data when compared to model 1. A useful reference scale that allows us to draw qualitative conclusions effectively is the named **Jeffreys’ scale** (refer to Table 2.1).

In typical scenarios, calculating the posterior distribution analytically is often challenging. In such cases, numerical tools assume a significant role in parameter estimation. Multiple alternatives are available to facilitate this process.

One method commonly used is the Markov Chain Monte Carlo (MCMC) [228] which uses random walkers to sample the parameter space and the likelihood distribution. We also have the nested sampling algorithm [217] (specifically the dynamic nested sampling), an algorithm that, much like the MCMC method, is used to make Bayesian parameter inference but with the advantage that one can get an estimate of the Bayesian evidence of each model.

In this work a python code named SimpleMC will be used (and modified when necessary) to perform the parameter inference procedure. This code can make MCMC processes for the posterior sampling. It can also do dynamic nested sampling using dynesty [219], a public, open-source, Python package. The SimpleMC code used in this work is stored here [1] and all the data used in this work is already implemented in SimpleMC.

## 2.3 Reconstructions

As mentioned before, we have several approaches to shed some light on possible solutions to the Cosmological Constant as a DE and its problems, and there is one alternative which works as the main focus of this work. This alternative is to perform **reconstructions**. Reconstructions serve the purpose of gaining insights into the dynamics of cosmological parameters when the genuine underlying function is not directly observable but can be derived from accessible data. For instance, they help in understanding how parameters (like the equation of state for DE) evolve concerning cosmic time or redshift. They will be broadly classified in 3 classes: parametric, non-parametric and model-independent. Depending on the type of reconstruction used one can get completely different results. In this section, I will provide a general overview of these methods, setting the stage for more detailed discussions in subsequent sections where we focus on the specific ones employed in this study.

### 2.3.1 Parametric Reconstructions

In these, a phenomenological parametric (a function) form is proposed to represent the quantity to be studied [207]. In parametric reconstructions one can find functions like the first terms of a Taylor series to combinations of logarithmic and exponential functions [207, 40]. All these have their respective characteristic parameters and they try to study a certain characteristic, i.e. exponential growth/decrease, oscillations, quintom-like behavior, etc. One of the best-known ones is the Chevallier-Polarski-Linder (CPL) [67] parameterization of the DE equation of state  $w(z) = w_0 + w_1 \frac{z}{1+z}$ , where the free parameters that are to be constrained by data are  $w_0$  and  $w_1$ . It is also common to study several similar parameterizations in a single study such as in [251] where 5 distinct functions are studied:

- $w(a) = w_0 e^{(a-1)}$
- $w(a) = w_0 a(1 - \log a)$
- $w(a) = w_0 a e^{(1-a)}$
- $w(a) = w_0 a(1 - \sin(1 - a))$
- $w(a) = w_0 a(1 - \arcsin(1 - a))$

each one with only one free parameter  $w_0$ , and all 5 tend to behave like a Phantom DE and alleviates (to a certain degree) the tension in the  $H_0$  parameter. There are others like the Padé

approximation [244, 40], as it often gives a better approximation than the first terms of a Taylor series, which is found to be as good as  $\Lambda$ CDM to explain the data observed (according to the Akaike and Bayesian information criteria [228, 189]) but it has a dependency on the redshift.

These reconstructions are not limited to study only the EoS as it has been seen for example in [119] where the deceleration parameter was parameterized as

$$q(z) = \frac{1}{2} + \frac{q_1 z + q_2}{(1+z)^2},$$

with two free parameters  $q_1$  and  $q_2$ . Two other approaches to reconstructing can be found in: [154] as  $q(z) = q_0 + q_1[\frac{\ln(N+z)}{1+z} + k]$  with free parameters  $q_0$ ,  $q_1$ ,  $N$  and  $k$ ; and in [257] where the two parameterizations  $q(z) = a + \frac{bz}{1+z}$  and  $q(z) = \frac{1}{2} + \frac{az+b}{(1+z)^2}$  with parameters  $a$  and  $b$ . One could also parameterize the jerk parameter [130, 164] or even directly the DE density, i.e. the Generalised Emergent Dark Energy (GEDE) [148, 249, 130], the Early Dark Energy (EDE) [191] and the Energy-Momentum Log-gravity (EMLG) [9].

During the course of this work some new parameterizations will be introduced. They will be discussed in greater detail in subsequent chapters.

Parametric reconstructions are then usually compared (by using Bayesian statistics) with the  $\Lambda$ CDM model to look for deviations from it and are useful to know the expected/preferred behavior of the DE, even if its underlying nature is still a mystery. Still they have the disadvantage of assuming a functional form a priori. Adopting this approach can lead to some bias regarding the function used. The problem of too many possible functions and variations to choose from is also present. To avoid these problems one can instead perform the other type of approach to a reconstruction: the non-parametric one.

### 2.3.2 Non-parametric reconstructions

Non-parametric reconstructions are more focused on the data and aim to be as free from model assumptions as possible. It doesn't rely on a specific functional form and seeks to describe the data without making strong assumptions a priori. They can be seen as the "counterpart" of the parametric ones.

Non-parametric reconstructions may include the use of Artificial Neural Networks or Gaussian processes (more on this one later), as they have proven to be useful in cosmology as more data become available [139, 213, 131, 233, 22, 254, 111, 247, 132, 239, 241, 118]. We also have as a non-parametric approach the Loess+Simex method [157], which combines the regression LOESS with the simulation-extrapolation technique SIMEX. This hybrid process leverages the strengths of both LOESS and SIMEX to achieve a more robust and accurate reconstruction of

cosmological quantities from observational data. Another non-parametric approach consists of combining Principal Component analysis (also more on this one later) with the Goodness of Fit (GoF) [256]. With this approach a deviation from the  $\Lambda$ CDM EoS ( $w = -1$ ) was found around  $z > 1.5$ . In this work two non-parametric approaches will be used: a Gaussian Process (GP) and Principal Component Analysis (PCA).

### Gaussian Process

GPs have been recently become very popular non-parametric reconstructions. For example in [213] a non-parametric reconstruction was made over  $H(z)$ ,  $w(z)$  and  $q(z)$  using the Union 2.1 SN1a data [225] and it agrees with the  $\Lambda$ CDM model, but the data used only encompasses a redshift up to 1, so the errors beyond this point are not constrained. Nevertheless the Gaussian Process approach has proven useful in cosmology as more data becomes available [233, 22, 254, 111, 247, 132, 239]. But what is a Gaussian Process?

A Gaussian Process (GP) is the generalization of a Gaussian distribution, that is, in every position  $x$ ,  $f(x)$  is a random variable. It is characterized by a mean function  $\mu(x)$  and a covariance  $\sigma^2 K(x, x')$ , where  $\sigma^2$  is the variance and  $K(x, x')$  the kernel representing the correlation of  $f$  between two different positions  $f(x)$  and  $f(x')$ . For an arbitrary amount of positions  $x_1, \dots, x_n$  then we have a multivariate Gaussian distribution

$$\bar{f} = [f(x_1), \dots, f(x_n)] \sim \bar{N}(\bar{\mu}, \sigma^2 K(\bar{x}, \bar{x}')), \quad (2.15)$$

where  $\bar{\mu} = [\mu(x_1), \dots, \mu(x_n)]$ , and

$$K(\bar{x}, \bar{x}') = \begin{pmatrix} K(x_1, x_1) & K(x_1, x_2) & \cdots & K(x_1, x_n) \\ K(x_2, x_1) & K(x_2, x_2) & \cdots & K(x_2, x_n) \\ \vdots & \vdots & \ddots & \vdots \\ K(x_n, x_1) & K(x_n, x_2) & \cdots & K(x_n, x_n) \end{pmatrix}. \quad (2.16)$$

The Kernel to be used in this work is the Radial Basis Function (RBF)

$$K(x, x') = \exp[-\theta(x - x')^2], \quad (2.17)$$

where the parameter  $\theta$  tells us how strong is the correlation. This kernel has the advantage of minimizing the degeneracies created due to a high number of hyperparameters since it only has  $\theta$ , it is isotropic if one chooses  $x = z$  being  $z$  the cosmological redshift, and it is also infinitely differentiable.

In this work a Gaussian Process will be used to perform some reconstructions, but it will be in an unorthodox manner. More on this in chapter 5.



## PCA

After doing a reconstruction we can perform a process known as Principal Component Analysis (PCA) on the parameters. Let's say we reconstruct the EoS using some parameters  $w_i$ . We start by computing the Fisher matrix of the parameters  $w_i$ , which is approximately  $F = C^{-1}$ , where  $C$  is the covariance matrix of the parameters  $w_i$ . Then we diagonalize  $F$  to find a basis where the parameters are uncorrelated, so that

$$F = W^T D W \quad (2.18)$$

where the rows of  $W$  are the eigenvectors  $e_i(z)$  of the basis in which the parameters are uncorrelated and  $D$  is a diagonal matrix. If  $\vec{p}$  is the vector of the best-fit values of the  $w_i$  then the new uncorrelated parameters are  $\vec{q} = W\vec{p}$ . Being  $d_i$  the diagonal elements of  $D$  we accommodate them such that  $d_1 > d_2 > \dots > d_N$ , and also their correspondent  $e_i(z)$  and  $q_i$ . These  $d_i$  are related with the errors as  $\frac{1}{\sqrt{d_i}} = \sigma_i$ . Then we can reconstruct the EoS as

$$w(z) = \sum_{i=1}^N q_i e_i(z), \quad (2.19)$$

with error

$$\sigma(w(z_n)) = \left( \sum_{i=1}^N \sigma^2(q_i) e_i^2(z_n) \right)^{1/2}, \quad (2.20)$$

where  $z_n$  is the redshift in which each parameter  $w_i$  is located. Now we can choose any number of principal components (PCs) to reconstruct the function (from 1 PC to the original number of parameters used in the reconstruction). If we use the same number of PCs as there are parameters then the reconstruction will look the same, but by removing the PCs with the smaller  $d_i$  we remove the noisiest aspects of the reconstruction (with biggest error  $\sigma_i$ , a common practice is to remove enough PCs to maintain 95% of the information or variance). By doing this we can draw conclusions about the data used and how well it constrains the parameters. This method will be used in chapter [4](#)

### 2.3.3 Model-independent Reconstruction

Let us delve in the third class of reconstruction: the model-independent one. These reconstructions work as a blend of the parametric and non-parametric ones. They are parametric in the sense that the reconstruction has parameters to infer with data and, as such, can be used in

a model-comparison procedure against  $\Lambda$ CDM. And they are similar to non-parametric reconstructions since they rely on using functions that don't have a predefined or rigid shape, they have much more freedom of "structure" than a parametric one.

One type of model-independent approach is proposed in [79] which is named "correlation function method". In [261] it was found using this method that with current data (combining BAO, SN1a, Hubble parameter and Planck telescope data) a dynamical form for  $w(z)$  is preferred over a constant value with a  $3.5\sigma$  significance level. This method will be explained further in this work. We also have the nodal reconstruction [230, 231, 128, 31] in which a piecewise linear (or cubic) is used to represent the function to reconstruct. This approach has been used to reconstruct the EoS [231], here was found that, although the  $\Lambda$ CDM model is consistent with the data used then, the reconstruction presented some redshift dependency (like a small "hump" in  $z \approx 1.3$ ) but beyond  $z \approx 1.5$  the data used was too inaccurate to have a saying in how the EoS should behave. This method was used in [31] (although here they called it "knot-spline" reconstruction) with the Planck temperature data and showed that this non-parametric approach can be used to find specific features by allowing some central "knots" to vary in height and width.

In chapter 4 the main focus is on model-independent reconstructions, particularly the nodal reconstruction, the bin reconstruction and the correlation function method [79]. Let's delve a little more into these approaches to reconstruction.

### Nodal reconstruction

This reconstruction consists in using an interpolation, either linear or cubic spline, to fill in the gaps between a certain number of "nodes". As an example, if we have a node for the EoS in a coordinate  $(z_i, w_i)$  and wish to linearly interpolate it with a node in  $(z_{i+1}, w_{i+1})$  we need a straight line  $L_i$  as

$$L_i(z) = \frac{w_{i+1} - w_i}{z_{i+1} - z_i} (z - z_i) + w_i, \quad z \in [z_i, z_{i+1}]. \quad (2.21)$$

These nodes then are points in space kept at a certain distance from each other and with variable height  $w_i$  and, in some cases, variable width  $z_i$ .

The interpolation could also be made with higher order polynomials, this approach being called cubic spline, to preserve smoothness between nodes, but this approach presents heavy correlations between nodes and unwanted noise to the reconstruction, it can also present numerical problems when changing too abruptly the value of the node's position or if they are too close.

Also, since there will not be any derivatives it presents no problem to have no smoothness in the reconstruction. Given this the main focus in this work will be the linear ones.

### Bin reconstruction

Another approach utilized in this study is the step function or binning scheme. In this method, numerous steps or “bins” are employed and connected using hyperbolic tangents. As a function it looks like this:

$$w(z) = w_1 + \sum_{i=1}^{N-1} \frac{w_{i+1} - w_i}{2} \left( 1 + \tanh \left( \frac{z - z_i}{\xi} \right) \right), \quad (2.22)$$

where  $N$  is the number of bins,  $w_i$  is the bin value,  $z_i$  is the position where the bin begins in the  $z$  axis and  $\xi$  is a smoothness parameter. As illustrated in Figure [2.1](#), we can observe the step function with  $N = 8$  and two different values of  $\xi$ . Similar to the nodal reconstruction, these bins can adjust their heights to enhance data fitting. Although this function is presented with the Equation of State (EoS)  $w(z)$ , it represents the generalized form of the bin function. If one intends to use this approach for reconstructing any other function, the only modification required is adjusting the values that the bins/parameters  $w_i$  can assume.

The objective of these two methods is to visualize the shape of the reconstructed quantity, allowing us to discern the data’s preferred behavior. As this reconstruction approach is model-independent, it minimizes bias towards a specific functional form or model. However, it’s essential to acknowledge the potential for overfitting when using an excessive number of nodes or bins. To address this, model comparison will be employed, leveraging Bayesian Evidence to penalize such choices. Another way of diminishing this risk of overfitting is to introduce a Correlation Function.

### Correlation Function method

This method can be applied on top of the nodal and binning approaches in order to obtain a function that evolves smoothly [\[78\]](#). The idea behind it is to treat the quantity to be reconstructed in place as a random field evolving along with a correlation function  $\xi$ , for instance

$$\xi(\delta z) = \frac{\xi(0)}{1 + \left( \frac{\delta z}{z_c} \right)^2}, \quad (2.23)$$

with  $\xi(0)$  being the normalization factor and  $z_c$  represents a smoothing distance. The correlation function [\(2.23\)](#), named CPZ [\[79\]](#), has a characteristic correlation length after which its contribution decreases, hence providing stronger correlations between neighboring bins when they are

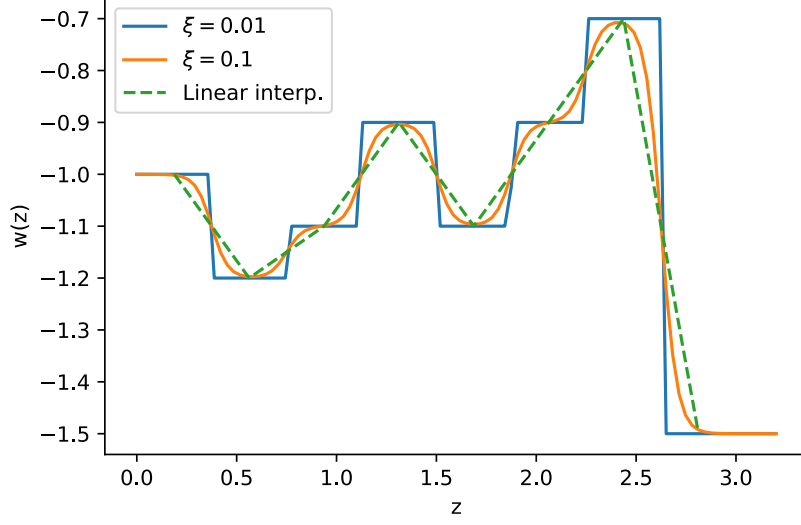


Figure 2.1: Bin graph with 8 nodes, 8 bins and two values of  $\xi$  for the bins. It is easy to observe the difference in smoothness with a bigger  $\xi$  for the bins.

located at distances smaller than  $z_c$ . There exist several alternatives that can reproduce this behaviour up to a certain degree, like the exponential fall-off  $\xi(\delta z) = \xi(0)e^{-\delta z/z_c}$  or the power law  $\xi(\delta z) = (\delta z/z_c)^{-n}$ , but the CPZ has a more transparent dependency in the parameters  $f_i$ , a relatively simpler behaviour and it constrains the high frequency modes better [79]. Throughout this work, I use the following values  $z_c = 0.3$  and  $\xi(0) = 0.1$  since they normalize the shorter wavelength modes of the data [78].

Assuming every amplitude  $f_i$  are equally distributed with the same width-location  $\Delta = z_{i+1} - z_i$ , then the average of  $f(z)$  over each  $f_i$  is

$$f_i = \int_{z_i}^{z_i+\Delta} f(z) dz. \quad (2.24)$$

The variation from the fiducial model averaged over the bin is  $\delta f_i = f_i - f_{\text{fid}}$ , where the fiducial model is the underlying scheme upon which the reconstruction will be dependent on. In this way the covariance matrix can be obtained by

$$C_{ij} \equiv \langle \delta f_i \delta f_j \rangle = \int_{z_i}^{z_i+\Delta} dz \int_{z_j}^{z_j+\Delta} dz' \xi(|z - z'|), \quad (2.25)$$

and therefore the associated prior

$$P_{\text{prior}} \propto e^{-\frac{1}{2}(f - f_{\text{fid}})^T C^{-1} (f - f_{\text{fid}})}. \quad (2.26)$$

Finally, once the prior is given (or equivalently  $\chi_{\text{prior}}^2 = -2 \ln P_{\text{prior}}$ ), the total  $\chi^2$  to minimize becomes

$$\chi^2 = \chi_{\text{data}}^2 + \chi_{\text{prior}}^2. \quad (2.27)$$

The fiducial model could be one previously known, for instance in the case of the dark energy EoS, it could be the cosmological constant with  $w_{\text{DE}}(z) = -1$  or  $\rho_{\text{DE}}(z) = \text{constant}$ . However, demanding a behaviour like the cosmological constant may create a bias when performing the reconstruction. The same would be true for any other fixed fiducial model, so I opted for the floating prior proposed by [79], where

$$f_i^{\text{fid}} = \sum_{|z_j - z_i| \leq z_c} \frac{f_j^{\text{recons}}}{N_j}, \quad (2.28)$$

here  $z_j$  is the position of the amplitude  $f_j$  and  $N_j$  is the number of amplitudes that fulfill the condition  $|z_j - z_i| \leq z_c$ . This floating prior makes sure that the parameter values stay continuous by evaluating the mean value of each parameter with its immediate neighbors.

It is important to mention that the correlation function method applied here is used as an “agnostic” way of reducing overfitting, agnostic in the sense that the imposed correlations are mainly obtained via a data-driven approach, not a theory-driven one, e.g. effective field theories (EFTs) such as Quintessence or Horndeski [73, 196, 103, 188, 197]. This could provide a small bias against EFTs, particularly Quintessence, as explained in [73]. Also, since this method is being used as a way to diminish overfitting it could even prevent some interesting features to appear or even wither existing ones, such as the disappearance of oscillatory features in the EoS, as seen in [188, 197], when using a theory prior.

## 2.4 Data

To make a reconstruction (or in general a Bayesian parameter inference procedure) one needs a set of data that will be used to constrain the free parameters of the model. In this work the data used is from the Hubble parameter [114], the Joint Light-curve Analysis (JLA) SN1a sample [34], the Pantheon and Pantheon+ SN1a samples [211], the BOSS and Lyman- $\alpha$  Baryonic Acoustic Oscillation (BAO) data [33] and the Planck CMB (treated as a BAO) [33].

### 2.4.1 Hubble parameter

The Hubble parameter tells us the expansion rate of the universe. It can be expressed as a function of the redshift  $z$  with the Friedmann equations. This parameter can be measured with old stars known as “cosmic chronometers” and they work as “standard clocks” in cosmology. It can be obtained by calculating the derivative of the cosmic time with respect to the redshift at  $z \neq 0$  as

$$H(z) \approx \frac{-1}{1+z} \frac{\Delta z}{\Delta t} \quad (2.29)$$

where the rate  $\Delta z/\Delta t$  is measured with the difference in age of the cosmic chronometers. In this work the data used is of these cosmic chronometers [135, 215, 223, 160, 260, 158, 159, 195] (written as H in the datasets) to constrain the parameters. In Table 2.2 they are reported and can be found within the repository [151].

The  $\chi^2$  of the cosmic chronometers is calculated as

$$\chi_H^2 = \sum_{i=1}^N \frac{(H_{i,m} - H_{i,obs})^2}{\sigma_i^2} \quad (2.30)$$

with  $H_{i,m}$  and  $H_{i,obs}$  being the Hubble parameter in the model and in the data and  $\sigma_i^2$  the error of the  $i$ th sample of H.

### 2.4.2 Type 1a supernovae

There are “standard candles” in cosmology as there are standard clocks. The type 1a supernovae (SN1a) take this place. The standard candles provide a luminosity distance in function of redshift as  $d_L(z) = (1+z)r(z)$ , with  $r(z)$  being the comoving distance

$$r(z) = \frac{1}{H_0} \int_0^z \frac{H_0}{H(z)} dz. \quad (2.31)$$

To achieve this, the distance modulus of a supernova is estimated as

$$\mu(z) = 5 \log \frac{D_L(z)}{Mpc} + 25. \quad (2.32)$$

where  $D_L(z) = H_0 d_L(z)$  is the luminosity distance. The distance modulus of the SN1a is derived from the empirical relation when observing light curves

$$\mu_{SN} = m_B^* + \alpha X - \beta C - M_B, \quad (2.33)$$

Table 2.2: Cosmic Chronometer Hubble parameter measurements with their errors.

$z$	$H \pm \sigma_H$ (CCB)	$H \pm \sigma_H$ (CCM)	$H \pm \sigma_H$ (CCH)	Ref.
0.07	$69 \pm 19.6$	...	...	[260]
0.09	...	...	$69 \pm 12$	[223]
0.12	$68.6 \pm 26.2$	...	...	[260]
0.17	...	...	$83 \pm 8$	[223]
0.1797	$75 \pm 4$	...	...	[160]
0.1993	$75 \pm$	...	...	[160]
0.2	$72.9 \pm 29.6$	...	...	[260]
0.27	...	...	$77 \pm 14$	[223]
0.28	$88.8 \pm 36.6$	...	...	[260]
0.3519	$83 \pm 14$	$88 \pm 16$	...	[160]
0.3802	$83 \pm 13.5$	$89.2 \pm 14.1$	...	[159]
0.4	...	...	$95 \pm 17$	[223]
0.4004	$77 \pm 10.2$	$82.8 \pm 10.6$	...	[159]
0.4247	$87.1 \pm 11.2$	$93.7 \pm 11.7$	...	[159]
0.4497	$92.8 \pm 12.9$	$99.7 \pm 13.4$	...	[159]
0.47	$89 \pm 49.6$	...	...	[195]
0.4783	$80.9 \pm 9$	$86.6 \pm 8.7$	...	[159]
0.48	...	...	$97 \pm 62$	[223]
0.5929	$104 \pm 13$	$110 \pm 15$	...	[160]
0.6797	$92 \pm 8$	$98 \pm 10$	...	[160]
0.7812	$105 \pm 12$	$88 \pm 11$	...	[160]
0.8754	$125 \pm 17$	$124 \pm 17$	...	[160]
0.88	...	...	$90 \pm 40$	[223]
0.9	...	...	$117 \pm 23$	[223]
1.037	$154 \pm 20$	$113 \pm 15$	...	[160]
1.3	...	...	$168 \pm 17$	[223]
1.363	$160 \pm 33.6$	$160 \pm 33.6$	...	[158]
1.43	...	...	$177 \pm 18$	[223]
1.53	...	...	$140 \pm 14$	[223]
1.75	...	...	$202 \pm 40$	[223]
1.965	$186.5 \pm 50.4$	$186.5 \pm 50.4$	...	[158]

where  $X$  is the stretch parameter,  $C$  is the color parameter,  $M_B$  is the absolute magnitude,  $m_B^*$  is the B-band apparent magnitude,  $\alpha$  and  $\beta$  are nuisance parameters. In the Pantheon Sample [211] the apparent magnitude  $m_B = m_B^* + \alpha X - \beta C$  is reported, and we fix the absolute magnitude  $M_B = -19.35$ , which is the best fitting value for  $\Lambda$ CDM. So we are left with the distance modulus

$$\mu(z) = 5 \log \frac{D_L(z)}{Mpc} + 25 = m_B - M_B, \quad (2.34)$$

from which the luminosity distance can be calculated. In this work both the old version of 1048 samples from the Pantheon SN1a sample [211] and the PantheonPlus data release [210] which consists of 1701 light curves of 1550 SNeIa are used. When used it will be written as SN in the datasets and it spans a redshift of  $0 < z < 2.26$ .

The  $\chi^2$  of the SN sample is calculated as

$$\chi_{\text{SN}}^2 = (\mu_{i,m} - \mu_{i,\text{obs}})C_{ij,\text{SN}}^{-1}(\mu_{j,m} - \mu_{j,\text{obs}}), \quad (2.35)$$

with  $\mu_{i,m}$  and  $\mu_{i,\text{obs}}$  being the distance modulus in the model and in the data and  $C_{ij,\text{SN}}$  the inverse covariance matrix of the observations. The full covariance matrix associated is comprised of a statistical and a systematic part, and along with the data, they are provided in the repository [136].

### 2.4.3 Baryon Acoustic Oscillations

The baryon acoustic oscillations (BAOs) are used as “standard rulers” in cosmology. They are used to measure the angular distance  $d_A = r(z)/(1+z)$ . The BAO scale is set by the radius of the sound horizon

$$r_d = \int_{z_d}^{\infty} \frac{c_s}{H(z)} dz, \quad (2.36)$$

$c_s$  being the sound speed of the baryon-photon fluid and  $z_d$  the drag epoch (when baryons and photons decouple) [95]. Since the size of  $r_d$  depends on the cosmological model, the BAO actually constrains  $D_A(z)/r_d$  (with  $D_A(z) = H_0 d_A(z)$ ),  $H(z)/r_d$  and the volume average distance  $D_V(z)/r_d = [(1+z)^2 D_A^2(z) cz/H(z)]^{1/3}$ . The BAO data used here is the Lyman  $\alpha$  DR-14 high-redshift measurements, MGS, 6dFGS and BAO-Galaxy consensus [20, 88, 32, 45, 44, 26]. To calculate the  $\chi^2$

$$\chi_{\text{BAO}}^2 = (b_{i,m} - b_{i,\text{obs}})C_{ij,\text{BAO}}^{-1}(b_{j,m} - b_{j,\text{obs}}) \quad (2.37)$$

where  $b_{i,m}$  and  $b_{i,\text{obs}}$  are the model and the BAO data values and  $C_{\text{BAO}}$  is the covariance matrix of the data.



#### 2.4.4 Cosmic Microwave Background

The data from Planck satellite for the Cosmological Microwave Background (CMB) is also used, but the focus is only on the cosmological background, not on perturbations, so the Planck data will be used as a BAO measurement in  $z \approx 1100$  [33], the last scattering redshift. This means that we measure the angular scale of the sound horizon at a large redshift. As explained in [33], the information of the CMB at a background level can be summarized in the 3 parameters  $w_b$  (physical baryon density parameter),  $w_{cb}$  (physical matter density parameter) and  $D_A(1100)/r_d$ , with their respective covariance matrix. To obtain the  $\chi^2$  we just, analogous to the BAO case, calculate

$$\chi_{PLK}^2 = (p_{i,m} - p_{i,obs}) C_{ij,PLK}^{-1} (p_{j,m} - p_{j,obs}) \quad (2.38)$$

where  $\mathbf{p}$  is the parameter vector and  $C_{PLK}$  is the covariance matrix.



## Chapter 3

# A model with Negative Energy

# Density: Graduated Dark Energy

### 3.1 Introduction

As explained in first chapter, one of the most intriguing tensions reported so far is the significant deficiency in the Hubble constant  $H_0$  value predicted by the cosmic microwave background (CMB) Planck data [4, 6] using the base  $\Lambda$ CDM model when compared with the values by direct model-independent local measurements [199, 200, 198, 109]. Surprisingly, the situation changes if the DE energy density is not restricted to be strictly positive. It has been reported that a number of persistent low-redshift tensions, including the  $H_0$  tension, may be alleviated by a dynamical DE whose energy density can assume negative values or vanish at a finite redshift [90, 34, 205, 161, 190, 64, 242, 97, 36, 35, 234, 255].

The possible need for a DE whose energy density can assume negative values was previously emphasised by the observation that, when the base  $\Lambda$ CDM model is considered, the Ly- $\alpha$  forest measurement of the BAO by the BOSS collaboration prefers a smaller value of the dust density parameter than is preferred by the CMB data [90]. They reported a clear detection of DE consistent with  $\Lambda > 0$  for  $z < 1$ , but with a preference for a DE assuming negative energy density values for  $z > 1.6$  and argued that the Ly- $\alpha$  data from  $z \approx 2.34$  can fit a non-monotonic evolution of  $H(z)$ , i.e., of the total energy density  $\rho_{\text{tot}}(z)$  –assuming general relativity (GR)– which is difficult to achieve in any model with non-negative DE density [34]. In another study [205], in line with this, it was argued that the Ly- $\alpha$  data can be accommodated by a physically

motivated modified gravity model that alters  $H(z)$  itself, and also that a further tension relevant to the Ly- $\alpha$  data can be alleviated in models in which  $\Lambda$  is dynamically screened, implying an effective DE passing below zero and concurrently exhibiting a pole in its equation of state (EoS), at  $z \sim 2.4$ . DE models –either as a physical source or an effective source arising from a modified theory of gravity– assumes negative energy density values have not been paid much attention so far (for reviews on DE and modified theories of gravity [77, 62, 71, 87, 63, 174, 173]). However, such scenarios are in fact familiar from an effective source (say, DE) defined by the collection of all modifications to the usual Einstein field equations in scalar-tensor theories, namely, when the cosmological gravitational coupling strength gets weaker with increasing redshift [47, 208]. A range of other examples of effective sources crossing below zero also exist, including theories in which  $\Lambda$  relaxes from a large initial value via an adjustment mechanism [96, 41], in cosmological models based on Gauss-Bonnet gravity [262], in braneworld models [206, 55], in loop quantum cosmology [29, 30], in higher-dimensional cosmologies that accommodate dynamical reduction of the internal space [69, 91, 13, 202], and generalisations of the form of the matter Lagrangian in a non-linear way [15, 46, 9].

It is possible to seek such scenarios by following a minimalist approach, namely, starting with the minimal extensions to the standard  $\Lambda$ CDM model. The most natural one to consider is the addition of positive spatial curvature, e.g., that of the Friedmann-Robertson-Walker (FRW) spacetime which imitates a negative energy density source with an EoS parameter equal to  $-1/3$ . It is easy to check that, however, to screen  $\Lambda$  at, e.g.,  $z \sim 2.4$  for  $\Omega_{\Lambda,0} \sim 0.7$ , its density parameter today is required to be  $\Omega_{k,0} \sim -0.06$ , which is a contradiction to the inflationary paradigm and is indeed not allowed by the joint results of the Planck release [6] suggesting spatial flatness to a  $1\sigma$  accuracy of 0.2%. By staying loyal to the inflationary paradigm and then suppose flat space, the simplest source that can realise such a behaviour can be obtained by promoting the null *inertial mass density* [113, 101] of the vacuum energy ( $\rho_{\text{inert}} = 0$ ) to a negative constant,  $\rho_{\text{inert}} = \text{const} < 0$ . The source  $\rho_{\text{inert}} = \text{const}$  has recently been of interest to many as it mimics  $\Lambda$  today while leading the universe to exhibit a future singularity dubbed as the Little Sibling of the Big Rip for  $\rho_{\text{inert}} = \text{const} < 0$  and a finite future bounce for  $\rho_{\text{inert}} = \text{const} > 0$  [53, 52]. However, in the light of observational analyses carried out in this work,  $\rho_{\text{inert}} = \text{const} < 0$  provides us with neither a superior DE model than  $\Lambda$ , nor an improvement regarding the tensions of interest. For instance, the observational data suggest that its energy density changes sign at a redshift larger than 65 (i.e., when it is already negligible) and it is indistinguishable from  $\Lambda$  today ( $z \sim 0$ ), so it cannot have consequences on the tensions. The simplest next step may be to consider the minimum *dynamical* deviation from the null inertial mass density in the form  $\rho_{\text{inert}} \propto \rho^\lambda < 0$

with  $\lambda$  being a real constant. The exponent  $\lambda$  here will provide a more featured evolution of the energy density passing below zero at high redshifts. Importantly, for arbitrarily large negative values of  $\lambda$ , it resembles a step function in redshift describing a spontaneously sign switching cosmological constant at a certain redshift. It can also be viewed as a phenomenological model described by a smooth function for approximately describing a vacuum energy that switches sign at a certain redshift and becomes positive just recently in the late universe and triggers the acceleration. A source having this form (but considering  $\rho_{\text{inert}} \propto \rho^\lambda > 0$ ) was first suggested in [37] (see also [38, 39]) for introducing an intermediate inflationary scenario named *graduated inflation*.

Accordingly, this source shall be named *graduated dark energy* (gDE) as in this chapter the present-day acceleration of the universe is studied. In fact, more recently, it has also been considered as a DE (e.g., [170, 222, 221, 107]). However, all these works focus on the future singularities and the asymptotic dynamics of the universe by retaining the positivity of the energy density (the cases for the negative energy density are discussed only superficially). In contrast, here, the focus is on its dynamics around the present time and then utilise its sign-switching energy-density feature to address the tensions that arise within  $\Lambda$ CDM model when the data from the late universe are considered.

Such scenarios, in particular, the sign-switching cosmological constant that arises as a limiting case of the gDE, can be extremely appealing from a string theoretic perspective. Constructing metastable de Sitter (dS) vacua (provided by  $\Lambda > 0$ ) has notoriously been a challenging task in string theory and, so far, has not have been concretely achieved [153, 214, 82, 246, 83, 81, 66, 84, 86, 70]. This has led many to suggest that string theory might not have any dS vacua at all [229, 85, 178, 110, 180, 184]. This would have immense implications in cosmology and/or theoretical physics, as it seems to imply an inconsistency between string theory and the universe we live in [137, 7, 28, 177, 129, 141, 19, 166, 124, 140, 74]. In contrast, an AdS (anti-de Sitter) background (provided by  $\Lambda < 0$ ) solution naturally arises in string theory or string theory motivated supergravities with broken/unbroken supersymmetry. Furthermore, the AdS space provides a very powerful setup to study various strongly coupled quantum field theories via the AdS/CFT (conformal field theory) correspondence [152, 245]. Contrary to the case of dS, which can only arise with broken supersymmetry, there does seem to exist a large number of consistent AdS backgrounds that can be obtained from string theory. It has also recently been claimed that transition from AdS vacua to dS vacua could be realised in a noncommutative quantum field theory setup [108]. Consequently, if one could show through gDE, that the observational data prefers a DE having  $\rho \sim \rho_0 > 0$  (positive cosmological constant) for  $z \sim 0$

(just recently) and  $\rho \sim -\rho_0 < 0$  (negative cosmological constant) for  $z \gg 0$  (most of the history of the universe), which realises at large negative  $\lambda$  values of gDE, and that the persistent tensions arising within the standard  $\Lambda$ CDM model disappear/relax, this would have far reaching implications for our understanding of the fundamental laws of physics. It will be shown that the observational data provides strong pointers in this direction. This leads to the conjecture that the cosmological constant has spontaneously switched sign and became positive, namely, the universe has transitioned from AdS vacua to dS vacua, at  $z \sim 2.3$  and triggered the observed late-time acceleration, and looking for such mechanisms in string theory is suggested.

### 3.2 Graduated dark energy

Inspired by [37], a type of DE model is defined, named as *graduated Dark Energy* (gDE), which yields an inertial mass density exhibiting power-law dependence to its energy density as follows;

$$\rho_{\text{inert}} = \gamma \rho_0 \left( \frac{\rho}{\rho_0} \right)^\lambda, \quad (3.1)$$

where  $\rho_0$  is positive definite (throughout the chapter, subscript 0 attached to any quantity denotes its value today), the parameters  $\gamma$  and  $\lambda$  are real constants. This can be viewed as characterising the minimum dynamical deviation from the null inertial mass density from the conventional vacuum energy. So that equation of state (EoS) parameter is  $w = p/\rho = -1 + \rho_{\text{inert}}/\rho$ , and reads

$$w = -1 + \gamma \left( \frac{\rho}{\rho_0} \right)^{\lambda-1}. \quad (3.2)$$

We note that  $\gamma = 0$  corresponds to the conventional vacuum energy with  $w = -1$  (leading to the  $\Lambda$ CDM model) and  $\lambda = 1$  corresponds to the perfect fluid with constant EoS parameter  $w = -1 + \gamma = \text{const}$  (leading to the  $w$ CDM model). From the continuity equation (1.26), this leads to  $d\rho + 3\gamma\rho_0 \left( \frac{\rho}{\rho_0} \right)^\lambda \frac{da}{a} = 0$ , which is solved by

$$\rho = \rho_0 [1 + 3\gamma(\lambda - 1) \ln a]^{\frac{1}{1-\lambda}}, \quad (3.3)$$

which satisfies

$$\rho_{\text{inert}} = \gamma \rho_0 [1 + 3\gamma(\lambda - 1) \ln a]^{\frac{\lambda}{1-\lambda}}, \quad (3.4)$$

$$w = -1 + \frac{\gamma}{1 + 3\gamma(\lambda - 1) \ln a}. \quad (3.5)$$

We note that  $w = -1 + \gamma$  today (when  $a = 1$  or redshift  $z \equiv -1 + \frac{1}{a} = 0$ ) and  $w \approx -1$  for sufficiently large and small  $a$ , in particular,  $w \rightarrow -1$  in the far future ( $a \rightarrow \infty$ ) and in

the very early universe ( $a \rightarrow 0$ ). Besides, provided that the parameters  $\gamma$  and  $\lambda$  are chosen appropriately, gDE can achieve a transition from  $\rho > 0$  to  $\rho < 0$  at a certain redshift. Thus, gDE can also be viewed as a phenomenological parameterization described by a smooth function for approximately describing the cosmological constant switches sign at a certain redshift and, for instance, becomes positive just recently in the late universe.

The gDE (3.3), in fact, exhibits various types of dynamics depending on its free parameters  $\lambda$  and  $\gamma$ , see [222] for a comprehensive investigation. In this work, the interest is in the case its energy density passes below zero at high redshifts, which, so far, has not been paid much attention, yet it is the case fitting the scenarios discussed in the Introduction 3.1 that most likely address the tensions relevant to  $H_0$  and, in particular, to the high-precision Ly- $\alpha$  data from  $z \approx 2.34$ . For instance, in the case  $\lambda = 0$  ( $\rho_{\text{inert}} = \gamma\rho_0$ ), (3.3) reduces to  $\rho = \rho_0 - 3\rho_0\gamma \ln a$ , consisting of a constant  $\rho_0 > 0$  mimicking  $\Lambda > 0$  and a dynamically screening term,  $-3\rho_0\gamma \ln a$ , in the past for  $\gamma < 0$ , viz.,  $\rho_0 - 3\rho_0\gamma \ln a = 0$  at  $a = e^{\frac{1}{3\gamma}}$ . Yet, the presence of the exponent  $\frac{1}{1-\lambda}$  in (3.3) will allow us to realise such a scenario with additional features.

First, we define  $\rho/\rho_0 = x^y$  along with  $\rho_0 > 0$ , where  $x \equiv 1 + 3\gamma(\lambda - 1) \ln a$  and  $y \equiv \frac{1}{1-\lambda}$ . We note that, unless  $\gamma = 0$  (conventional vacuum) or  $\lambda = 1$  (perfect fluid with constant EoS parameter),  $x$  changes sign at

$$a = a_* \equiv e^{-\frac{1}{3} \frac{1}{\gamma(\lambda-1)}}, \quad (3.6)$$

which is in the past ( $a_* < 1$ , the case of interest) for  $\gamma(\lambda - 1) > 0$ , and in the future ( $a_* > 1$ ) for  $\gamma(\lambda - 1) < 0$ . Next,  $y < 0$  for  $\lambda > 1$  so that  $\rho \rightarrow \pm\infty$  as  $a \rightarrow a_*$  and  $y > 0$  for  $\lambda < 1$  so that  $\rho \rightarrow 0$  as  $a \rightarrow a_*$ , where the latter case is the one of interest. Thus, let's proceed with the following two conditions:

$$\lambda < 1 \quad \text{and} \quad \gamma < 0, \quad (3.7)$$

the latter of which implies  $w(a = 1) < -1$ , i.e., the gDE must be in the phantom region today.

To get around a mathematical obstacle, when investigating gDE computationally, one continues by writing  $\frac{\rho}{\rho_0} = x^y$  in an equivalent way as  $\frac{\rho}{\rho_0} = \text{sgn}(x) |x|^y$  for  $y = \frac{m}{n}$  with  $m$  and  $n$  being odd integers, namely,

$$\rho = \rho_0 \text{sgn}[1 - \Psi \ln a] |1 - \Psi \ln a|^{\frac{1}{1-\lambda}}, \quad (3.8)$$

for  $\Psi \equiv -3\gamma(\lambda - 1) < 0$  (i.e.,  $\gamma < 0$ ),  $\lambda < 1$  and the exponent  $\frac{1}{1-\lambda} = \frac{m}{n}$  with both  $m$  and  $n$  being odd integers. For practical reasons, it is better to consider  $m = 1$  and so  $\lambda = -2N$  with  $N = 0, 1, 2, \dots$ , i.e.,  $\lambda = 0, -2, -4, \dots$ . Here  $\text{sgn}$  is the signum function that reads  $\text{sgn}(x) = -1, 0, 1$

for  $x < 0$ ,  $x = 0$  and  $x > 0$ , respectively. Of course, in principle, there is an infinite number of such  $\lambda$  values, not continuous, between the ones listed above, and so one can treat  $\lambda$  in (3.8) as if it is continuous since one can always find an allowed  $\lambda$  value indistinguishably close to a forbidden  $\lambda$  value.

Consequently, the gDE-CDM model replaces the  $\Lambda$  of the Friedmann equation of the standard  $\Lambda$ CDM model by the gDE (3.8) taking the form of

$$\frac{H^2}{H_0^2} = \Omega_{r,0} a^{-4} + \Omega_{m,0} a^{-3} + \Omega_{\text{DE},0} \text{sgn}[1 - \Psi \ln a] |1 - \Psi \ln a|^{\frac{1}{1-\lambda}}, \quad (3.9)$$

and one can rewrite

$$\frac{\rho_{\text{DE}}}{\rho_{c,0}} = \Omega_{\text{DE},0} \text{sgn}[1 - \Psi \ln a] |1 - \Psi \ln a|^{\frac{1}{1-\lambda}}, \quad (3.10)$$

where  $\Psi < 0$  and  $\lambda = 0, -2, -4, \dots$

Regarding inertial mass density (3.4); when  $\gamma < 0$ , if  $1 - \lambda$  is odd then  $\lambda$  is even, and consequently we have the exponent  $\frac{\lambda}{1-\lambda} = \frac{[\text{even}]}{[\text{odd}]}$  in (3.4), which in turn implies that  $\rho_{\text{inert}} \leq 0$ , then

$$\rho_{\text{inert}} = \gamma \rho_0 |1 + 3\gamma(\lambda - 1) \ln a|^{\frac{\lambda}{1-\lambda}}, \quad (3.11)$$

under the conditions derived above. It turns out that  $\rho_{\text{inert}} = 0$  is the upper bound  $\rho_{\text{inert,max}} = 0$ .

It was claimed above that gDE can also be viewed as a phenomenological model described by a smooth function that approximately describes the cosmological constant switching sign at a certain redshift and becoming positive just recently in the late universe. Indeed, under the conditions one can consider,  $\rho(a = 1) > 0$  and  $\rho(a \ll a_*)/\rho(a \gg a_*) \approx -1$  along with  $w(a \ll a_*) \approx w(a \gg a_*) \approx -1$ , which imply that the energy density of the gDE at high redshifts not only passes below zero but also settles in a value almost equal to the negative of its present time value and remains almost there all the way to the early times before which gDE is irrelevant to the dynamics of the universe anymore. Note that the EoS parameter is just slightly below (above) the phantom divide line for  $a \gg a_*$  ( $a \ll a_*$ ) with  $a_* < 1$ , and  $w \rightarrow -1$  only when either  $a \rightarrow 0$  or  $a \rightarrow \infty$ . Therefore, the energy density of gDE grows very slowly in the future and reaches arbitrarily large values in the very remote future, and also grows in negative values very slowly (much slower than radiation and dust, both which then eventually dominate gDE in the finite past) with the increasing redshift for  $a \ll a_*$ , and reaches arbitrarily large negative values in the beginning of the universe. It is important to note, however, that for arbitrarily large negative values of  $\lambda$ , the energy density equation (3.10) (or (3.8)) transforms into a step



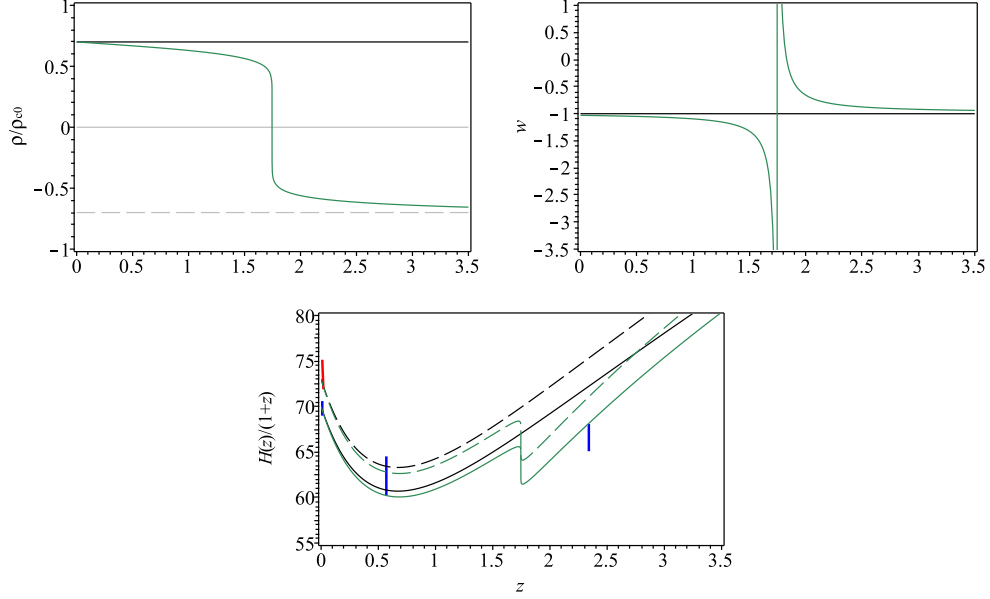


Figure 3.1:  $\Omega_{m,0} = 0.30$  is used and, for gDE-CDM,  $\gamma = -0.03$  along with  $\lambda = -10$  (green).  $H(z)/(1+z)$  vs.  $z$  for the gDE-CDM (green) and  $\Lambda$ CDM (black).  $H_0 = 70 \text{ km s}^{-1} \text{ Mpc}^{-1}$  (solid) and  $H_0 = 73 \text{ km s}^{-1} \text{ Mpc}^{-1}$  (dashed).  $H_0 = 69.8 \pm 0.8 \text{ km s}^{-1} \text{ Mpc}^{-1}$  from the TRGB  $H_0$  [109],  $H(z = 0.57) = 97.9 \pm 3.4 \text{ km s}^{-1} \text{ Mpc}^{-1}$  [27], and  $H(z = 2.34) = 222.4 \pm 5.0 \text{ km s}^{-1} \text{ Mpc}^{-1}$  from the latest BAO data [90].  $H_0 = 73.52 \pm 1.62 \text{ km s}^{-1} \text{ Mpc}^{-1}$  is independent measurement from Gaia parallaxes [200].

function;

$$\frac{\rho_{\text{DE}}}{\rho_{c,0}} \rightarrow \Omega_{\text{DE},0} \text{sgn}[1 - \Psi \ln a] \quad \text{as } \lambda \rightarrow -\infty \quad (3.12)$$

with an EoS parameter  $w \rightarrow -1$ . In this case, the energy density of gDE is non-dynamical except that it spontaneously changes sign at  $a = a_*$ . Thus, for large negative values of  $\lambda$ , gDE model is a very good approximation for describing a cosmological constant spontaneously switching sign at  $z = z_*$  in the limit  $\lambda \rightarrow -\infty$ ,  $\frac{\rho_{\text{DE}}}{\rho_{c,0}} = \Omega_{\text{DE},0}$  for  $z < z_*$  and  $\frac{\rho_{\text{DE}}}{\rho_{c,0}} = -\Omega_{\text{DE},0}$  for  $z > z_*$ .

The following may be useful as a demonstration of how gDE-CDM model works and gives a guide to the values of the parameters of the model. Let's choose  $a_* = e^{-1}$  ( $z_* \sim 1.7$ ) in line with [34] (see Fig.11 in [34]). This leads to  $\lambda = 1 + \frac{1}{3\gamma}$ , where  $\lambda$  must be a large negative number as  $\gamma \sim 0$  must be used (it is observationally well known that  $\gamma = w_0 + 1 \sim 0$ ) along with  $\gamma < 0$  (the condition derived above). For example,  $\gamma = -0.03$  (or  $w_0 = -1.03$ ) predicted by the Planck release [6] leads to  $\lambda \sim -10$ . Accordingly, in Fig. 3.1, it is depicted  $\frac{\rho(z)}{\rho_{c,0}}$ ,  $w(z)$  and  $H(z)/(1+z)$  by considering  $\Omega_{m,0} = 0.30$  along with two different Hubble constant values,  $H_0 = 70 \text{ km s}^{-1} \text{ Mpc}^{-1}$  and  $H_0 = 73 \text{ km s}^{-1} \text{ Mpc}^{-1}$ , for both the  $\Lambda$ CDM model and gDE-CDM model with  $\lambda = -10$  and  $\gamma = -0.03$ . We note that, in the gDE-CDM model, the steep change

in  $H(z)/(1+z)$  at  $z \sim z_* = 1.7$  allows it to pass through all data points as well as achieve larger  $H_0$  values, whereas in the case of the  $\Lambda$ CDM model, it does not pass through Ly- $\alpha$  data at  $z = 2.34$  and the increased  $H_0$  value worsens this situation. This is signalling that the gDE would lead to improved fit to the observational data and alleviate the tensions of various degrees of significance between some existing data sets within the  $\Lambda$ CDM cosmology. As, in the gDE-CDM model, we have  $\rho \sim \rho_0$  and  $w \lesssim -1$  (slightly in phantom region) for  $z \ll z_*$  (also for  $z \sim 0$ ) and  $\rho \sim -\rho_0$  and  $w \gtrsim -1$  (slightly in quintessence region with negative energy density) for  $z \gg z_*$ , from phenomenological point of view such an achievement may be signalling that indeed the cosmological constant is responsible for the current acceleration of the universe, but it has changed sign at  $z_* \sim 2$  and was negative at the higher redshifts.

### 3.3 Constraints from the latest cosmological data

This section provides constraints on the gDE-CDM model using the latest (at the time) observational data with a further discussion of the model and its consequences.

In order to perform the parameter-space exploration we use (as mentioned before) SimpleMC [\[1\]](#) [\[34\]](#). The SimpleMC code takes into account a compressed version of recent datasets, for instance the Planck information (PLK) (where the CMB is treated as a “BAO experiment” at redshift  $z = 1100$ ) measured by the angular scale of the sound horizon at that time, the analysis of Type Ia supernova (SN) data from the Joint Light-curve Analysis compressed into a piece-wise linear function fit over 30 bins evenly spaced in  $\log z$ , and high-precision Baryon Acoustic Oscillation measurements (BAO), from comoving angular diameter distances, Hubble distance and the volume averaged distance, at different redshifts up to  $z = 2.36$ . For a more detailed description about the datasets used see [\[34\]](#). A collection of currently available cosmic chronometer measurements ( $H$ ) is also included, see [\[115\]](#).

In this analysis, the radiation content is assumed by considering three neutrino species ( $N_{\text{eff}} = 3.046$ ) with minimum allowed mass  $\sum m_\nu = 0.06 \text{ eV}$  and a radiation density parameter given by  $\Omega_{\text{r},0} = 2.469 \times 10^{-5} h^{-2} (1 + 0.2271 N_{\text{eff}})$ , where  $h$  is the present-day value of the dimensionless reduced Hubble parameter  $h(z) = H(z)/100 \text{ km s}^{-1} \text{ Mpc}^{-1}$ . The total radiation content today is kept fixed in the analysis since it is well constrained by the CMB monopole temperature,  $T_{\text{CMB},0} = 2.7255 \pm 0.0006 \text{ K}$  [\[106\]](#). Throughout the analysis flat priors are assumed over the sampling parameters:  $\Omega_{\text{m},0} = [0.05, 1.0]$  for the matter density parameter today,  $\Omega_{\text{b},0} h^2 = [0.02, 0.025]$  for the physical baryon density parameter and  $h = [0.4, 1.0]$  for the reduced Hubble constant. With regards to the gDE parameters,  $\gamma = [-0.2, 0]$  and  $\lambda = [-27, 0]$  (when  $\lambda$  is free).

$\lambda$	$\Omega_{m,0}$	$h$	$\gamma = w_0 + 1$	$\Psi$	$z_*$	$t_0[\text{Gyr}]$	$-2\Delta \ln \mathcal{L}_{\text{max}}$
$\Lambda\text{CDM}$	0.302(6)	0.682(5)	0	0	–	13.806(22)	0.0
0	0.297(7)	0.689(7)	$> -0.08$	$> -0.25$	–	13.796(24)	0.02
–2	0.297(7)	0.688(7)	$> -0.06$	$> -0.61$	–	13.795(25)	0.02
–4	0.289(6), 0.298(7)	0.700(9), 0.686(7)	$-0.057(2), > -0.048$	$-0.86(3), > -0.73$	2.31(12),–	13.714(25), 13.791(26)	1.0, 0.02
–6	0.292(6), 0.299(6)	0.699(9), 0.685(7)	$-0.039(1), > -0.037$	$-0.86(3), > -0.77$	2.31(12),–	13.715(25), 13.792(27)	2.0, 0.01
–10	0.294(6), 0.299(6)	0.696(8), 0.684(7)	$-0.025(1), > -0.021$	$-0.86(3), > -0.69$	2.32(12),–	13.722(27), 13.797(25)	4.4, 0.02
–14	0.296(6), 0.300(6)	0.695(8), 0.683(7)	$-0.019(1), > -0.017$	$-0.86(3), > -0.76$	2.33(12),–	13.719(31), 13.794(27)	5.3, 0.01
–20	0.297(6), 0.300(6)	0.696(9), 0.683(7)	$-0.013(1), > -0.012$	$-0.86(3), > -0.76$	2.32(12),–	13.718(31), 13.795(26)	6.0, 0.02
–17.9(5.8)	0.296(6), 0.299(7)	0.697(9), 0.684(8)	$-0.017(8), > -0.074$	$-0.85(4), > -0.69$	2.32(19),–	13.719(30), 13.795(24)	6.4, 0.01

Table 3.1: Mean values along with  $1\sigma$  constraints on the set of parameters used to describe the gDE-CDM parameters. For one-tailed distributions the upper limit 95% C.L. is given. For two-tailed the 68% C.L. is shown. The last column,  $-2\ln(\mathcal{L}_{\Lambda,\text{max}}/\mathcal{L}_{\text{gDE,max}})$ , is used to compute best-fit differences of gDE-CDM from  $\Lambda\text{CDM}$  ( $-2\ln \mathcal{L}_{\Lambda,\text{max}} = 73.44$ ) based on the improvement in the fit alone.

Table 3.1 summarises the observational constraints on the free parameters  $\Omega_{m,0}$ ,  $h$ ,  $\lambda$  and  $\gamma$ , as well as the derived parameters  $\Psi$ ,  $z_*$  and  $t_0$  (age of the universe today), of the gDE-CDM model using the combined datasets PLK+BAO+SN+ $H$ ; and for comparison shows those parameters used on the standard  $\Lambda\text{CDM}$  model ( $\gamma = 0$ ). The columns for each parameter contain the corresponding mean values and  $1\sigma$  errors, according to the number of modes presented on the 1D marginalised posterior distributions. In the last column the  $-2\Delta \ln \mathcal{L}_{\text{max}} = \Delta\chi_{\text{min}}^2$  values representing the improvement in the fit to the data are listed w.r.t. the  $\Lambda\text{CDM}$ . At the outset, one immediately notices that in the analyses the gDE leads to an improvement of up to  $\Delta\chi_{\text{min}}^2 = 6.4$  (corresponding to about  $2.5\sigma$ ) when comparing it with the cosmological constant. In what follows it is discussed in detail how this significant improvement is due to the fact that the gDE-CDM alleviates some of the tensions the  $\Lambda\text{CDM}$  experiences.

In Table 3.1, for  $\lambda = 0, -2$ , there is nothing interesting and no significant improvement to the fit w.r.t.  $\Lambda\text{CDM}$ , viz.,  $\Delta\chi_{\text{min}}^2 < 0.02$ . However, one can observe that something surprising occurs when  $\lambda \leq -4$  (also when  $\lambda$  is free) that the data predict bimodal posterior probability distributions for the parameters of the gDE-CDM, for which one can observe two sets of constraint values in each column of Table 3.1. This may also be seen, for example, from the top left panel of Fig. 3.2 which displays 1D marginalised posterior distributions for the  $\gamma$  parameters. Notice that, for  $\lambda \leq -4$ , as we move towards the larger negative values of  $\gamma$ , the existence of a second (new) maximum starts appearing significantly far away from  $\gamma = 0$  ( $\Lambda\text{CDM}$ ). The first (old) maximum containing  $\gamma = 0$  is always there, but, when  $\lambda \leq -6$ , it consistently shrinks

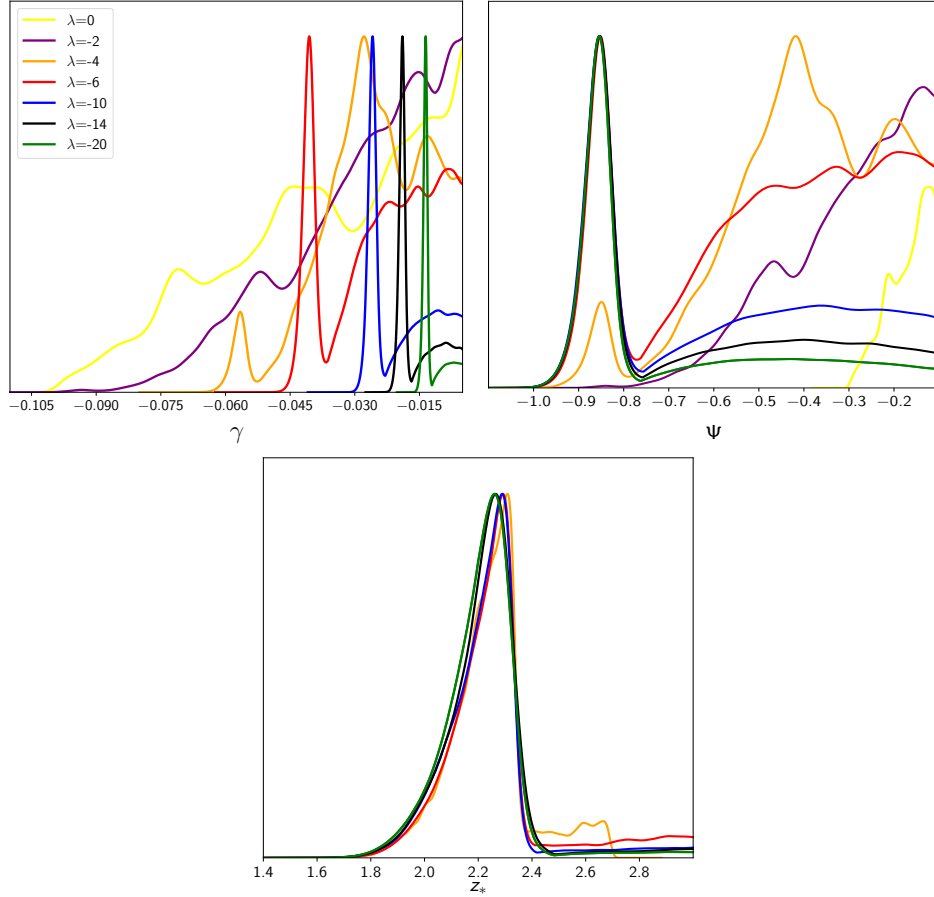


Figure 3.2: 1D marginalised posterior distributions for the graduated  $\gamma$  parameter (top left panel),  $\Psi \equiv 3\gamma(1 - \lambda)$  (right) and the redshift location of the pole (if present) given by Eqn. (3.13). For a better display some particular cases of  $\lambda$  values are included.

with the larger negative values of  $\lambda$ , during which the new maximum is getting relatively higher and sharper. This implies that the data significantly favour the new maximum over the old maximum when  $\lambda \lesssim -6$ . Indeed, we read from Table 3.1 that the improvement in the fit w.r.t.  $\Lambda$ CDM reaches highly significant levels –e.g.,  $\Delta\chi_{\min}^2 = 6$  when  $\lambda = -20$  and  $\Delta\chi_{\min}^2 = 6.4$  when  $\lambda$  is free– for the new maximum, while it remains always at insignificant levels  $-\Delta\chi_{\min}^2 \lesssim 0.02$  irrespective of the value of  $\lambda$ – for the old maximum. The poor improvement level of  $\Delta\chi_{\min}^2 \lesssim 0.02$  both in the old maximum (the maximum containing  $\gamma = 0$  when  $\lambda \lesssim -4$  and  $\lambda$  is free, and the single maximum when  $\lambda \lesssim 3$ ) presents no evidence for favouring these over the  $\Lambda$ CDM and the constraints on the parameters for these cases do not show a considerable deviation from those of the  $\Lambda$ CDM. Therefore, in what follows all these cases are discarded and proceed to the discussions with reference to the  $\Lambda$ CDM ( $\gamma = 0$ ), basically, by considering only the new maximum

that appears when  $\lambda \lesssim -6$ , e.g., by considering the one on the left of the pair of constraints given in a column for a parameter of the gDE-CDM in Table 3.1

The presence of these new maxima has important consequences and may be better explained through the expression (3.6). This expression indicates if there exists a sign change in the energy density of the gDE (or a pole in its EoS parameter), it will happen at a redshift

$$z_* = e^{-\frac{1}{\Psi}} - 1. \quad (3.13)$$

Hence, the quantity  $\Psi = -3\gamma(\lambda - 1)$  determines the position of the pole and, if it is a real one, must yield a unique value irrespective of the values  $\lambda$  and  $\gamma$ . That is, for a given  $\lambda$ , the  $\gamma$  parameter selects its best position such that  $\Psi$  remains unchanged, and this can be seen in the right-hand panel of Fig. 3.2 (see also Table 3.1). One can observe that a peak at  $\Psi = -0.86$ —significantly away from  $\Psi = 0$  ( $\Lambda$ CDM)—emerges when  $\lambda = -4$  and as  $\lambda$  takes more negative values (see the cases  $\lambda \leq -6$ ) it becomes significantly higher and sharper, fixed at  $\Psi = -0.86$ , while the old peak containing  $\Psi = 0$  becomes more prolate and lower. This implies highly significant observational evidence for the sign change of the energy density of the gDE (or pole in its EoS parameter) at the redshift corresponding to  $\Psi = -0.86$ . It is shown, according to (3.13), in the bottom panel of Fig. 3.2, the 1D marginalised posterior distribution of the redshift for this event persistently located at  $z_* \approx 2.32$  (see Table 3.1). Interestingly, but not surprisingly this particular position agrees with the location of the Ly- $\alpha$  auto and cross-correlation BAO ( $z = 2.34$ ) data and the works [90, 34, 205]. This suggests such a behaviour of DE for alleviating the tensions besetting this observation. We should note here that the peaks containing  $\Psi = 0$  ( $\Lambda$ CDM) also predict the sign change of the gDE, but they have been discarded for the following reasons. Firstly, these cases correspond to the ones discarded above, since they do not present any statistical evidence for being favoured over  $\Lambda$ CDM (the  $\Psi \rightarrow 0$  limit leading to  $z_* \rightarrow \infty$ ). Secondly, in the analyses, one can observe that these cases predict completely different  $z_*$  values for different  $\lambda$  values (if they were real the predictions need to have been stable at a certain redshift) and all of which are extremely large (even having redshift values larger than the redshift of the big bang nucleosynthesis epoch) at which dark energy is irrelevant to the cosmological dynamics.

The bimodal distribution that  $\Psi$  exhibits has a strong impact on the posterior distribution of  $h$ , and therefore on the Hubble constant  $H_0$ , which also exhibits a bimodal behaviour. Fig. 3.3 describes this behaviour; as soon as the  $\lambda$  parameter starts decreasing the bimodal distribution on the panel  $\{h, \Psi\}$  starts showing up for a particular  $\gamma$  value (display in pink colour). This bimodal distribution is summarised on the marginalised error bars shown in Fig. 3.4. One can

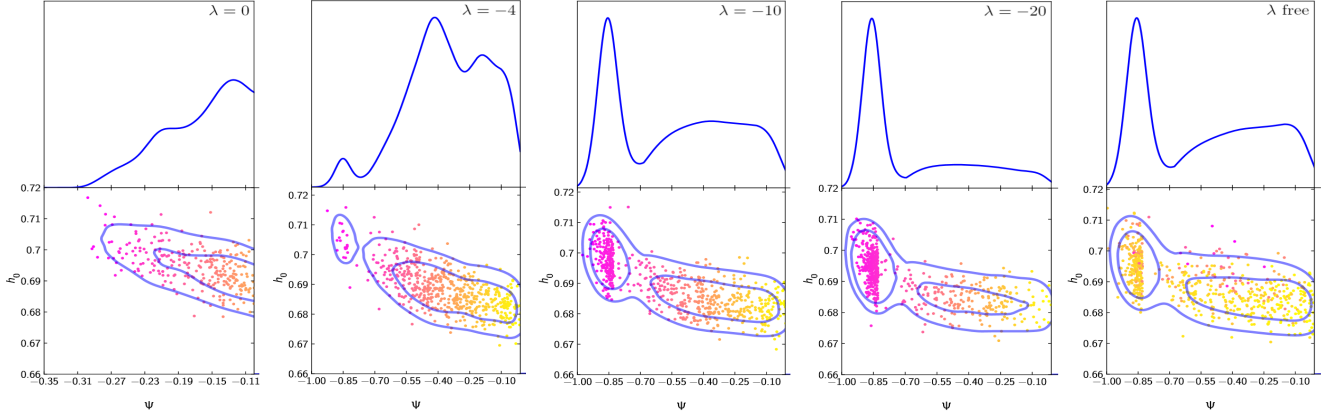


Figure 3.3: Top panel: 1D marginalised posterior distributions of  $\Psi$ , along with (bottom panel) 2D posterior distributions of  $\{\Psi, h_0\}$  colour coded by the  $\gamma$  parameter.

observe that while the values (green) associated with the old peak containing  $\Psi \sim 0$  ( $\Lambda$ CDM) agree with the  $H_0$  values measured from the inverse distance ladder (e.g.,  $H_0 = 67.4 \pm .5$  from Planck 2018 [6]), the ones (red) associated with the new peak stable at  $\Psi \sim -0.86$  (away from  $\Psi = 0$ ) agree with the higher  $H_0$  values measured from the distance ladder measurements (e.g.,  $H_0 = 69.8 \pm 0.8$  from a recent calibration of the Tip of the Red Giant Branch (TRGB) applied to Type Ia supernovae [109]). Therefore, the  $H_0$  predicted within the  $\Lambda$ CDM (matching the results from the old peak) has deficiency w.r.t. the TRGB  $H_0$  value, while the ones predicted by the new peak (appears for  $\lambda \lesssim -4$ ) perfectly match with it. It certainly favours the new peak that it predicts a value matching the independent TRGB  $H_0$  value. It is also significant that it uses the distance ladder approach, rather than the inverse distance ladder approach. Also, the latter BAO calibration of  $H_0$  is not completely independent of the Planck measurement, as both  $H_0$  determinations are based on the  $\Lambda$ CDM and its adopted value of the sound horizon scale. Moreover, the independent TRGB  $H_0$  value (so the values from the new peak) agrees with both Planck [6] and Cepheid [199, 200, 198]  $H_0$  values. However, when combined with Cepheid measurements the tension with the Planck value is relieved only at about  $\sim 1\sigma$  level and still remains significant [109].

We notice in Table 3.1 that the values of the parameters  $\Psi(\gamma, \lambda)$  –or  $z_*(\gamma, \lambda)$ – and of the other cosmological parameters  $\Omega_{m,0}$ ,  $h$  and  $t_0$  are quite stable for  $\lambda \leq -10$ . One may see from the last row in Table 3.1 that this observation is confirmed when the model is constrained by letting also the parameter  $\lambda$  free (with a flat prior  $\lambda = [-27, 0]$ ). Left panel of Fig. 3.5 displays the 3D marginalised posterior distribution of the  $\{\Psi, \lambda\}$  parameter region colour coded with the  $\gamma$

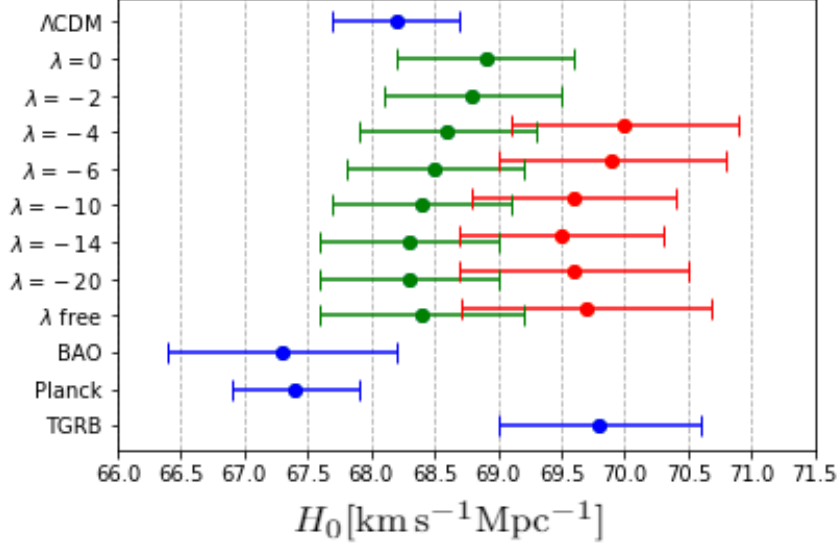


Figure 3.4: Means values along with  $1\sigma$  error bars from the 1D marginalised posterior distributions of  $H_0$  [km s $^{-1}$  Mpc $^{-1}$ ]. Green error bars are associated with the peak containing  $\Psi \sim 0$  ( $\Lambda$ CDM), whereas red with the new peak stable at  $\Psi \sim -0.86$ .

parameter. Here, the bimodality of the constraints on the gDE-CDM shows up as two detached 2D outer contours. The narrow one located at  $\Psi \sim -0.86$  corresponds to the new maximum, while the wide one corresponds to the old maximum containing the  $\Lambda$ CDM (top-right corner). In the right panel of the same figure the 1D posterior distribution of the  $z_*$  associated with the new maximum is presented, which demonstrates that the redshift at which the gDE energy density changes sign (its EoS parameter exhibits a pole) is stable at  $z_* \sim 2.32$ .

It was shown in [205] through the  $Om h^2$  diagnostic (introduced to test the  $\Lambda$  hypothesis in a model-independent way) that the  $\Lambda$ CDM is in tension with the BAO's statistically independent measurements of  $H(z)$  at redshifts of 0.57 and 2.34. It was shown that this tension is alleviated in models in which the  $\Lambda$  was dynamically screened in the past and that the energy density of such evolving DE models passes below zero (exhibits pole in the effective EoS) at  $z \sim 2.4$ . These are in line with the new maxima of the gDE-CDM, yet in addition the fact that the constant that plays the role of  $\Lambda$  in gDE is embedded into a parenthesis raised to a power renders the model more featured. Therefore, gDE in the context of  $Om h^2$  diagnostic is also investigated.

The  $Om h^2$  diagnostic is defined in [205] as follows:

$$Om h^2(z_i; z_j) = \frac{h^2(z_i) - h^2(z_j)}{(1+z_i)^3 - (1+z_j)^3}, \quad (3.14)$$

and depends only on  $H(z)$ . Accordingly, knowing it at two or more redshifts, one can obtain

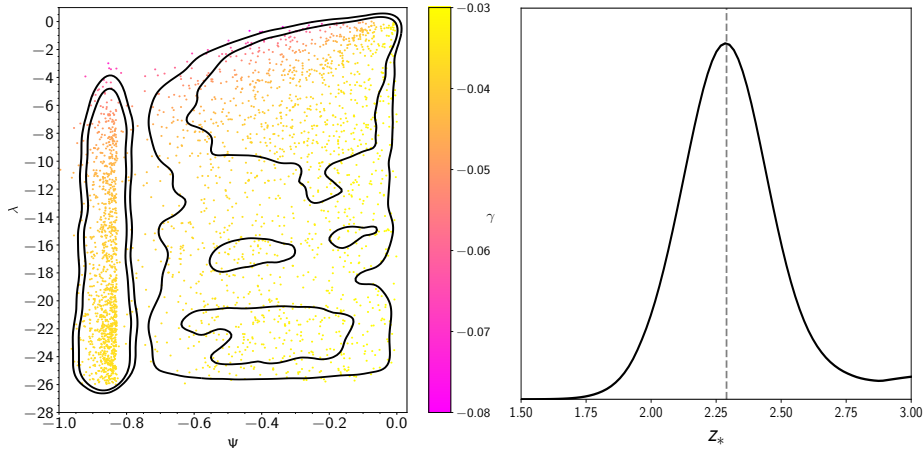


Figure 3.5: Graduated Dark energy model with varying the  $\lambda$  parameter. Left panel: 3D marginalised posterior distributions for the graduated  $\lambda$  and  $\Psi$  parameters, coloured coded by the  $\gamma$  parameter. Right panel: 1D marginalised posterior of the redshift position given by the pole. The vertical line is the mean value  $z_* = 2.32$ .

$Om h^2$  value(s) in a model-independent manner and thence conclude whether or not the DE is a  $\Lambda$ . For the  $\Lambda$ CDM, omitting radiation (negligible in the late universe), we have  $h^2 = h_0^2 [\Omega_{m,0}(1+z)^3 + 1 - \Omega_{m,0}]$  leading to a constant

$$Om h^2(z_i; z_j) = h_0^2 \Omega_{m,0}. \quad (3.15)$$

For the gDE-CDM, using (3.9), we have

$$Om h^2(z_i; z_j) = h^2 \Omega_{m,0} + h^2 (1 - \Omega_{m,0}) \frac{\text{sgn}(x_i) |x_i|^y - \text{sgn}(x_j) |x_j|^y}{(1+z_i)^3 - (1+z_j)^3}, \quad (3.16)$$

where we have neglected radiation and used the zero-curvature constraint,  $\Omega_{m,0} + \Omega_{DE,0} = 1$ . The second line of the  $Om h^2(z_i; z_j)$  for the gDE-CDM emerges as a correction to the one for the  $\Lambda$ CDM. We can calculate the predicted  $Om h^2(z_i; z_j)$  with these two equations for any pair of chosen redshifts using the constraints on the models and then compare the same with the model-independent estimates obtained by (3.14).

One can calculate, from (3.14), the model independent estimates as  $Om h^2(z_1; z_2) = 0.164 \pm 0.024$ ,  $Om h^2(z_1; z_3) = 0.123 \pm 0.006$  and  $Om h^2(z_2; z_3) = 0.119 \pm 0.007$  by using  $H(z_1 = 0) = 69.8 \pm 0.8 \text{ km s}^{-1} \text{ Mpc}^{-1}$  from the TRGB  $H_0$  [109],  $H(z_2 = 0.57) = 97.9 \pm 3.4 \text{ km s}^{-1} \text{ Mpc}^{-1}$  based on the clustering of galaxies in the SDSS-III BOSS DR11 [27], and  $H(z_3 = 2.34) = 222.4 \pm 5.0 \text{ km s}^{-1} \text{ Mpc}^{-1}$  based on the BAO in the Ly- $\alpha$  forest of SDSS DR11 data [90]. The constraint  $Om h^2 = 0.140 \pm 0.002$  ( $Om h^2 = 0.143 \pm 0.001$  in Planck 2018 [6]) obtained for the



$\lambda$	$Om h^2(z_1; z_2)$	$Om h^2(z_1; z_3)$	$Om h^2(z_2; z_3)$
$\Lambda$ CDM	0.140(2)	0.140(2)	0.140(2)
0	0.134(4)	0.139(4)	0.140(4)
-2	0.135(4)	0.140(2)	0.140(2)
-4	0.136(3)	0.129(1), 0.140(2)	0.129(2), 0.140(2)
-6	0.137(2)	0.128(1), 0.140(3)	0.127(2), 0.140(2)
-10	0.137(2), 0.139(2)	0.127(2), 0.140(2)	0.123(2), 0.140(2)
-14	0.138(2), 0.139(2)	0.126(2), 0.140(2)	0.127(2), 0.140(2)
-20	0.139(2), 0.140(2)	0.125(2), 0.140(2)	0.124(2), 0.140(2)
Free	0.136(4), 0.139(2)	0.127(4), 0.140(2)	0.126(2), 0.140(2)

Table 3.2: Mean values along with  $1-\sigma$  constraints on the set of parameters that describe  $Om$  diagnostic.

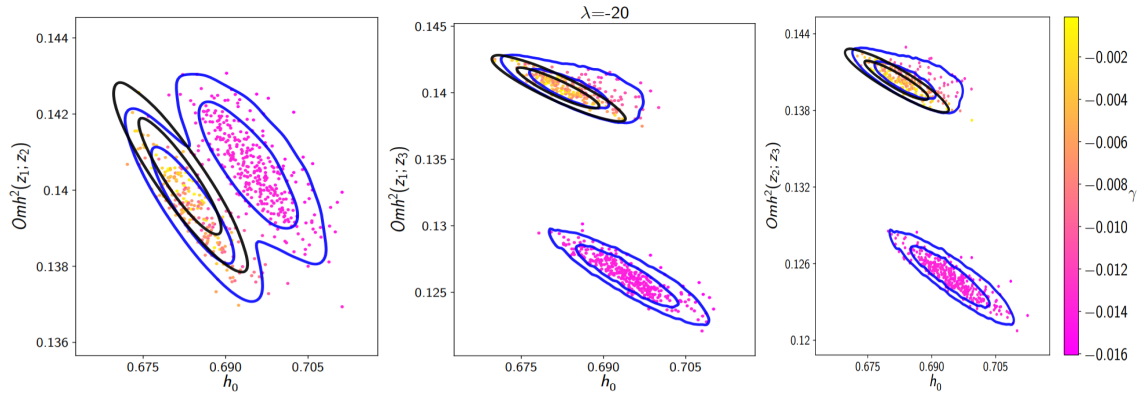


Figure 3.6:  $Om h^2$  diagnostic for the graduated dark energy model with  $\lambda = -20$  using three redshifts  $\{z_1, z_2\}$  (left),  $\{z_1, z_3\}$  (middle) and  $\{z_2, z_3\}$  (right). The colour code indicates the value of  $\gamma$  parameter, where the yellow points mimic the  $\Lambda$ CDM behaviour and the pink ones the new feature introduced by the gDE model.

$\Lambda$ CDM is in clear tension with the latter two of these estimates. In Table 3.1 is seen that, for  $\lambda \leq -10$  as well as the  $\lambda$  free case, the constraints for all of the three  $Om h^2$  exhibit bimodal characteristic, i.e., there are two valued constraints corresponding to the new (left) and old (right) maxima. One can notice  $Om h^2(z_1; z_2) \sim 0.140$  (as in the  $\Lambda$ CDM) almost the same for both the new and old maxima, yet it agrees with the corresponding model independent estimate. However, when considering  $Om h^2(z_1; z_3)$  and  $Om h^2(z_2; z_3)$  it is observed that while the ones associated with the new maximum yield  $\sim 0.125$  in agreement with the corresponding model independent estimates, the ones associated with the old maximum yield  $\approx 0.140$  in tension. For a visual demonstration, in Fig. 3.6, the marginalised posterior distributions for the

parameter  $\gamma$  in the  $\{\gamma, Omh^2(z_i; z_j), h\}$  subspace for  $\{z_1, z_2\}$ ,  $\{z_1, z_3\}$  and  $\{z_2, z_3\}$  are shown, where the blue contours and 3D scatter color plots described the gDE-CDM model for  $\lambda = -20$ . The color code indicates the value of  $\gamma$  labelled by the color bar. Black contours display 2D marginalised posterior distributions for the  $\Lambda$ CDM which agree with the position of the yellow points corresponding to the old maxima of the gDE-CDM. The contours at about  $Omh^2 \sim 0.125$  correspond to the new maxima of the gDE-CDM describing the case in which the energy density of the gDE passes below zero  $z \sim 2.32$ .

All these superiorities in goodness of fit to the observational data arising in the case of the new maxima of the gDE-CDM are obviously consequences of the fact that the energy density of the gDE passes below zero at  $z_* \approx 2.3$  by exhibiting a certain type of dynamics. By using the *fgivenx* package [125], in the upper panel of Fig. 3.7 the probability (more pink implies more probable) distribution of the redshift dependency of the energy density of gDE scaled to the critical energy density of the present-day universe, viz.,  $\rho_{\text{DE}}/\rho_{c,0}$  is shown. One can observe that gDE, viz.,  $\rho_{\text{DE}}(z)/\rho_{c,0}$ , does not distinguish from  $\Lambda$  (solid straight black line) at a value  $\sim 0.70$  for  $z \lesssim 2$ , but it reaches a junction at  $z \sim 2.3$  and for larger redshifts it either keeps tracking  $\Lambda$  by retaining the value  $\sim 0.70$  (the one associated with the old maximum and disfavoured by the data) or rapidly changes route and starts to track a new value  $\sim -0.70$  like a mirror image of the former track at  $\rho_{\text{DE}} = 0$  (the case associated with the new maximum and favoured by the data). The rapid sign switch of the gDE energy density at  $z \sim 2.3$  implies a rapid drop in the total energy density of the universe, and in  $H(z)$ , at that redshift. This behaviour of  $H(z)$  emerges in association with the new maxima of the gDE-CDM for more negative values of  $\lambda$ , as can be seen in the lower panel of Fig. 3.7, reconciles it with the lower  $H(z)$  value of the Ly- $\alpha$  data at  $z = 2.34$  with respect to the one predicted by  $\Lambda$ CDM for that redshift. Furthermore, this reconciliation between the gDE-CDM and Ly- $\alpha$  data, in turn, provides the gDE-CDM with easiness in achieving large  $H(z)$  values for  $z \lesssim 2$  and thereby predicts larger  $H_0$ , and so gDE-CDM relieves the  $H_0$  tension that  $\Lambda$ CDM has been suffering from.

### 3.4 Spontaneous sign switch in the cosmological constant

In this section, there will be some comments on the implication of the dynamics of gDE that leads to all these reconciliations with the observational data on the nature of the dark energy. First, one notes the following features of gDE. From Table 3.1 for larger negative values of  $\lambda$ ,  $\rho_{\text{DE}}/\rho_{c,0} = 0.70$  and  $w_0 \sim -1.01$  at  $z = 0$ , its energy density switches sign rapidly at  $z_* \approx 2.32$  (which is quite stable) and settles into a value  $\rho_{\text{DE}}/\rho_{c,0} \sim -0.70$  and remains there for  $z_* \gtrsim 2.3$ .

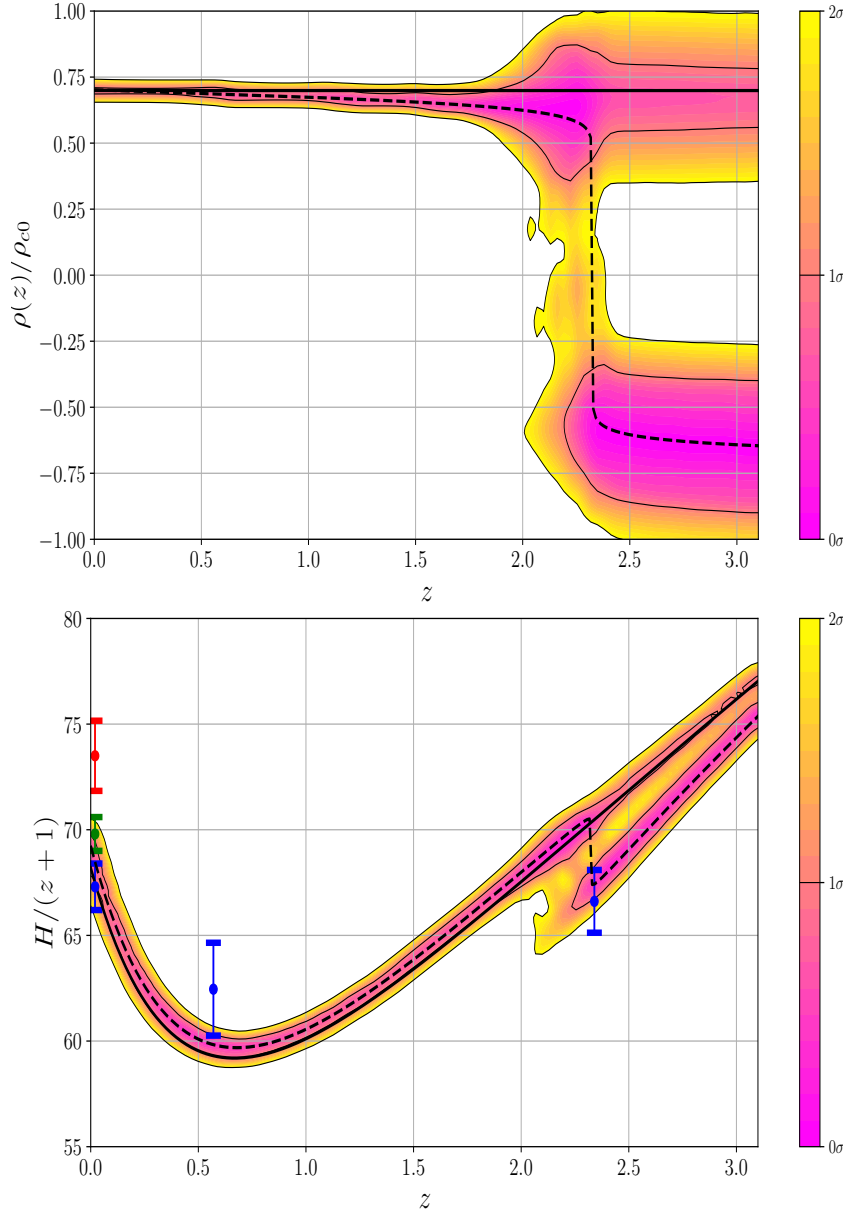


Figure 3.7: Top panel:  $\rho_{\text{gDE}}/\rho_{c0}$  versus redshift  $z$  for  $\lambda = -20$  displays the maximum predicted that  $\rho_{\text{gDE}}$  changes sign at  $z \sim 2.3$ . Bottom:  $H(z)/(1+z)$  function. Include the latest BAO data points [34] (blue bars) where  $H_0 = 67.3 \pm 1.1$ , the Planck 2018 [6]  $H_0 = 67.4 \pm 0.5$  data (red bar) and the TGRB model independent [109]  $H_0 = 69.8 \pm 0.8$  data (green bar). Black dashed line corresponds to best-fit values of gDE and solid black line corresponds to  $\Lambda$ CDM. We note that, due to the jump at  $z \sim 2.3$ , the gDE model is not in tension with the BAO Ly- $\alpha$  data from  $z = 2.34$  in contrast to  $\Lambda$ CDM model and also gDE gives larger  $H_0$  values w.r.t.  $\Lambda$ CDM model and thereby relaxes  $H_0$  tension.

Next, one can observe in the same table that the larger the negative values of  $\lambda$ , the better fit to the data (the larger  $\Delta\chi_{\min}^2$ ). This follows the trend that makes  $\rho_{\text{DE}}(z)$  increasingly resemble a step function centred at  $z_*$  with two branches yielding opposite values about zero (a pattern of flat positive energy density for  $z < z_*$  and flat negative energy density for  $z > z_*$ , both of which have the same absolute value) and indeed, we know from (3.12), that  $\rho_{\text{DE}}$  transforms into a step function for arbitrarily large negative values of  $\lambda$ . The largest negative  $\lambda$  value considered in the analyses is  $-27$ , yet it is easy to check mathematically that considering even larger negative values would not effect the results considerably since, for this value, the function  $\rho_{\text{DE}}(z)$  already closely resembles a step function. Thus, the results from the new maximum of the gDE for large negative values of  $\lambda$  can safely be interpreted as the results one would obtain for a cosmological constant that achieved its present-day positive value by spontaneously switching sign at  $z_* \sim 2.3$ , but was negative in the earlier stage of the universe.

Some general constraints that are typically applied to classical matter source, irrespective of its detailed description, may be utilised for further supporting this interpretation (see [113, 65]). Let us consider gDE as an actual barotropic fluid,  $p = p(\rho)$ , along with the best fit values obtained on its free parameters from the observational analysis. In this case, although it behaves almost like a cosmological constant (in spite of the fact that it switches sign at  $z \approx 2.32$ ) throughout the history of the universe, strictly speaking, it violates the weak energy condition, namely, the non-negativity conditions on the energy density,  $\rho \geq 0$ , for  $z > z_*$ , and on the inertial mass density,  $\rho_{\text{inert}} \geq 0$ , throughout the history of the universe. Moreover, there are periods during which it violates the condition  $0 \leq c_s^2 \leq 1$  on the speed of sound of a barotropic fluid given by the adiabatic formula  $c_s^2 = dp/d\rho$ . The upper limit (causality limit) is a rigorous one which cannot be violated unless we abandon relativity theory. The lower limit applies to a stable situation, and otherwise the fluid is classically unstable against small perturbations of its background energy density -the so called Laplacian (or gradient) instability. It is well known that phenomenological fluid models of DE are difficult to motivate, and adiabatic fluid models are typically unstable against perturbations, since  $c_s^2$  is usually negative for  $w < 0$ . It is possible to evade this constraint in non-adiabatic fluid descriptions (e.g., canonical scalar field for which the effective speed of sound -which governs the growth of inhomogeneities in the fluid- is equal to unity,  $c_{s\text{ eff}} = 1$ ), and in an adiabatic fluid if  $w$  decreases sufficiently fast as the universe expands (e.g., Chaplygin gas). However, with some exceptions, it is unlikely to describe gDE with a canonical scalar field -especially when we consider the best fit values. Also, gDE yields  $c_s^2 = -1 + \gamma\lambda \left(\frac{\rho}{\rho_0}\right)^{\lambda-1} = -1 + \frac{\gamma\lambda}{1+3\gamma(\lambda-1)\ln a}$ , and  $c_s^2(z=0) = -1 + \gamma\lambda$ . Accordingly, the constrains obtained when  $\lambda$  is free predict  $c_s^2(z=0) = -0.6957 \pm 0.1739$  for  $z=0$  and

$c_s^2 \gg 1$  while  $0 < \rho \ll \rho_0$  (just after gDE assumes positive values at  $z \approx 2.32$ ). On the other hand, whether it is positive or negative, a cosmological constant (viz., the limit  $\lambda \rightarrow -\infty$ , see (3.12)) is well behaved:  $\rho_{\text{inert}} = 0$ , and  $c_s^2 = 0$  (it has no speed of sound, and thereby does not support classical fluctuations). Regarding the negativity of its energy density (when  $z > z_*$ ), a negative cosmological constant is ubiquitous in the fundamental theoretical physics without any complication, for instance, it can be taken as just a geometrical component ( $\rho < 0$  will then be an effective energy density rather than an actual one), and it also is very natural from symmetry considerations and provides the ground state (AdS background) in various low energy limits of string theory.

Thus, bringing all these points together, it is tempting to conclude that the cosmological constant has spontaneously switched sign and become positive at  $z \approx 2.32$  and triggered the late-time acceleration. Of course, one could look for realising such a nontrivial behaviour of gDE as an effective source in a modified gravity model (the general constraints that are typically applied to classical matter source might then be evaded) and reach different conclusions.



## Chapter 4

# Model Independent Reconstructions of the Dark Energy

### 4.1 Introduction

As stated in chapter 2, even though parametric forms usually provide a better fit to the data, they have the limitation of assuming an *a priori* functional form which may lead to some bias or misleading model-dependent results, regardless of the nature of DE. To avoid these possible issues, non-parametric and model-independent techniques are used. They allow us to extract information directly from the data to detect features within cosmological functions. That is, the goal of non-parametric and model-independent approaches is to reconstruct (infer) an unknown quantity without a predefined shape.

The main aim of this chapter is to perform model-independent reconstructions of the dark energy features and to provide a model comparison through the Bayesian evidence and goodness-of-fit. The analysis is carried out among the nodal and bin reconstructions, an extension of the two of them where internal amplitudes are allowed to vary in height as well as in position, the correlation function method, and then, for comparison, to include some of the parametric proposals. Even though these techniques are applicable to any function describing the dark energy, the focus is on the EoS and the energy density. After the reconstruction is carried out, some of the cosmological functions can therefore be derived, i.e. Hubble parameter  $H(z)$ , deceleration parameter  $q(z)$  and the  $Om(z)$  diagnostic. Finally PCA is performed to discern possible important features from noise contributions.

The chapter is organized as follows: in section [4.2](#) the reconstruction methodology is described. Then in section [4.3](#) a brief review of the underlying theory, datasets and some specifications about the parameter estimation and model selection are provided. Finally in section [4.4](#) the main results are presented.

## 4.2 Reconstruction methodology

The reconstructions to be employed are the previously described Bins and Nodal methods. In both types of reconstructions the nodes are located in space at certain positions  $z_i$  and with variable amplitudes  $f_i$ .

Along with the usual approaches, a modified version of these reconstructions is used. This modification considers the internal positions  $z_i$  to be free parameters, which will allow it to capture more specific features at certain places [\[127, 31\]](#). Notice that in this version, the internal variable positions have to be sorted in a way to avoid possible overlapping in the reconstructions. This approach gives more degrees of freedom (one for each variable  $z_i$ ) to the reconstruction. When using the linear interpolation the expected behavior is straightforward, as it only varies the lines between nodes, however in the binning process it will affect the width of the bins, so it would be easier to find specific features on the positions rather than on the amplitudes.

Finally, there exists the possibility of either overfitting by using a very complex model with a large amount of bins (or nodes) or underfitting by not capturing enough features due to the use of just few bins (or nodes). Both of these possible issues can be managed by performing a model comparison among reconstructions through the Bayesian Evidence, that is, the impact of additional parameters and their priors is modulated to find out the most suitable to the data. This method follows the principle of simplicity and economy of explanation known as Occam's Razor [\[228\]](#) which states: "*the simplest theory compatible with the available evidence ought to be preferred*". The Correlation Function method will also be used when a large number of parameters are present to diminish the possibility of overfitting. Although to see if any possible bias due to this method may arise there will be an instance where it is not used (as seen in Fig. [4.4](#)).



## Bayesian statistics

In order to perform the parameter estimation we follow the definition of the Bayes Theorem

$$P(u|D, M) = \frac{\mathcal{L}(D|u, M)P(u|M)}{E(D|M)}, \quad (4.1)$$

being  $u$  the vector of parameters of the hypothesis  $M$  (or model) to assess,  $D$  is the experimental (observational) data,  $P(u|D, M)$  the posterior probability distribution,  $\mathcal{L}(D|u, M)$  the likelihood,  $P(u|M)$  the prior distribution and  $E(D|M)$  the Bayesian evidence. Once the Bayesian evidence is computed for two models  $M_1$  and  $M_2$ , the Bayes factor is defined as

$$B_{12} \equiv \frac{E(D|M_1)}{E(D|M_2)}. \quad (4.2)$$

This quotient, together with the Jeffrey's scale shown in Table [2.1](#) [\[228, 98\]](#), is a great empirical tool for performing model selection, that is, it gives an insight of how good a model  $M_1$  is when compared to model  $M_2$ . In this work,  $M_1$  will correspond to  $\Lambda$ CDM and  $M_2$  will be any of the reconstructions in order to make a direct comparison with the standard model. Even so, it is important to mention that Jeffreys' scale is empirical in nature and sometimes can rule out the true model [\[169\]](#); added to this we have the dependence of the Bayesian evidence on priors and on model constrains [\[138\]](#). So, even though it is a great tool for comparison, it should not be taken as completely decisive when performing model selection.

## 4.3 Theory and datasets

The important equations and concepts (regarding background cosmology) for this reconstruction will be now explained and presented. For a homogeneous and isotropic flat universe given by the Friedmann-Robertson-Walker metric, the Friedmann equation describing the dynamical evolution, in terms of redshift  $z$ , can be written as

$$\frac{H^2(z)}{H_0^2} = \Omega_{r,0}(1+z)^4 + \Omega_{m,0}(1+z)^3 + \Omega_\Lambda. \quad (4.3)$$

Here, we have the components of the universe written in terms of the dimensionless density parameters  $\Omega_i(z) \equiv \rho_i(z)/\rho_c(z)$ , where their contribution at the present time (represented by subscript 0) are  $\Omega_{r,0}$  for the relativistic particles,  $\Omega_{m,0}$  describes the matter content (baryons and dark matter) and  $\Omega_\Lambda$  is associated to the cosmological constant;  $\rho_c$  is the critical density of a spatially flat universe.

By letting aside the cosmological constant and allowing a dynamical dark energy component, the last term in the equation [\(4.3\)](#) is replaced by  $\Omega_\Lambda \rightarrow \rho_{DE}(z)/\rho_{c,0}$ . Furthermore, if the dark

energy is assumed to be a perfect fluid with a barotropic EoS, then once we compute the EoS we are able to derive the energy density through

$$\frac{\rho_{\text{DE}}(z)}{\rho_{c,0}} = \Omega_{\text{DE},0} e^{3 \int_0^z \frac{dz'}{1+z'} (1+w_{\text{DE}}(z'))}. \quad (4.4)$$

On the other hand, the dark energy density could, in general, come from an effective model contribution and not necessarily from a physical component. Hence  $\rho_{\text{DE}}(z)$  may have any shape (including negative values). Therefore, if the shape of  $\rho_{\text{DE}}(z)/\rho_{c,0}$  is obtained from any process, then we are able to derive its associated equation of state:

$$w_{\text{DE}}(z) = -1 + \frac{1}{3} \frac{d \ln \rho_{\text{DE}}(z)}{d \ln(1+z)}. \quad (4.5)$$

Finally, if the shape of the energy density is obtained, either directly or through  $w_{\text{DE}}(z)$ , we are able to compute some derived functions, for instance the  $Om$  diagnostic, which provides a null test for the cosmological constant [\[204\]](#)

$$Om(z) = \frac{h^2(x) - 1}{(x)^3 - 1}, \quad x = z + 1, \quad h(x) = \frac{H(x)}{H_0}, \quad (4.6)$$

and the deceleration parameter

$$q(z) = -1 + \frac{d \ln H}{d \ln(1+z)}. \quad (4.7)$$

In this chapter the reconstruction efforts will be aimed to both the density  $\rho_{\text{DE}}(z)$  and the EoS  $w_{\text{DE}}(z)$ .

## Data sets

In this chapter the full catalogue of 1048 supernovae from the Pantheon SN Ia sample is used, covering a redshift range of  $0 < z < 2$  [\[211\]](#) (written as SN in the datasets). The full covariance matrix associated is comprised of a statistical and a systematic part, and along with the data, they are provided in the repository [\[136\]](#).

A collection of cosmic chronometers will also be used [\[135, 215, 223, 160, 260, 158, 159\]](#) (written as H in the datasets) to perform the reconstructions, which can be found within the repository [\[151\]](#).

Finally also the BAO distance measurements will also be of use in this chapter. The sound horizon is calibrated by using Big Bang Nucleosynthesis [\[33\]](#). The BAO datasets used here contain the SDSS DR12 Galaxy Consensus, BOSS DR14 quasars (and eBOSS), Lyman- $\alpha$  DR14 auto-correlation, SDSS MGS and 6dFGS located at different redshifts up to 2.36. For a more

Model	$w_{\text{DE}}(z)$	$\rho_{\text{DE}}(z)/\rho_{c,0}$
Parameterizations	$w_{\text{CDM}}$ $w_c : [-2.0, 0.0]$	Sigmoid $z_{\text{cut}} : [0.0, 3.0]$
	CPL $w_0 : [-2.0, 0.0], w_a : [-2.0, 2.0]$	
Binning/Nodal ( $i = 1 \dots 6, 20$ )	$w(z_i) : [-2.5, 1.0]$	$\rho(z_i) : [0.0, 1.5]$ if $z_i < 1.5$ : $[-1.5, 1.5]$ if $z_i \geq 1.5$
Binning-internal $z_i$	$w(z_i) _{i=4} : [-2.5, 1.0]$  $z_1 : [0.2, 1.4]$ $z_2 : [1.6, 2.8]$	$\rho(z_i) _{i=3} : [0.0, 1.5]$ if $z_i < 1.5$ : $[-1.5, 1.5]$ if $z_i \geq 1.5$  $z_1 : [0.2, 1.4]$ $z_2 : [1.6, 2.8]$

Table 4.1: Additional parameters and their flat prior range.

complete explanation see [20, 88, 32, 45, 44, 26] and references therein.

To compute the  $\chi^2$  for each data sample, we have

$$\chi_{\text{data}}^2 = (d_{i,m} - d_{i,\text{obs}})C_{ij,\text{data}}^{-1}(d_{j,m} - d_{j,\text{obs}}), \quad (4.8)$$

where  $d_m$  and  $d_{\text{obs}}$  are the model predictions and the observables respectively;  $C_{\text{data}}$  is the covariance matrix associated to each of the datasets. Since observations of each dataset are independent from each other, the joint  $\chi^2$  can be calculated as

$$\chi_{\text{total}}^2 = \chi_{\text{H}}^2 + \chi_{\text{SN}}^2 + \chi_{\text{BAO}}^2. \quad (4.9)$$

## Models and priors

Since the Bayesian evidence is very susceptible to the number of parameters and their prior distribution, it is worth to be careful when selecting them. A summary of the additional parameters along with their prior ranges is displayed in Table 4.1.

First, to provide a comparison to the reconstructions, some parameterization models will be constrained. For instance, the  $w_{\text{CDM}}$  model which corresponds to a constant EoS  $w_{\text{DE}}(z) = w_c$  and the Chevallier-Polarski-Linder (CPL) EoS [67] in which  $w_{\text{DE}}(z) = w_0 + w_a \frac{z}{1+z}$ , being  $w_0$ ,  $w_a$  and  $w_c$  free parameters to be estimated with data. The flat priors for  $w_0$  and  $w_c$  are the same  $[-2.0, 0.0]$  and the flat prior used for  $w_a$  is  $[-2.0, 2.0]$ . Then, inspired by the idea of a

density capable of performing a possible transition to  $\rho_{\text{DE}} \leq 0$  at high redshifts, similar to the one introduced by [10], a simple parameterization with the shape of a sigmoid function will be proposed:

$$\frac{\rho_{\text{DE}}(z)}{\rho_{c,0}} = \Omega_{\text{DE},0} \left( k_0 - \frac{1}{1 + e^{-10(z-z_{\text{cut}})}} \right), \quad (4.10)$$

with  $z_{\text{cut}}$  the redshift value where the transition may occur and  $k_0 = 1 + \frac{1}{1+e^{10z_{\text{cut}}}}$  is a constant which compensates the necessary amount so that  $\rho_{\text{DE}}(z=0)/\rho_{c,0} = 1 - \Omega_{\text{m},0}$ , to account for the Friedmann constraint. The parameter  $z_{\text{cut}}$  has a flat prior within the range  $[0.0, 3.0]$ . The sharp part of this sigmoid function comes from the argument in the exponential, if this number is larger (smaller) its transition to zero would be sharper (smoother).

Throughout all the reconstructions the data is let to decide the level of complexity of the two main functions within the range  $0 \leq z \leq 3$ , that is, the nodes and bins (free parameters) are placed over this range, and for  $z > 3$  there will be a constant value adopted, which corresponds to the last amplitude.

In the first set of reconstructions, the position of the nodes and bins are kept fixed and uniformly distributed within  $z = [0, 3]$ . In both types of reconstructions (bins and nodes) it is relatively free to choose any number of amplitudes, thus the number of parameters to be used are from 1 to 6 (and then, without loss of generality, jump to 20) to see the improvement of the fit to the data and how well the Bayesian evidence responded. Notice that the  $w$ CDM model is equivalent to the EoS reconstruction with one bin. In particular, the possibility of having a negative energy density is allowed, hence the amplitudes for the nodes and bins for  $\rho_{\text{DE}}(z)/\rho_{c,0}$  were set to move freely on the ordinate with flat priors  $[0.0, 1.5]$  if  $z < 1.5$ , otherwise the prior is set to  $[-1.5, 1.5]$ , since it is beyond  $z = 1.5$  where a switch to negative energy density is generally presented. For the amplitudes in the EoS we have flat priors of  $[-2.5, 0.0]$ . An important point is that when incorporating the correlation function method with a floating prior ( $\chi^2_{\text{prior}}$ ) or CPZ, it is recommended to choose a large number of bins. In this case, 20 bins were used and obtained consistent results.

For these previous set reconstructions the positions  $z_i$  for each parameter remained fixed, however one may argue that the location of the amplitudes could bias the results. To check this point, in the second set of reconstructions every amplitude varies as well as the internal positions are allowed to move freely, spanning over the  $z$ -direction (but without overlapping each other). For the reconstruction of  $w_{\text{DE}}(z)$  6 parameters will be considered: 4 varying amplitudes and 2 internal positions; similarly for  $\rho_{\text{DE}}(z)/\rho_{c,0}$  5 parameters will be used: 3 amplitudes and 2

internal positions. They will be referred to as 4y2x (3y2x in the case of the density) or simply *internal*  $z_i$ . Whereas the priors for the amplitudes remain the same as in the first set, the priors for the internal  $z_i$  positions are [0.2, 1.4] and [1.6, 2.8] respectively.

Regarding the regular cosmological background parameters, we have: the reduced dimensionless Hubble parameter  $h = H_0/100\text{kms}^{-1}\text{Mpc}^{-1}$  with a flat prior of [0.6, 0.8], the baryon density  $\Omega_{b,0}h^2$  with prior [0.021, 0.024] and the matter density parameter  $\Omega_{m,0}$  with a prior of [0.2, 0.4].

To perform the reconstruction analysis a modified version of the `SimpleMC` code was used [1] along with `dynesty` [219], a nested sampling algorithm which allows to compute efficiently the Bayesian evidence. For the number of live points one can follow the general rule [134] of using  $50 \times ndim$  live points, where the dimensionality  $ndim$  corresponds to the number of parameters, so the total number of live points depends on the reconstruction and the amount of bins/nodes. As for the stopping criterion an accuracy of 0.01 is set, which indicates the maximum difference between samples. Within the `SimpleMC` code I have also implemented the Principal Component Analysis and the correlation function method with the floating prior. For the functional posterior confidence contour plots a python package named `fgivenx` [125] was used.

## 4.4 Results

The results will be presented in 4 subsections: regarding the EoS, the energy density, the derived functions in terms of the results and the PCA analysis to distinguish noise from signal. The best-fit parameter values, the logarithm of the Bayes' factor ( $\ln B_{\Lambda\text{CDM},i}$ ) and the goodness of fit ( $\Delta\chi^2$ ) are presented in Table 4.2; complementary to this table, both quantities are displayed in Fig. 4.1. The regions of confidence for the parameterizations are shown in Fig. 4.2, whilst the reconstructions are shown in Figs. 4.3 and 4.4.

### Dark Energy Equation of State

The best-fit values (with standard deviations) for the  $w\text{CDM}$  and the CPL parameterization, correspond to  $w_c = -0.99 \pm 0.06$ ,  $w_0 = -1.01 \pm 0.08$  and  $w_a = 0.12 \pm 0.47$  respectively. That is, the models with one or two parameters,  $w\text{CDM}$ , CPL and the 2-parameter reconstructions produce very similar results, which means they are statistically consistent with the cosmological constant, within the 68% confidence region (see Figure 4.2 and the first column of Figure 4.3).

Model	Parameters	$h_0$	$\Omega_{m,0}$	$\ln B_{\Lambda\text{CDM},i}$	$\Delta\chi^2$
$\Lambda\text{CDM}$	-	0.683 (0.008)	0.306 (0.013)	0	0
$w\text{CDM}$	1	0.680 (0.017)	0.305 (0.015)	2.56 (0.14)	-0.14
Sigmoid	1	0.688 (0.009)	0.312 (0.013)	-0.12 (0.13)	-2.56
CPL	2	0.674 (0.021)	0.299 (0.019)	3.54 (0.15)	-0.68
<hr/>					
$w_{\text{DE}}(z)$	Binning				
	2	0.692 (0.017)	0.316 (0.015)	3.02 (0.16)	-0.83
	3	0.681 (0.018)	0.307 (0.016)	3.60 (0.15)	-2.88
	4	0.681 (0.017)	0.303 (0.015)	2.93 (0.16)	-5.15
	5	0.681 (0.017)	0.305 (0.016)	4.72 (0.16)	-3.57
	6	0.676 (0.016)	0.299 (0.015)	3.11 (0.17)	-8.86
4y2x	6	0.684 (0.017)	0.309 (0.015)	2.86 (0.16)	-8.03
	20	0.691 (0.015)	0.298 (0.014)	2.33 (0.18)	-15.74
$+\chi_{\text{prior}}^2$	20	0.688 (0.015)	0.298 (0.015)	5.52 (0.18)	-9.97
<hr/>					
	Linear-Nodal				
	2	0.681 (0.021)	0.307 (0.019)	3.96 (0.15)	-0.12
	3	0.677 (0.018)	0.301 (0.018)	3.61 (0.16)	-2.98
	4	0.682 (0.018)	0.302 (0.017)	3.46 (0.16)	-3.74
	5	0.683 (0.017)	0.305 (0.016)	5.03 (0.16)	-3.19
	6	0.681 (0.017)	0.302 (0.016)	4.15 (0.17)	-5.06
4y2x	6	0.681 (0.017)	0.302 (0.016)	3.02 (0.16)	-6.22
<hr/>					
$\rho_{\text{DE}}(z)/\rho_{c,0}$	Binning				
	1	0.694 (0.013)	0.318 (0.015)	-0.01 (0.13)	-0.77
	2	0.683 (0.013)	0.309 (0.015)	-0.42 (0.13)	-3.04
	3	0.681 (0.013)	0.307 (0.015)	-0.59 (0.14)	-4.24
	4	0.677 (0.014)	0.304 (0.016)	0.53 (0.14)	-3.61
	5	0.682 (0.015)	0.309 (0.016)	0.54 (0.14)	-5.72
	6	0.683 (0.015)	0.311 (0.016)	1.23 (0.15)	-8.04
3y2x	5	0.686 (0.012)	0.313 (0.014)	-0.49 (0.14)	-4.47
	20	0.685 (0.014)	0.318 (0.014)	2.36 (0.16)	-11.60
$+\chi_{\text{prior}}^2$	20	0.685 (0.015)	0.317 (0.014)	5.20 (0.16)	-9.96
<hr/>					
	Linear-Nodal				
	2	0.683 (0.017)	0.311 (0.015)	0.57 (0.14)	-2.72
	3	0.685 (0.019)	0.311 (0.017)	1.58 (0.14)	-2.47
	4	0.686 (0.018)	0.313 (0.016)	1.50 (0.14)	-2.73
	5	0.691 (0.017)	0.314 (0.016)	1.65 (0.15)	-3.71
	6	0.685 (0.017)	0.308 (0.015)	1.85 (0.15)	-4.13
3y2x	5	0.691 (0.016)	0.315 (0.015)	1.11 (0.14)	-3.38

Table 4.2: Mean values, and standard deviations, for the cosmological parameters. For each model, the last two columns present the Bayes Factor, and the  $\Delta\chi^2 = \chi_{\Lambda\text{CDM}}^2 - \chi_i^2$  for fitness comparison. The datasets used are BAO+H+SN. Here  $\ln E_{\Lambda\text{CDM}} = -530.79(0.12)$ .

Also, these results can be validated when comparing the  $\Delta\chi^2$  presented in Table 4.2

When computing the Bayes' factors of all the models (green region of the top panel in Fig. 4.1) one observes, in general, a moderate evidence against the reconstructions regardless of the number of extra parameters, compared to the standard model. However, in the reconstructions certain features at high redshift become apparent as more parameters are added, and therefore an enhancement in the goodness of fit. For instance, when using three amplitudes (second column of Figure 4.3), a bump-like shape appears at  $z \approx 1.5$  and after that the general form presents a possible crossing of the phantom-divide-line (PDL), i.e. for  $z \gtrsim 2$  the amplitude values lean toward  $w_{\text{DE}} < -1$  outside the 68% confidence region, which represents an improvement of  $\Delta\chi^2 \sim -3$ . If one continues the process of adding amplitudes to the reconstructions, the main trend preserves a bump but now located at about  $z \approx 1.2$  and a crossing of the PDL at  $z \sim 1.5$ . This is not true though when having 5 extra parameters (and there will be a similar problem when reconstructing the density with 4 extra parameters), although the reason for this is mainly related to the reconstruction methodology, for a detailed explanation please refer to 4.5. It was also found that the cosmological constant is slightly outside of the 95% confidence contours at several places (see last column of Figure 4.3), and according to the Table 4.2 by using the definition of statistical significance in terms of the standard deviation  $\sigma$ , that is, the signal-to-noise ratio  $S/N \equiv \sqrt{|\Delta\chi^2|}$ , it represents a  $\sim 3\sigma$  deviation from  $\Lambda\text{CDM}$  based on the improvement in the fit alone. These two features play a key role in identifying the correct dark energy model. If future surveys confirm their existence, the cosmological constant and single scalar field theories (with minimal assumptions) might be in serious problems as they cannot reproduce these essential features, and therefore alternative models should be taken into account. Furthermore, in the internal- $z_i$  reconstructions the internal positions are able to localize the position for the bump and the PDL, and the results resemble the previous ones, see the last two columns of Figure 4.4. Besides the presence of the bump and crossing of the PDL, we can note that at  $z = 0$  the 68% confidence contour lays down right below the limits of  $w_{\text{DE}} < -1$ . An important point to stress out is that the freedom of the internal positions led to a better fit to the data, compared to the reconstructions with the same number of parameters but fixed positions; displayed as the x-markers in the top panel of Figure 4.1.

Finally, to corroborate these findings, two reconstructions with 20 parameters are included: binning and binning with CPZ correlation function, shown in the column 1 and 2 of Figure 4.4. For these particular reconstructions, the focus is on the binning method as it provides a better fit to the data. As commented above, the correlation method is incorporated to create a function

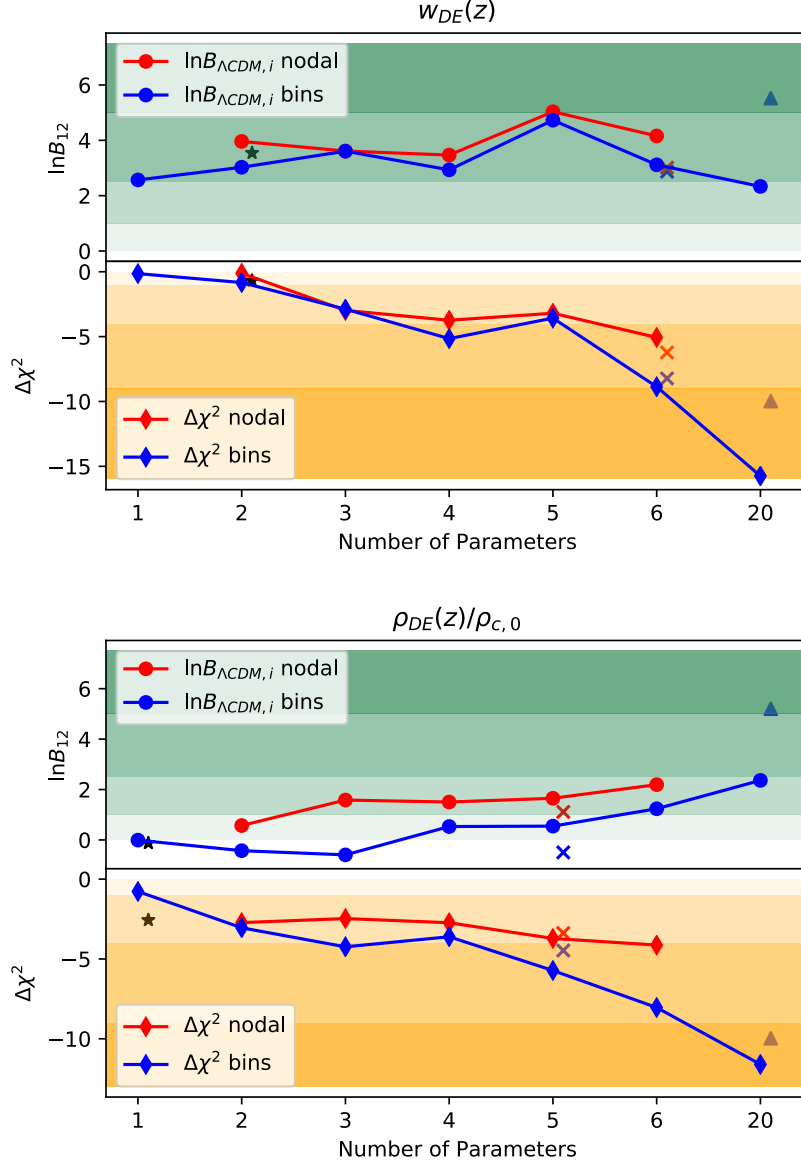


Figure 4.1: In this graph the differences in the  $\Delta\chi^2$  and the Bayes factor between  $\Lambda$ CDM and the reconstructions for  $w_{DE}(z)$  and  $\rho_{DE}/\rho_{c,0}$  are shown. The green shades show the strength-of-evidence according to the Jeffrey's scale and the orange shades show the 1 to 4- $\sigma$  levels of statistical significance  $S/N \equiv \sqrt{|\Delta\chi^2|}$ . Ideally one wants the upper markers to stay as close as possible to the black line at 0 (preferably to cross it), which it is an indication of a better Bayes' factor, and the lower ones to be far away from zero, which indicates a better fit to the data. The stars indicate the fitness of the reconstruction of the CPL EoS (top) and the energy density with a sigmoid (bottom), the crosses indicate the internal  $z_i$  reconstructions and the triangles the reconstructions with 20 bins plus correlation function. The binning reconstructions are plotted with blue lines, whereas the nodal with red lines.



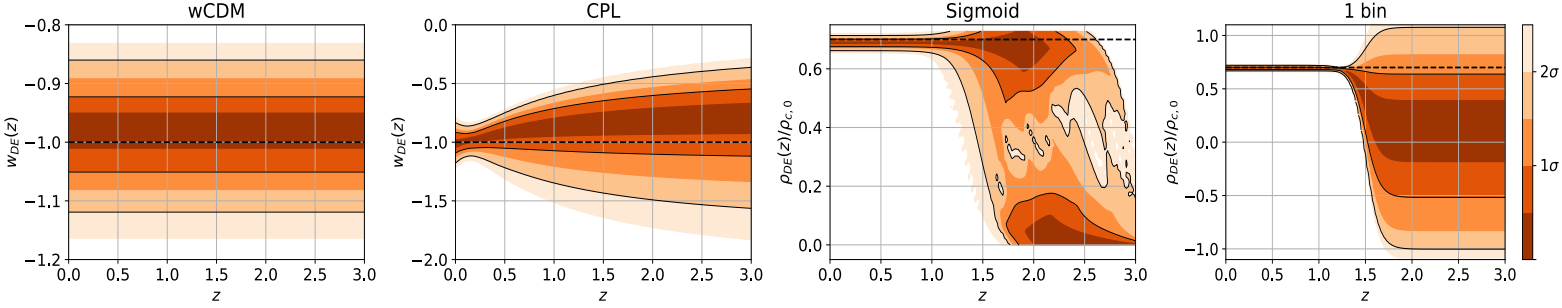


Figure 4.2: These plots show the functional posterior probability: the probability of  $w_{\text{DE}}(z)$  or  $\rho_{\text{DE}}(z)/\rho_{c,0}$  as normalised in each slice of constant  $z$ , with colour scale in confidence interval values. The 68% ( $1\sigma$ ) and 95% ( $2\sigma$ ) confidence intervals are plotted as black lines. From left to right: parameterized equations of state for  $w\text{CDM}$  and CPL, phenomenological sigmoid and 1-bin energy density reconstructions. The dashed black line corresponds to the standard  $\Lambda\text{CDM}$  values.

that evolves smoothly, and in general, they both share the same structure: a bump located at  $z \approx 1.2$ , a crossing of the PDL at  $z \approx 1.5$  and a slight preference of  $w_{\text{DE}} < -1$  at  $z = 0$ . Besides these three features (found already in the internal models), there is also an oscillatory behaviour throughout the whole structure, which yields to a deviation of about  $4\sigma$  to the  $\Lambda\text{CDM}$ . Even though this result may be considered as an overfitting due to the large number of parameters and small  $\Delta\chi^2$ , its Bayes factor is as good as the reconstruction with fewer amplitudes. Also, the authors in [226] obtained a similar shape by using only three parameters in a Fourier basis and concluded a deviation of about  $3\sigma$  from the cosmological constant, as done here through a different mechanism.

## Dark Energy Density

Similarly to the previous section, with one extra parameter, through the  $z_{\text{cut}}$  in the sigmoid function for  $\rho_{\text{DE}}$ , one gets a better fit to the data by more than  $1\sigma$ , and its Bayes' factor results on a negative value  $B_{\Lambda\text{CDM},i} = -0.124 \pm 0.131$ , indicating a slight evidence in its favor, although it is still within the  $1\sigma$  for the error. The constraints of the  $z_{\text{cut}}$  parameter corresponds to  $2.101 \pm 0.413$ , which provides an insight of a possible vanishing energy density beyond  $z = 2$ . This feature is also noticeable when looking at the 1-bin reconstruction where the cosmological constant is on the edge of the 68% confidence contour for  $z > 1.5$  (see Fig. 4.2).

By incorporating additional parameters to the reconstruction of  $\rho_{\text{DE}}(z)/\rho_{c,0}$  the fit to the data becomes better than the standard model, as shown by the negative values of the  $\Delta\chi^2$  on the bottom panel of Fig 4.1. Even though this behaviour is expected by the increased of complexity,

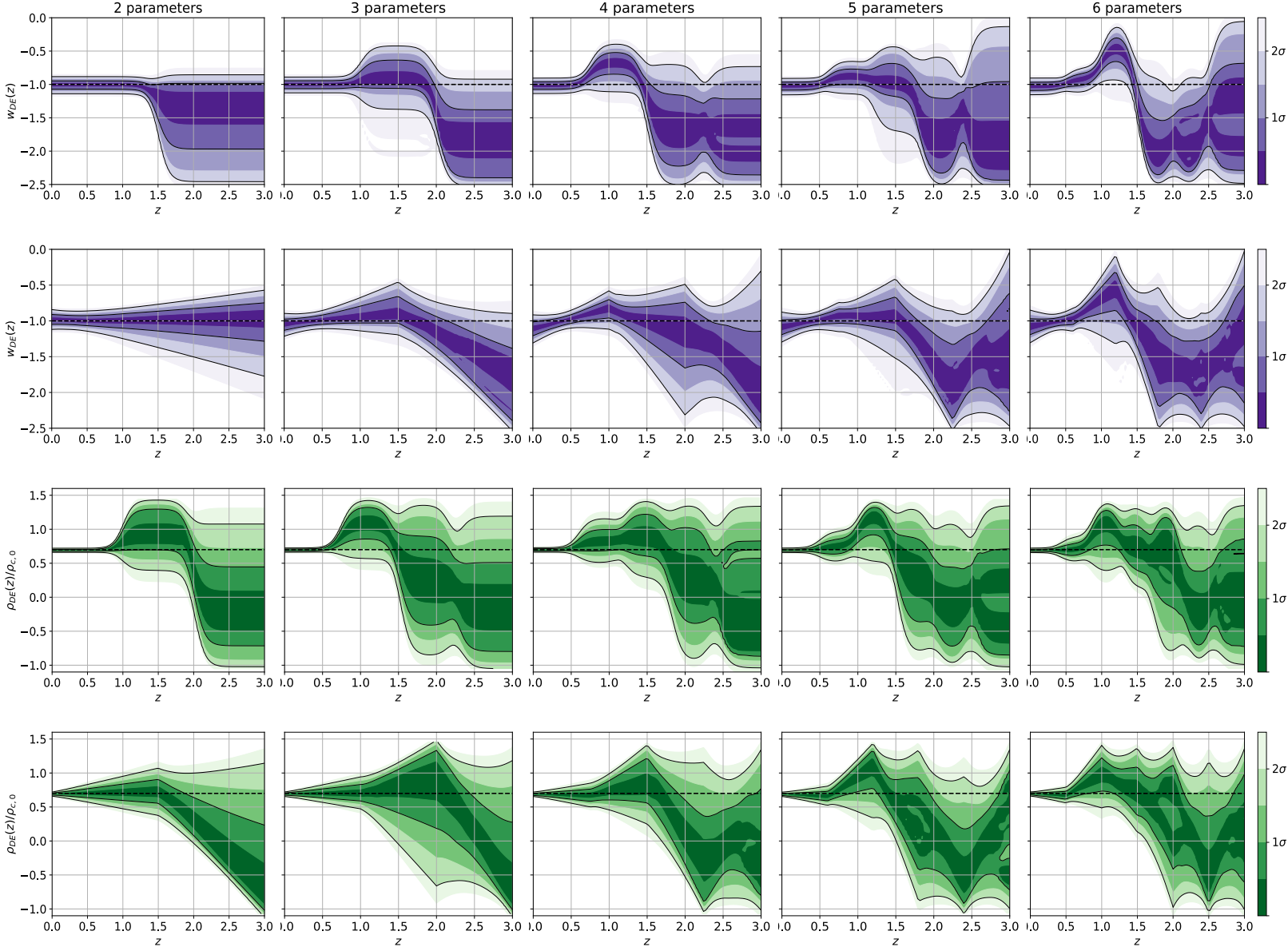


Figure 4.3: From top to bottom: reconstructed  $w_{DE}(z)$  with bins (and nodes), reconstructed  $\rho_{DE}(z)/\rho_{c,0}$  with bins (and nodes). It is easy to observe there is more structure (more apparent features) in the reconstructions as the number of parameters increases (from left to right).

it is accompanied by a penalization incorporated into the Bayes Factor, shown in the green part of Fig 4.1. As the number of nodes/bins increases it is expected that the values of  $B_{\Lambda\text{CDM},i}$  do so too, however, an important point to note is the existence of a valley on this factor up to 4 parameters, where the first three have negative values indicating an evidence in favor (but still

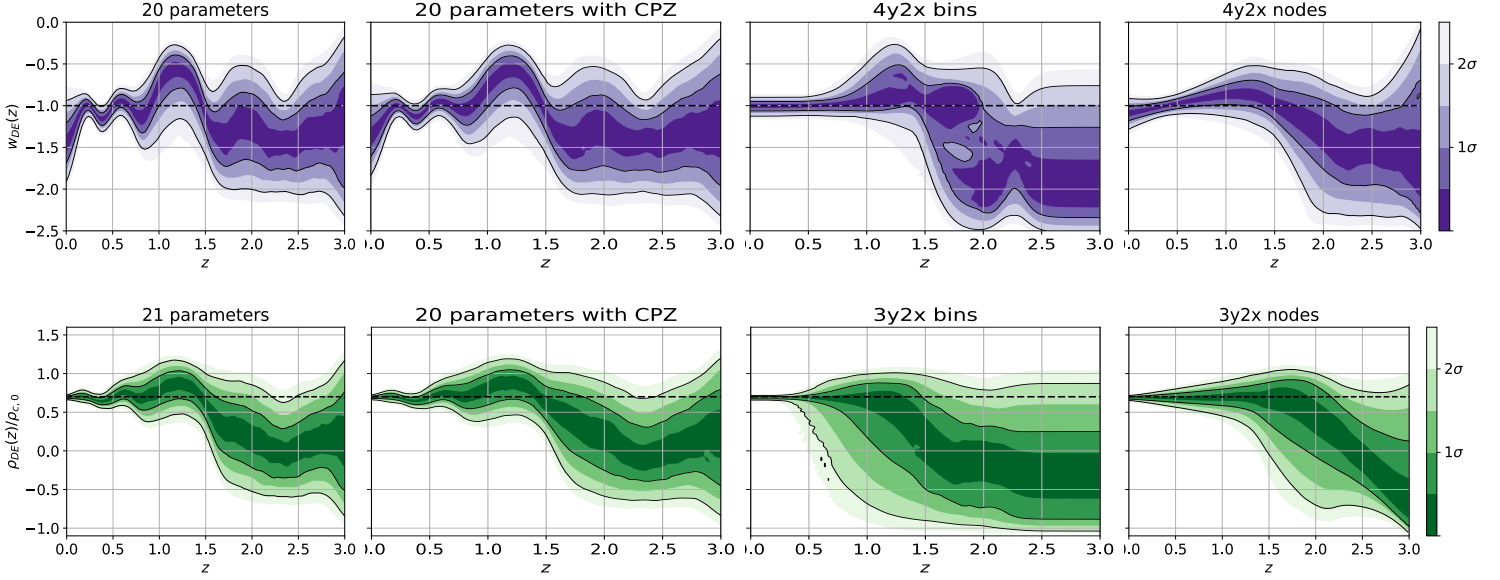


Figure 4.4: From left to right: reconstructions with 20 bins, 20 bins with correlation function, internal  $z_i$ -bins and internal  $z_i$ -nodes. Purple figures correspond to the EoS whereas green to the energy density.

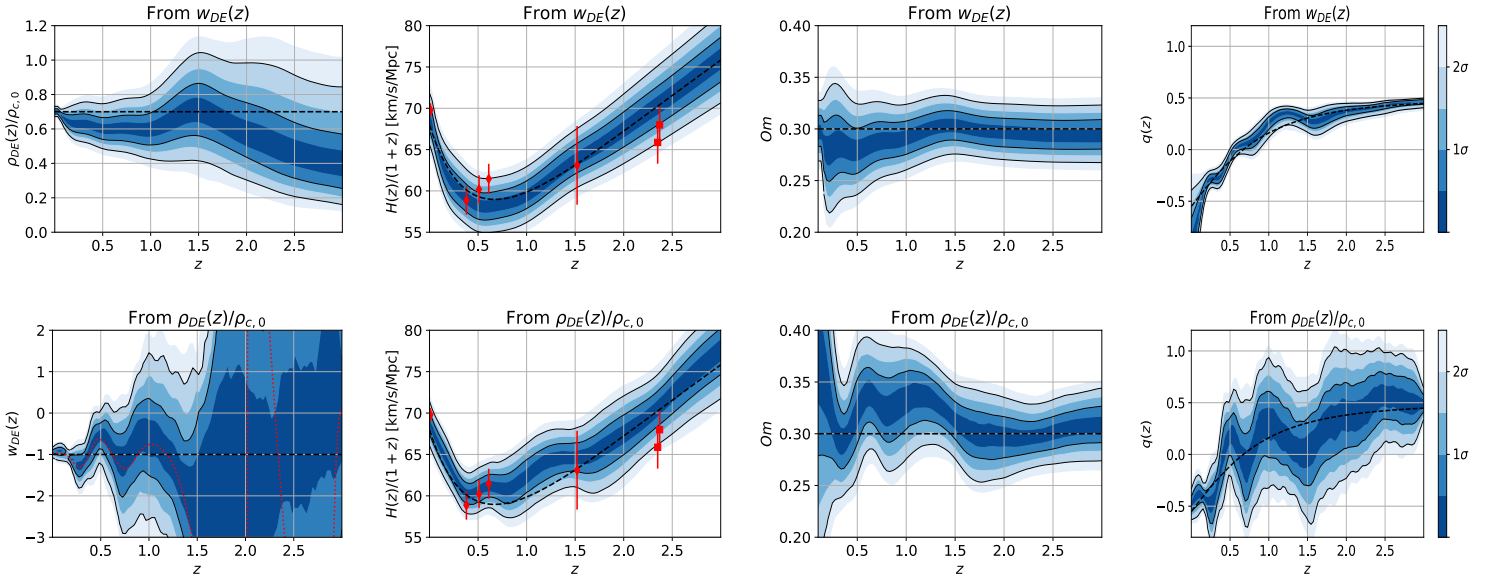


Figure 4.5: Derived functions for the reconstructed  $w_{DE}(z)$  and  $\rho_{DE}(z)/\rho_{c,0}$  with 20 bins plus correlation function. The red dotted line in the derived  $w_{DE}(z)$  corresponds to the best-fit values.

inconclusive) of the reconstructions, and also reflected on the improvement of the  $\chi^2$ . This may be happening due to the data having a preference for an energy density with a bump located

at  $z \approx 1.2$  and then as the redshift becomes larger  $\rho_{\text{DE}}(z)$  decreases until reaching a zero value, and even passing through negative values, but still statistically consistent with zero. That is, by having at least two amplitudes the reconstruction methodology is flexible enough to present this behavior, as seen in the first three columns of Fig 4.3. As more parameters are added, the presence of a possible sign change in the energy density is more pronounced. This transition occurs near  $z \approx 2$ , and in the region around  $z \approx 2.5$  the deviation from the cosmological constant peaks. The general behaviour of these reconstructions is reflected by these two main features, which together provide a deviation up to  $2.8\sigma$  from the standard model.

In the same manner as the reconstruction for the EoS, one may say that the position of these two features (the bump at  $z \sim 1.2$  and the vanishing energy density behaviour for  $z > 1.5$ ) could be biased because the particular location for the amplitudes. Even so, it is stated in [12] that these particular features and their positions are prompted by the Lyman- $\alpha$  BAO data (as will be further discussed in the PCA subsection). In order to find an optimal place for the internal positions, they are set free by allowing them to move around the  $z$ -axis. Because of this additional freedom, the internal reconstruction (or 3y2x model) is able to localize these features and provides a better fit to the data, compared to the reconstruction with three fixed amplitudes. Moreover, despite having 5 extra parameters, the binning reconstruction has a negative Bayes factor which favours this model over the rest of the reconstructions (displayed as crosses in the bottom panel of Fig. 4.1).

Lastly, as was made with the EoS, a 20 bins and 20 bins with the correlation function reconstructions were incorporated. Both present more substructures like an oscillatory-like behavior at late times and also have a transition to a null or negative density in  $z > 2$ , as seen in Fig 4.4. Analogous to the guidance offered by the oscillatory demeanor found in the EoS reconstruction, its apparent wavering nature in  $z < 1.5$  could encourage the study of an oscillatory basis such as a Fourier series. Looking at the  $\Delta\chi^2$  we notice a deviation from the  $\Lambda$ CDM of about  $3.4\sigma$ , and a Bayes factor comparable with the few-parameter reconstructions.

The drop-off behaviour of  $\rho_{\text{DE}}(z)$  and, perhaps, a transition to a negative energy density has been captured in other works [162, 155, 243, 235, 10, 12, 97], as it seems to alleviate the tension that arises by estimating the Hubble constant  $H_0$  with different datasets. It was also found in [72] that, when considering flat  $\Lambda$ CDM and binning the data, negative energy densities ( $\Omega_{m,0} > 1$ ) are expected for higher redshifts. Hence, it may be pertinent to study models with a similar demeanor. This behaviour does not necessarily imply a negative physical energy density per se, but it may be the indication of an effective energy density, i.e. similar to the one generated by the curvature component [126, 3].

In general, and throughout the reconstruction process, there have been found different features beyond the cosmological constant, which result in deviations up to  $3\sigma$ . One final interesting observation is that the reconstructions when using bins are generally better than with nodes and also the Bayes factor shows an improvement. Likewise, there is a preference for the reconstruction with 20 bins over 20 bins plus the correlation function, reflected on the  $\Delta\chi^2$ , in fact there is a strong evidence against using the 20 bins+prior model, according to the Jeffreys' scale.

## Derived functions

Once the general form of both the EoS and the energy density are obtained one proceeds to obtain their respective derived functions, these being: the Hubble parameter  $H(z)/(1+z)$ , the  $Om$  diagnostic and the deceleration parameter  $q(z)$ . For the reconstructed energy density, the EoS can be derived and similarly for the reconstructed EoS, the energy density is inferred. These derived functions correspond to the 20 bin reconstruction, which produced the best fit, and their posterior probabilities are displayed in Fig. 4.5. In general, the functions coming from the energy density show an enhanced oscillatory behaviour, compared to the functions derived from the EoS.

When comparing the reconstructed EoS with the one deduced from  $\rho_{\text{DE}}/\rho_{c,0}$  we notice an important difference: negative energy density values are allowed, hereby the derived EoS presents a discontinuity at about  $z \approx 2$ , seen in the best-fit model denoted by the red dotted line in Fig. 4.5. Such type of discontinuities have been found and studied in other reconstructions and different models, such as [10, 116, 240]. Regarding the derived energy density: when reconstructing  $\rho_{\text{DE}}/\rho_{c,0}$  directly its freedom in the parameter space allowed it to reach null values of the energy density, and even negative ones at high redshifts; but when a barotropic EoS is imposed, through the conservation equation, the derived energy density remains always positive with a bump located at  $z \approx 1.5$  and a smooth drop out at high redshifts.

Considering the  $H(z)/(1+z)$ , the best-fit reconstructed function passes through the observational  $H(z)$  values (red error bars in Fig. 4.5),  $H_0 = 69.8 \pm 0.8 \text{ km s}^{-1} \text{ Mpc}^{-1}$  from the TRGB [109], consensus Galaxy BAO (from  $z_{\text{eff}} = 0.38, 0.51, 0.61$ ) and DR14 Ly- $\alpha$  BAO (from  $z_{\text{eff}} = 2.34, 2.35$ ) [45, 88, 26], and hence the best-fit is slightly better compared to the  $\Lambda$ CDM model (black dashed line).

In general, the  $Om$  diagnostic shows consistency with several parameterizations and reconstructions [194, 163]. Nevertheless, in these reconstructions a mixed behaviour between

quintessence and phantom components has been found, corroborated by the EoS. That is, we have certain places where  $Om(z) > \Omega_{m,0}$  (quintessence) and others with  $Om(z) < \Omega_{m,0}$  (phantom).

Finally, the deceleration parameter  $q(z)$  for the reconstructed EoS gives a value for the transition to an accelerated universe around  $z \sim 0.6$ , which is statistically consistent with the  $\Lambda$ CDM value, and with results previously obtained [154, 42, 163]. On the other hand, when  $q(z)$  is reconstructed through the energy density, the universe can potentially go through several short periods of acceleration-deceleration (a similar behaviour was seen in [243]), however the main acceleration transition corresponds to  $z \sim 0.45$ , unlike in  $\Lambda$ CDM, where the acceleration starts at  $z \sim 0.7$ .

## PCA and the Bayes' Factor

By applying the principal component analysis to remove the noisiest modes (enough to preserve 95% of the variance) of the reconstructions, we see that the biggest changes happened mainly at  $z > 2.0$ . An example of this can be seen in Fig. 4.6, where the reconstruction with 20 bins for the energy density and the EoS was used. Since the only information here is coming from the Lyman- $\alpha$  BAO ( $z \sim 2.3$ ) it may be reasonable to argue that some tensions amongst models come from these high-redshift data (as has been also suggested in [6, 104, 80]), or perhaps it exists the possibility that large systematic errors are present in this dataset. This may be an indication that the dynamical DE behavior, referring to the crossing of the PDL for the EoS and the null energy density at early times, is merely due to noisy data, although this will not be confirmed until a significant amount of information is obtained in this redshift region. This also has an effect in the Bayesian Evidence. As the parameters beyond  $z = 1.5$  are the least constrained they contribute little to nothing to the final evidence of the reconstruction and thus means that one has to be very careful when utilizing the Bayes' Factor to directly perform model selection. Added to this is the fact that the Evidence is pretty susceptible to the prior range. Such problems are common when performing reconstructions, but a possible solution has been proposed in [138], although it is still a work in progress.

Nevertheless, something that should be borne in mind is that certain characteristics pointing out to dynamics are still present even when removing the noisiest PCs. These characteristics, in the energy density, are the oscillatory nature at low redshift and the transition to a null or negative energy density in  $z \approx 1.5$ ; with the EoS the preserved features include the oscillatory behavior, the bump in  $z \approx 1.3$ , a preference for values below  $w_{DE} = -1$  at  $z = 0$ , and the crossing

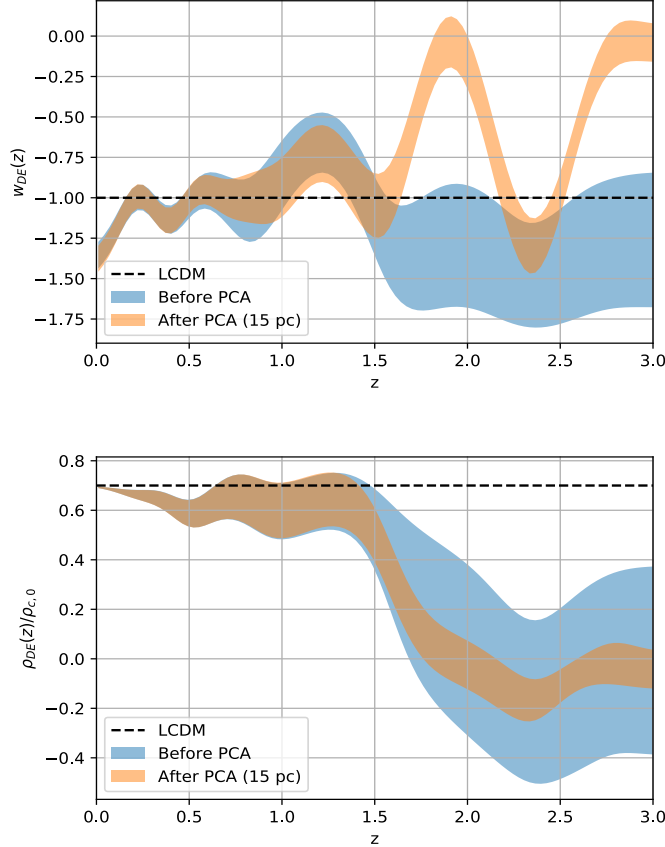


Figure 4.6: Applying the principal component technique to the reconstructions of the EoS and the energy density with 20 bins. By eliminating 5 PCs (which add up to about 5% of the total variance for each reconstruction) one obtains the orange figures with slightly overestimated errors localized in  $z > 1.5$ .

of the phantom divide line in late times.

## 4.5 Capturing features with the right amount of parameters

Given the mathematical structure of the binning scheme and linear interpolation of the reconstructions there are some subtleties that are not obvious at first glance. In particular one that has an effect to this work: a bigger number of parameters does not necessarily means a better fitness to the data. We can only guarantee it to be true when the bigger number of parameters is a multiple of the one being compared. For example if we compare a reconstruction with 2 parameters we can only guarantee that the ones with  $2n$  (with  $n \in \mathbb{N}$ ) parameters will perform better at fitting the data (and this is true for any number of parameters, not only 2). This is

because the bins/nodes are all equally spaced in the redshift range  $[0, 3]$ . When using, let's say 2 and 4 parameters, the reconstruction with 2 having parameter positions of  $(1.5, 3.0)$  is a special case of the one with 4 with parameters positions of  $(0.75, 1.5, 2.25, 3.0)$ , and the same is true for any multiple of 2.

This also means that there may be some features that a certain number of bins/nodes will not be able to capture since they are located in a region not accessible by the larger number of bins/nodes. As seen in Fig 4.7 where the data (black dots) are being modeled with 2 and 3 bins. The data clearly show a transition in  $z = 1.5$  and the 3 bins cannot, by design, correctly model this transition since the positions of the bins interfere. It is also important to note that these problems also appear with an interpolation reconstruction (linear, cubic and so forth), not only in the binning scheme. This happens almost exclusively to reconstructions with a low number of nodes/bins because as more parameters are utilized the resolution of the reconstruction becomes a lot better.

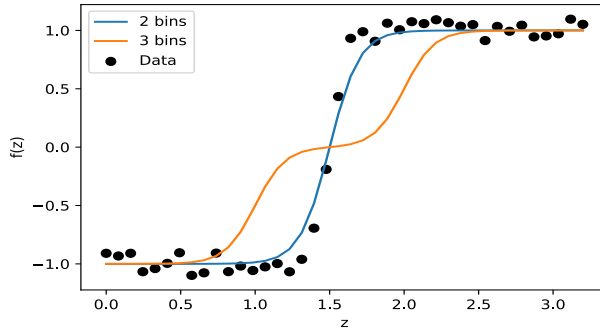


Figure 4.7: Visual representation of the possibility of underfitting data with more parameters.

Even if these effects could seem generally unimportant they are quite relevant to this work since they are both present. When reconstructing either the EoS or the density with 4 and 5 parameters we should expect a better fit to the data with 5 parameters because it has more degrees of freedom, but the  $\Delta\chi^2$  says otherwise. By separating and analyzing the  $\Delta\chi^2$  in its components via equation 4.9 we see some differences as expected, but the component responsible for the bad fitness when utilizing 5 bins is the  $\Delta\chi_H^2$  with a difference of 3.36 when compared to the 4 bin reconstruction (for reference we also have  $\Delta\chi_{SN}^2 = -1.38$  and  $\Delta\chi_{BAO}^2 = -0.4$  in favor of the 5 bin reconstruction). This indicates that there might be some feature present in the 4 bin reconstruction which favours it specifically with the Hubble parameter data, and it is not present in the 5 bin one. This feature is also present in the 6 bin reconstruction, as represented



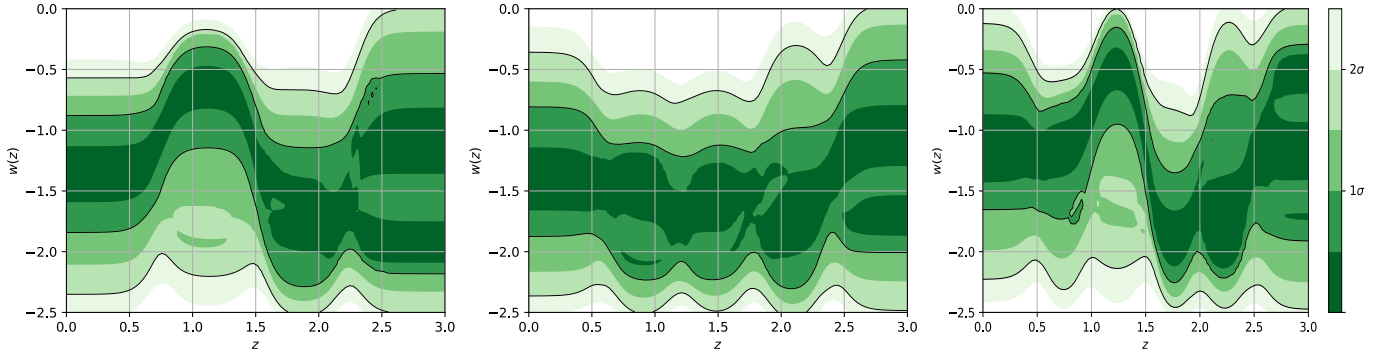


Figure 4.8: Functional posteriors of the EoS reconstruction, from up to down, with 4, 5 and 6 bins using only Hubble parameter data.

by its  $\Delta\chi_H^2 = 5.26$  (when compared with the 5 bin one).

The absent feature becomes obvious when reconstructing the EoS with 4, 5 and 6 bins with only Hubble parameter data, which is the data where 5 bins has trouble with. The functional posterior of these reconstructions can be seen in Fig 4.8. Paying attention to the  $1\sigma$  region of 4 and 6 bins a bump can be seen followed by a slump in the interval  $0.7 < z < 2.0$ . The 5 bin reconstruction is completely missing this bump and subsequent slump. As explained at the start of the section, the reason for the inability with 5 bins to reproduce this behaviour comes from its bins' positions. The important bin is the one that starts in 1.2 and ends in 1.8, since the transition from bump to slump happens in  $z = 1.5$  it is impossible for this bin to correctly capture such trait.



## Chapter 5

# Interacting Dark Energy in a Model Independent way

### 5.1 Introduction

In order to explain the small scale structure formation, or at least to ameliorate the problems associated with the CDM model, several alternatives have been introduced. One viable option is to replace the standard CDM with a Scalar Field dark matter components [216, 123, 147, 156, 227, 168] or by introducing the Self Interacting dark matter [220, 120, 183], or to support the warm dark matter scenario [186, 167].

On the other hand, there exists a particular type of models where the non-minimal interaction (hereinafter I'll use the word interaction to mean non-minimal interaction) between DM and DE may be able to solve or at least alleviate these issues (along with the DE ones) with relative ease [145, 146, 92, 193, 25, 59, 89, 250, 253, 187, 93, 94, 117, 150, 43, 176, 175]. Recent analyses have focused on the resemblance between DM-DE interacting models with modified gravity theories [238, 142]. As such, a viable alternative is to assume an interaction between these two components [54, 48]. Even though the interacting models have been extensively analyzed, their interaction kernel's form still remains a mystery.

This is why a significant amount of research works have been dedicated to introducing new models in a phenomenological way (such as the parameterizations). Models with interacting dark sectors, also named Interacting Dark Energy (IDE), are no strangers to parameterizations, since the interplay is generally proposed in a particular demeanor motivated by certain characteristics.

For example, a popular assumption, inspired by several behaviors in particle physics [185], is to express the interaction kernel,  $Q$ , in terms of the energy densities ( $\rho_{\text{DM}}$  and/or  $\rho_{\text{DE}}$ ) and time (through the Hubble parameter  $H^{-1}(z)$ ). Nevertheless, these are only few assumptions and, since the nature of the interaction is still obscure, they can come up in several different functional forms and combinations, see for example [146, 92, 238, 250, 187, 252]. Generally, for these type of models, it is found that the structure formation remains unaltered and late-time acceleration is also in accordance with the standard model (see [238, 48] for a comprehensive review of interacting models and their behavior).

However, as useful as parameterizations may be (not only for IDE but in general) they possess the already mentioned limitation that a functional form is assumed a priori, which could bias the results.

To avoid these issues it is useful to perform reconstructions by extracting information directly from the data, using model-independent techniques or non-parametric ones. The Gaussian process (GP), specifically for the IDE models, has become a regular choice for a non-parametric approach [23, 165, 248, 50, 49, 236]. This methodology has found a possibility of an interaction and given some insights into possible preferred behaviors and characteristics, such as a crossing of the non-interacting line. In spite of this, the GP approach cannot be used for model comparison in concordance with the  $\Lambda$ CDM model given its non-parametric nature.

Despite the extensive study of both the interaction models and the model-independent approaches in cosmology, they have been rarely used in tandem; for example Cai et. al. [58] and Salvatelli et. al. [209] used redshift bins, and for Solano et. al. [218] the main focus are the Chebyshev polynomials. They found a possible crossing in the non interaction line, and in [58] obtained an oscillatory behavior through the interaction, although the data in this work was limited to cover a narrow range of redshift (around  $z < 1.8$ ). This finding inspired the study of possible sign-switching interactions, instead of the classical monotonically decreasing or increasing parameterizations. We have for example: in [149] the parameterization  $Q(a) = 3b(a)H_0\rho_0$  was first proposed, with  $b(a) = b_0a + b_e(1 - a)$  being the sign-switching part; in [224] the model  $Q = 3H\sigma(\rho_{\text{DE}} - \alpha\rho_{\text{DM}})$  ( $\alpha$  being a positive constant of order unity) also presents a switching interaction; in [258] the named Ghost dark energy is used in tandem with an interaction kernel  $Q = 3\beta Hq(\rho_{\text{DE}} + \rho_{\text{DM}})$  where its sign is able to change since it is a function of the deceleration parameter  $q$ ; and in [121] a bunch of variations of  $Q(a) = 3b(a)H(a)\rho_i$  are studied. The general consensus reached by the majority of these models is that, if a transition was to happen, it should be around the time when the accelerated expansion of the universe began ( $z \sim 0.5$ ). Therefore, in this chapter I will use some model-independent approaches to reconstruct the in-

interaction kernel between DE and DM directly from the data. The methods used are the binning scheme along with the Gaussian Process as an interpolation approach. Moreover, as additional cases, together with the DM-DE interaction, the cosmological constant will be replaced with a constant EoS free to vary.

The chapter is organized as follows: in [5.2](#) a brief review of the underlying theoretical reason that can lead one to consider the possibility of non-minimal interaction within the dark sector is provided, followed by [5.3](#) where the reconstruction methodologies are described. In [5.4](#) the datasets and some specifications about the parameter estimation and model selection are made clear. Finally, in [5.5](#) the main results are presented.

## 5.2 Interacting DM-DE Model

Let's recall the Friedmann and continuity equations, respectively:

$$3H^2 = \kappa(\rho_r + \rho_b + \rho_{\text{DM}} + \rho_{\text{DE}}), \quad (5.1)$$

$$\begin{aligned} \dot{\rho}_r + 4H\rho_r + \dot{\rho}_b + 3H\rho_b + \dot{\rho}_{\text{DM}} + 3H\rho_{\text{DM}} \\ + \dot{\rho}_{\text{DE}} + 3H\rho_{\text{DE}}(1 + w_{\text{DE}}) = 0, \end{aligned} \quad (5.2)$$

where  $H$  is the Hubble parameter, and a dot denotes derivative with respect to cosmic time. It is reasonable to assume that the sources such as baryons and radiation, whose physics are well known within the standard model of particle physics, are individually conserved, i.e.,  $\nabla^\mu T_{\mu\nu}^r = 0$  and  $\nabla^\mu T_{\mu\nu}^b = 0$  (viz.,  $\dot{\rho}_r + 4H\rho_r = 0$  and  $\dot{\rho}_b + 3H\rho_b = 0$ ). This in turn implies, via continuity equation [5.2](#) conservation within the dark sector (DM+DE) itself:

$$\dot{\rho}_{\text{DM}} + 3H\rho_{\text{DM}} + \dot{\rho}_{\text{DE}} + 3H\rho_{\text{DE}}(1 + w_{\text{DE}}) = 0. \quad (5.3)$$

At this stage, in the cosmology literature so far, the very strong assumption that DM and DE are conserved separately—i.e.,  $\dot{\rho}_{\text{DM}} + 3H\rho_{\text{DM}} = 0$  and  $\dot{\rho}_{\text{DE}} + 3H\rho_{\text{DE}}(1 + w_{\text{DE}}) = 0$ —is often made with almost no basis of this assumption. Then, taking advantage of the only remained freedom, viz.,  $w_{\text{DE}}$ , due to the unknown nature of DE, different models of DE have been put forward to extend the standard cosmological model since the discovery of the late time acceleration of the universe. Thus, if we do not follow this two-step path to build a cosmological model, the fact that the very nature of both DM and DE are still not known and GR itself does not impose them to be conserved separately, we have, from [5.3](#),  $\nabla^\mu T_{\mu\nu}^{\text{DM}} = Q$  and  $\nabla^\mu T_{\mu\nu}^{\text{DE}} = -Q$ , namely,

$$\dot{\rho}_{\text{DM}} + 3H\rho_{\text{DM}} = Q, \quad (5.4)$$

$$\dot{\rho}_{\text{DE}} + 3H\rho_{\text{DE}}(1 + w_{\text{DE}}) = -Q, \quad (5.5)$$

where we have two undetermined functions; the DE EoS parameter  $w_{\text{DE}}$  and the interaction kernel  $Q$ , which determines the rate and direction of the possible energy transfer between DE and DM; namely,  $Q = 0$  implies minimal interaction (gravitational interaction only) between DM and DE,  $Q > 0$  implies energy transfer from DE to DM, and  $Q < 0$  implies energy transfer from DM to DE. In particular, in the case  $Q = 0$  (minimal interaction) and  $w_{\text{DE}} = -1$  we have the standard  $\Lambda$ CDM model. In this chapter, there will not be any assumption about any phenomenological or theoretical models for the nature of interaction between DM and DE ( $Q$ ) and the dynamics of the DE ( $w_{\text{DE}}$ , or a corresponding  $\rho_{\text{DE}}$ ), instead these parameters will be reconstructed, as well as some important kinematic parameters (the Hubble parameter  $H(z)$  and deceleration parameter  $q(z) \equiv -1 + dH^{-1}/dt$ ), from observational data in a model-independent manner. The effects of a possible non-minimal interaction between DM and DE will be reflected on altered kinematics of the universe. This can be observed via the Friedmann equation (5.2), due to the deviations in the evolution of the energy densities of the DM and DE from what they would have in the absence of a non-minimal interaction. It is in general very useful to have an idea on what corresponding minimally interacting (no energy exchange) DE and DM would lead to the same altered kinematics of the universe. To do so, one can define the *effective* EoS parameters for the DM and DE;  $w_{\text{eff,DM}}$  and  $w_{\text{eff,DE}}$ , respectively. These effective parameters are defined such that, in the absence of non-minimal interaction, they would lead to the same functional forms  $\rho_{\text{eff,DM}}$  and  $\rho_{\text{eff,DE}}$  as obtained through the model-independent reconstruction processes by allowing a possible non-minimal interaction. Accordingly, one can write the following separate continuity equations for the DM and DE in terms of  $w_{\text{eff,DE}}$  and  $w_{\text{eff,DM}}$

$$\dot{\rho}_{\text{DM}} + 3H(1 + w_{\text{eff,DM}})\rho_{\text{DM}} = 0, \quad (5.6)$$

$$\dot{\rho}_{\text{DE}} + 3H(1 + w_{\text{eff,DE}})\rho_{\text{DE}} = 0, \quad (5.7)$$

and then, comparing these with the continuity equations that involve the interaction kernel, i.e., 5.4 and 5.5, we reach the following relation between the effective EoS parameters of the DM and DE and the interaction kernel:

$$w_{\text{eff,DM}} = \frac{-Q}{3H\rho_{\text{DM}}}, \quad w_{\text{eff,DE}} = w_{\text{DE}} + \frac{Q}{3H\rho_{\text{DE}}}. \quad (5.8)$$

It is also convenient to define a dimensionless interaction kernel parameter as follows;

$$\Pi_{\text{DM}} = \frac{-Q}{3H\rho_{\text{c},0}} = -\Pi_{\text{DE}}, \quad (5.9)$$

where  $\rho_{\text{c},0} = 3H_0^2/8\pi G$  is the critical energy density of the present-day universe. Now, let's see how  $Q = Q(z)$  should behave so that some appropriate priors for the reconstruction can

be chosen. It is widely accepted that, despite its problems,  $\Lambda$ CDM is very good at explaining most observations, so any made efforts should not differ significantly from it, despite the model-independent nature of the reconstructions used. For a comprehensive understanding of the impact of this interaction, perturbation analysis should also be included in this analysis. However, the focus in this chapter, as a proof of the concept, is on the background data and therefore the full analysis including perturbations will be left for future research. On the other hand, this does not mean that perturbations have been completely ignored here, as their effects are already reflected when choosing the prior ranges for  $\Pi_{\text{DE}}$ . In order to preserve the dust-like behavior of the DM and avoid significantly altering the perturbations, thus not spoiling the structure formation, one may demand that  $w_{\text{eff,DM}} \sim 0$  [179, 48, 238], which implies  $|\frac{Q}{3H\rho_{\text{DM}}}| \sim 0$ , then  $|\frac{Q}{3H}| \ll \rho_{\text{DM}}$ . Namely, we cannot have  $\frac{Q}{3H} \sim \rho_{\text{DM}} > 0$  otherwise the universe would always remain in the matter dominated era (viz., in the Einstein-de Sitter universe phase). Also, it is preferable to prevent  $\frac{Q}{3H} < 0$  and  $|\frac{Q}{3H}| \sim \rho_{\text{DM}}$  otherwise the universe would have never entered the matter dominated era and the successful explanation of galaxy and large-scale structure formation would be spoiled. With some algebra and using previously explained definitions one can arrive at  $|\Pi_{\text{DE}}| \ll \Omega_{\text{m}} \frac{H^2}{H_0^2}$ . Recent studies [43, 259] found that when using current cosmological data, the interaction could be so intense as to imply that the EoS of DM can reach values of  $w_{\text{eff,DM}} \sim 1/3$ . These results can be of use as a motivation to relax the constrain on  $\Pi_{\text{DE}}$ , so the dimensionless interaction kernel will be allowed to behave as  $|\Pi_{\text{DE}}| \sim \Omega_{\text{m}} \frac{H^2}{H_0^2}$ . These restrictions will be used as a guide when proposing the priors for the reconstruction of  $\Pi_{\text{DE}}(z)$  in [5.3] and the curve  $\Omega_{\text{m}} H^2 / H_0^2$  will be plotted as a reference.

By using the dimensionless interaction kernel together with the chain rule and  $\rho_{c,0}$ , we can express [5.4] and [5.5] as

$$\frac{d(\rho_{\text{DM}}/\rho_{c,0})}{dz} = \frac{3}{1+z} \left( \frac{\rho_{\text{DM}}}{\rho_{c,0}} + \Pi_{\text{DM}} \right), \quad (5.10a)$$

$$\frac{d(\rho_{\text{DE}}/\rho_{c,0})}{dz} = \frac{3}{1+z} \left[ (1 + w_{\text{DE}}) \frac{\rho_{\text{DE}}}{\rho_{c,0}} + \Pi_{\text{DE}} \right], \quad (5.10b)$$

respectively. These continuity equations are then solved numerically and used to express the Friedmann equation, i.e.,  $H(z)$ . The continuity equations for radiation and baryonic matter do not change, so we have, assuming a spatially flat universe:

$$\frac{H^2(z)}{H_0^2} = \Omega_{b,0}(1+z)^3 + \frac{\rho_{\text{DM}}(z)}{\rho_{c,0}} + \frac{\rho_{\text{DE}}(z)}{\rho_{c,0}}, \quad (5.11)$$

where radiation has been neglected, as it is well negligible in the post-recombination universe.

In [237] it was demonstrated that an equivalence between dynamical DE (through a dynamical EoS parameter) and an interacting DE-DM model (with a constant EoS parameter) exists

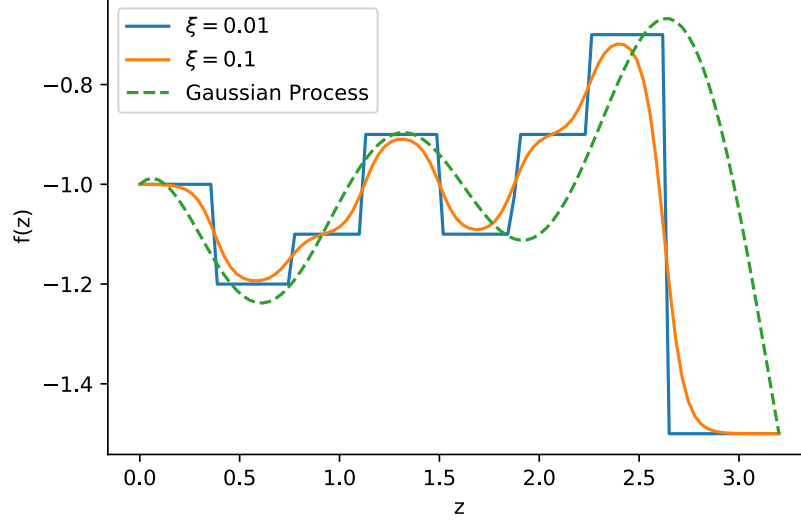


Figure 5.1: Comparison between a Gaussian Process for interpolation and a step function approach. The influence of the smoothness parameter  $\xi$  in the Binning scheme is also shown.

at the background level. To avoid this and to maintain as little bias as possible regarding the underlying possible functional form of the dimensionless interaction kernel parameter  $\Pi_{\text{DE}}(z)$ , the reconstruction efforts will be aimed mainly towards the interaction kernel but letting the EoS parameter to be a variable single bin  $w_0$ . Reconstructing both functions with model independent approaches, with a large number of extra parameters at the same time, could cause a lot of degeneracies with [\[5.8\]](#) but it may be worth to do it in future works.

Finally, for the sake of comparison Solano's dimensionless interaction function [\[218\]](#) will be plotted:

$$I_Q(z) = \frac{Q(z)}{\rho_{c,0}H(z)(1+z)^3}, \quad (5.12)$$

which is proposed as a way to better visualize the interaction kernel and its defining characteristics.

### 5.3 Binned and Gaussian Process interpolations

The reconstruction methods considered in this chapter are the Binning scheme and the GP.

Analogous to the binning approach, the GP will be used as an interpolation between nodes in order to have a model-independent reconstruction in a similar fashion as the reconstruction



performed in [112]. This method yields slightly different results than the Binning scheme as seen in 5.1. The node values are located at  $z_i$  to describe  $\Pi_{\text{DE}}(z_i)$ . The  $z_i$  values remain fixed, so the free parameters for the interaction kernel would be the amplitudes  $\Pi_{\text{DE}}(z_i) = \Pi_i$ . In the present chapter, and without loss of generality, for the reconstruction of  $\Pi_{\text{DE}}$  five amplitudes (parameters) will be utilized, evenly located across the interval of  $0.0 \leq z \leq 3.0$ . This choice implies that each amplitude encompasses a redshift interval of 0.6 when using bins. Alternatively, when utilizing GP the positions of the parameters  $\Pi_i$  are located in the following positions [0.0, 0.75, 1.5, 2.25, 3.0].

## 5.4 Datasets and Methodology

In this chapter, the data used includes the collection of cosmic chronometers [135, 215, 223, 160, 260, 158, 159] (we will refer to this dataset as H), which can be found within the repository [151]. Also the data includes the full catalogue of supernovae from the Pantheon+ SN Ia sample, covering a redshift range of  $0 < z \lesssim 2.26$  [210] (which will be referred to as SN). Finally the BAO datasets will be employed, containing the SDSS Galaxy Consensus, quasars and Lyman- $\alpha$  forests [21]. The sound horizon is calibrated by using BBN [76]. This dataset will be referred to as BAO.

To find the best-fit values for the free parameters of the model, SimpleMC [1, 33] is used again with the `dynesty` library [219]. The number of live-points were selected using the general rule  $50 \times ndim$  [134], where  $ndim$  is the number of parameters to be sampled. The flat priors used for the base parameters are:  $\Omega_m = [0.1, 0.5]$  for the matter density parameter,  $\Omega_b h^2 = [0.02, 0.025]$  for the physical baryon density,  $h = [0.4, 0.9]$  for the dimensionless Hubble constant  $h = H_0/100 \text{ km s}^{-1} \text{ Mpc}^{-1}$ . For comparison the  $w$ CDM model  $w_{\text{DE}}(z) = w_c$ , the Chevallier-Polarski-Linder (CPL) EoS parameter  $w_{\text{DE}}(z) = w_0 + w_a \frac{z}{1+z}$  [68] and the sign-switch interaction kernel (SSIK)  $Q = 3\sigma H(\rho_{\text{DE}} - \alpha\rho_{\text{DM}})$  [224] will be included. Their free parameters being  $w_c$ ,  $w_0$  and  $w_a$  for  $w$ CDM and CPL; for SSIK  $w_0 = [-2.0, 0.0]$ ,  $\sigma = [0.0, 1.0]$  and  $\alpha = [0, 4]$ . The flat prior for  $w_c$ , and  $w_0$ , is the same  $[-2.0, 0.0]$  and the flat prior used for  $w_a$  is  $[-2.0, 2.0]$ . For the reconstruction of  $\Pi_{\text{DE}}(z)$  let's recall that  $|\Pi_{\text{DE}}| \sim \Omega_m(z)E^2(z)$  will be used as a loose guide as mentioned before to choose the priors, which will be defined as  $\Pi_{\text{DE},i} = [-2.0, 2.0]$  when  $z < 1.0$  and  $\Pi_{\text{DE},i} = [-15.0, 15.0]$  when  $z > 1.0$ . Regarding the EoS parameter we either fix it to a cosmological constant  $w_0 = -1$  or let it vary as a free parameter  $w_0 = [-2.0, 0.0]$ .

## 5.5 Results

In this section the constraints are presented, at 68% CL, for  $h$  and  $\Omega_{m,0}$ , along with a comparison of the best-fit of the model  $-2\Delta \ln \mathcal{L}_{\max}$  and the Bayes Factor, with respect to  $\Lambda$ CDM, shown in [5.1](#) for all the scenarios. Moreover, the posterior probability density functions are shown, at 68% and 95% CL, for some quantities of interest in the interacting scenarios in [5.2](#), [5.3](#), [5.4](#) and [5.5](#).

Beginning with the well known parameterizations  $w$ CDM and CPL, and by using all the combined datasets, i.e., BAO+H+SN, the following constraints on the parameters were obtained:  $w_c = -0.99 \pm 0.06$ ,  $w_0 = -1.01 \pm 0.08$  and  $w_a = 0.12 \pm 0.47$ . Their  $-2\Delta \ln \mathcal{L}_{\max}$  are almost similar, among each other, with an improvement of 2.73 for  $w$ CDM and 2.81 for CPL with respect to the  $\Lambda$ CDM case, for one and two additional degrees of freedom, respectively (see also [5.1](#)). The SSIK parameterization has, instead, three extra parameters with constraints  $w_0 = -0.91 \pm 0.05$ ,  $\alpha = 0.97 \pm 0.79$  and  $\sigma = 0.061 \pm 0.053$ , and it presents a similar, albeit slightly better, fit of the data like the former parameterizations, with  $-2\Delta \ln \mathcal{L}_{\max} = -3.12$ . The evidences obtained favor  $w$ CDM over CPL and SSIK, with SSIK being the worst overall of the three parameterizations, which is not surprising as it has three extra parameters. Still when comparing any of the three scenarios with the standard cosmological model, even if they improve the fit of the data, the evidence is slightly against them, because models with additional parameters are more complex and therefore penalized by the Occam's razor principle.

Then the reconstructions using five nodes interpolated via Gaussian Process for  $\Pi(z)$  were performed in two ways. One has an EoS parameter  $w = -1$ , for which  $-2\Delta \ln \mathcal{L}_{\max} = -3.89$  was obtained, and this represents an improvement of almost  $2\sigma$  over the standard model. The other one with a variable EoS parameter  $w_0 = -0.81 \pm 0.16$  with  $-2\Delta \ln \mathcal{L}_{\max} = -4.22$ , which is slightly better and suggests small deviations from  $w = -1$ . This stands out as the best model (when looking at the fitness of the data) among the reconstructions. The main feature found in the functional posterior of  $\Pi_{\text{DE}}(z)$ , shown in [5.2](#) and [5.3](#) (bottom right panel), is the presence of an oscillatory-like behavior around  $\Pi_{\text{DE}} = 0$ . This behavior is present at one sigma level when  $w = -1$  and becomes more pronounced when the DE EoS parameter is free to vary. In fact it is noticeable the presence of two maxima, one located at  $z \sim 0.4$  and a more prominent one at  $z \sim 2.3$ , with deviations slightly outside the  $1\sigma$  region. Additionally, there is also a local minimum at  $z \sim 1.3$ . Interestingly, all of them align closely with the positions of the BAO Galaxies and BAO Ly- $\alpha$  data, represented by the red error bars in the second panel of the figures. The reconstruction of  $\Pi(z)$  indicates more than one sign change in the flux of energy

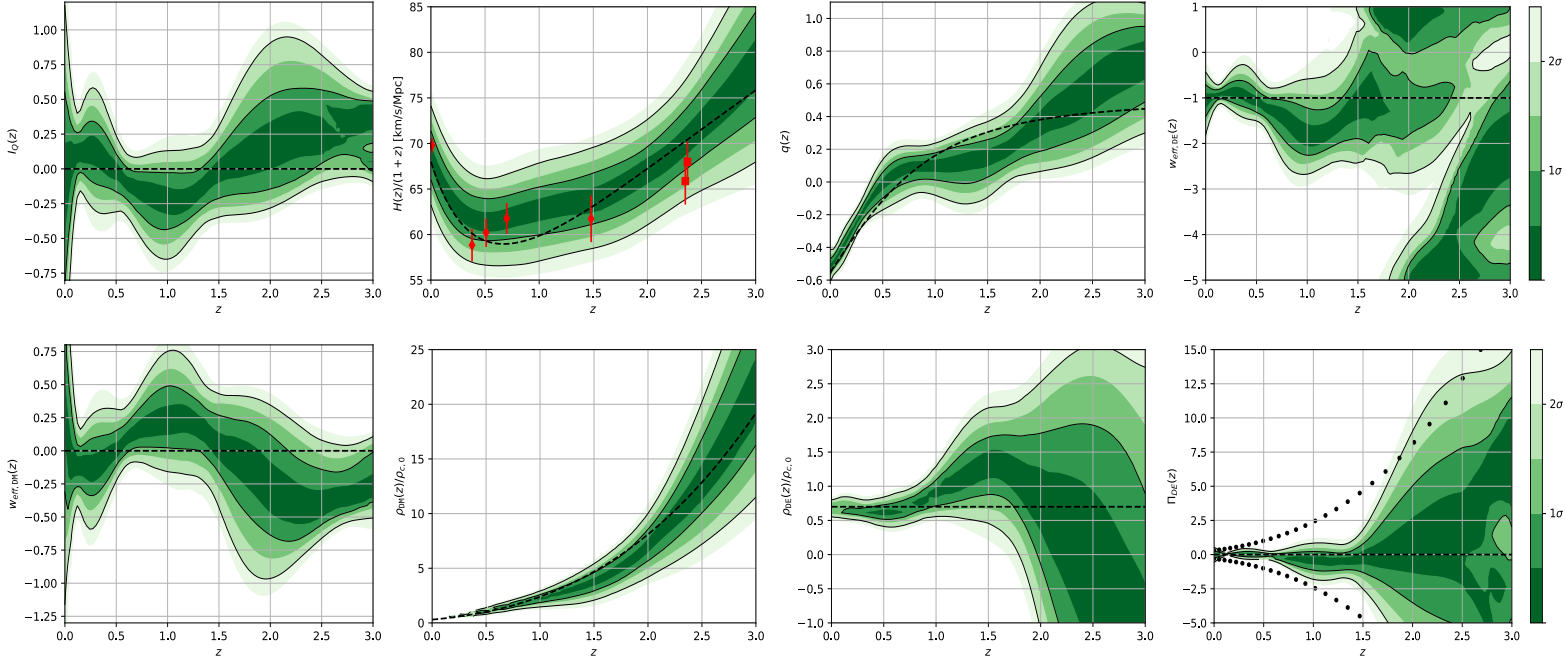


Figure 5.2: Functional posterior probability of the reconstruction by using a Gaussian Process and  $w = -1$ . The probability as normalised in each slice of constant  $z$ , with colour scale in confidence interval values (see color bar at the right). The 68% ( $1\sigma$ ) and 95% ( $2\sigma$ ) confidence intervals are plotted as black lines. From left to right in the upper part: the rescaling function  $I_Q(z)$ , the Hubble Parameter, the deceleration parameter and the effective EoS parameter for DE. In the lower part: the effective EoS parameter for DM, the density for DM and DE respectively and the dimensionless interaction kernel  $\Pi_{DE}$ . The dashed black line corresponds to the standard  $\Lambda$ CDM values and the dotted line in the  $\Pi_{DE}(z)$  plot corresponds to the  $\Omega_m H(z)^2 / H_0^2$  curve.

density transfer, that is, when the kernel switches from positive to negative the energy flow changes direction, i.e., in other words, at the beginning there is a flux of energy in the direction of DE to DM, followed by a transition and thus the flux of energy reverses from DM to DE. The physical mechanism which makes this possible is beyond the scope of this work but it is important to note that similar results have been obtained before in [58] with older versions of the data sets.

Once the reconstruction of  $\Pi(z)$  has been performed, one is able to extract some derived features, shown in [5.2, 5.3]. Here there are the plots of the functional posteriors for the quantities:  $H(z)/(1+z)$  (corresponds to expansion speed of the universe, i.e.,  $\dot{a}$  with  $a$  being the scale factor), Solano's dimensionless interaction function  $I_Q(z)$ , the deceleration parameter  $q(z)$ , the two effective EoS parameters ( $w_{\text{eff,DM}}$  and  $w_{\text{eff,DE}}$ ), and both energy densities ( $\rho_{\text{DM}}/\rho_{c,0}$  and  $\rho_{\text{DE}}/\rho_{c,0}$ ). Both figures present a similar structure in the results, but the case where the EoS parameter is

free to vary (Fig. 5.3) is a bit more pronounced, hence let's focus on this case. The general form of  $\Pi(z)$ , including its oscillatory behavior, is transferred to the derived functions. For instance, and as noted before, the presence of maxima in the interaction kernel may be able to explain the BAO data. This can be seen in the panel with  $H(z)/(1+z)$ , which contributes to alleviate the BAO tension created between low redshift (galaxies) and high (Ly- $\alpha$ ) data, explored in [33, 11]. The fact that the general form of  $H(z)/(1+z)$  changed, causes a displacement of its minimum value which in turn moves the beginning of the acceleration epoch to lower values of redshift, i.e.  $q(z) = 0$  at  $z \sim 0.5$  at 68% CL away from the  $\Lambda$ CDM value. The main differences of the  $\Lambda$ CDM and the reconstructed IDE are accentuated on the functional posterior of the re-escalation function  $I_Q(z)$ . Here we notice the existence of regions where the standard model remains outside the 68% CL ( $1-\sigma$ ), which could motivate further studies of an interaction kernel which presents oscillations. The general tendency of this function also resembles a previously obtained result in [50] with regards to the predominant negative values at late times. The last reconstructed derived features are the effective equations of state parameters and the energy densities. The effective EoS parameter of the DE, at low redshift, resembles a Quintom-like behavior crossing the phantom-divide-line (PDL), viz.,  $w = -1$ , multiple times; as studied in [232]. A primary characteristic of the effective EoS parameter is exhibiting a pole (viz.,  $\lim_{z \rightarrow z_{\dagger}^{\pm}} w_{\text{DE}}(z) = \pm\infty$  with  $z_{\dagger}$  being the singular point). As studied in previous works [16, 17, 102, 181] this is necessary when a transition to a negative energy density is present, and this can also be easily verifiable by looking at the DE density,  $\rho_{\text{DE}}/\rho_{c,0}$ , which allows a transition to negative values at about  $z \sim 2.3$ . As a consequence of the interacting mechanism, the DM effective EoS parameter also shows some oscillations, although it is still statistically in agreement with  $w_{\text{DM}} = 0$ . Because the effective DM EoS parameter is a function of  $Q(z)$  one finds that, if  $Q(z) \neq 0$  then the DM would be no longer exhibit  $\rho \propto a^{-3}$ , i.e., no longer behave like a fluid with a pressure identical to zero. This result is similar to the one obtained in [143], where the term used for a DM with a dynamic EoS parameter was named Generalized dark matter (GDM). On the other hand, its energy density shows a tendency towards smaller values than  $\Lambda$ CDM (dashed line) at low redshifts, a possible transition to null or negative values at  $z \sim 2.3$  and then larger values at higher redshifts. This is a consequence of the changing direction in the energy transfer.

Next the results of the reconstruction using bins instead of GP are presented. The functional posteriors can be seen in 5.4 ( $w = -1$ ) and 5.5 ( $w = w_0$ ). They look quite similar to the general features of the GP counterparts. When having  $w = -1$  a  $-2\Delta \ln \mathcal{L}_{\text{max}} = -3.88$  is obtained, and if the DE EoS parameter is allowed to vary one gets  $w_0 = -0.98 \pm 0.09$  and  $-2\Delta \ln \mathcal{L}_{\text{max}} = -3.92$

Table 5.1: Mean values, and standard deviations, for the parameters used throughout the reconstructions. For each model, the last two columns present the Bayes Factor, and the  $-2\Delta \ln \mathcal{L}_{\max} \equiv -2 \ln(\mathcal{L}_{\max, \Lambda\text{CDM}}/\mathcal{L}_{\max, i})$  for fitness comparison. The datasets used are BAO+H+SN. Here  $-2 \ln \mathcal{L}_{\max, \Lambda\text{CDM}} = 1429.7$ ,  $\ln E_{\Lambda\text{CDM}} = -721.35(0.14)$ .

Model	EoS parameter	$h$	$\Omega_{m,0}$	$\ln B_{\Lambda\text{CDM},i}$	$-2\Delta \ln \mathcal{L}_{\max}$
$\Lambda\text{CDM}$	-1	0.683 (0.008)	0.306 (0.013)	0	0
$w\text{CDM}$	$w_c$	0.675 (0.022)	0.296 (0.016)	1.51 (0.18)	-2.73
CPL	$w_0 + w_a(1 - a)$	0.676 (0.023)	0.298 (0.019)	2.37 (0.19)	-2.81
SSIK	$w_0$	0.681 (0.025)	0.303 (0.027)	3.82 (0.21)	-3.12
$\Pi_{\text{DE}}$ GP	-1	0.684 (0.027)	0.321 (0.032)	8.61 (0.21)	-3.89
	$w_0$	0.687 (0.027)	0.311 (0.024)	8.01 (0.21)	-4.22
$\Pi_{\text{DE}}$ bins	-1	0.684 (0.025)	0.319 (0.027)	5.69 (0.22)	-3.88
	$w_0$	0.689 (0.027)	0.314 (0.025)	7.51 (0.22)	-3.92

Table 5.2: Constraints at 68% CL of the parameters for the model-independent reconstructions. The values for  $\Pi_4$  are unconstrained for some of the cases, and for  $\Pi_5$  for every case, which is expected given the lack of data in this redshift.

Model	$w_0$	$\Pi_1$	$\Pi_2$	$\Pi_3$	$\Pi_4$	$\Pi_5$
$\Pi_{\text{DE}}$ GP	-1	-0.01(0.26)	-0.26(0.36)	-0.29(1.04)	0.93(5.34)	unconstr.
	-0.81(0.16)	-0.78(0.71)	-0.16(0.39)	-0.22(1.14)	5.35(5.82)	unconstr.
$\Pi_{\text{DE}}$ bins	-1	0.04(0.05)	-0.61(0.56)	0.54(3.16)	unconstr.	unconstr.
	-0.98(0.09)	0.02(0.06)	-0.43(0.76)	0.18(3.55)	unconstr.	unconstr.

with respect to the  $\Lambda\text{CDM}$  scenario, improving the fit of the data and also performing slightly similar the reconstruction made with the GP interpolation. The results for this case also present oscillations around the null value of the interaction kernel  $\Pi_{\text{DE}} = 0$  which, again, indicates more than one shift in the direction of energy density transfer. However, by using bins, the oscillations are noisier and thus more difficult to spot than in the one performed using GP; the results of the two cases, with fixed or varying EoS parameter, are very similar to each other. As far as the reconstructed derived features, there is a similar behavior to that found with GP. The re-escalation function  $I_Q(z)$ , for example presents some oscillatory-like behavior that is less pronounced than the GP case, but lacks the first peak at redshift  $z \sim 0.5$ . The Hubble parameter presents a horizontal flat region (darker green). However, due to the larger confidence contours,

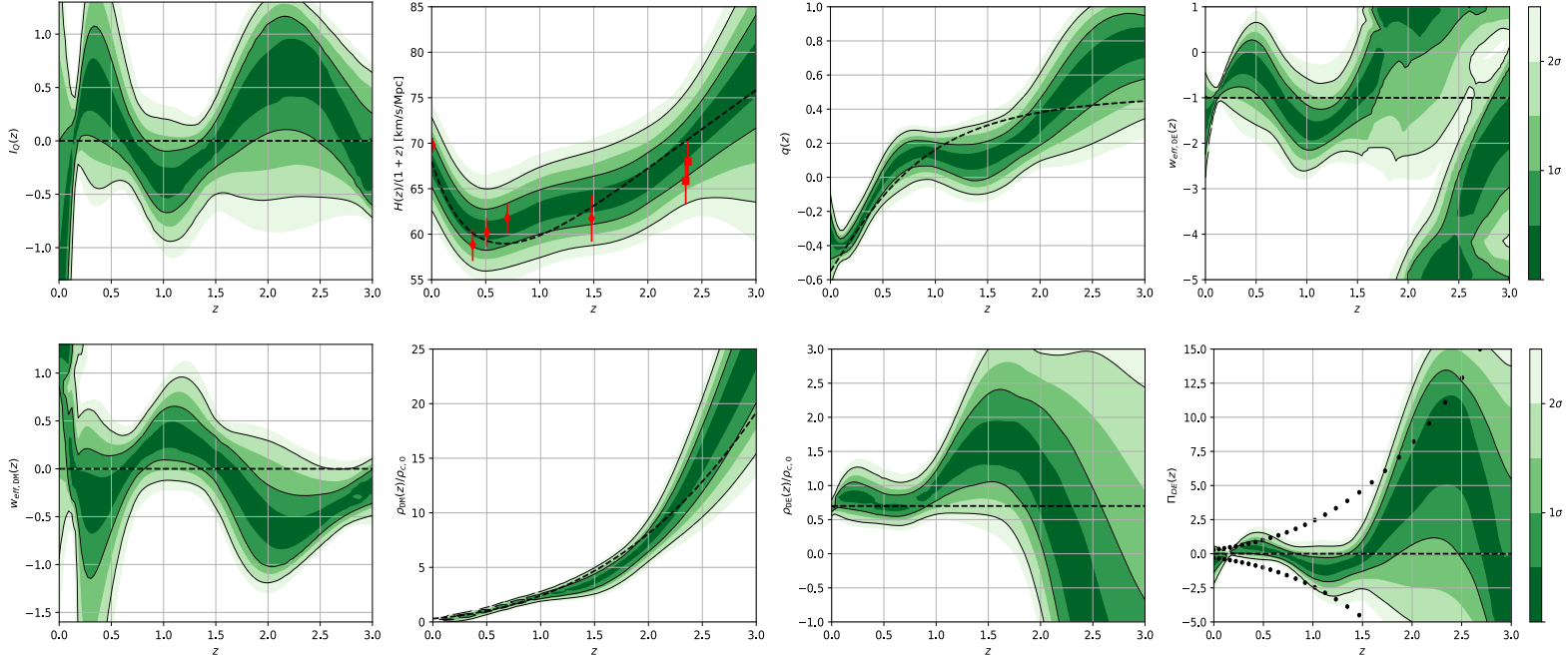


Figure 5.3: Functional posterior probability of the reconstruction by using a Gaussian Process and  $w = w_0$ .

The probability as normalised in each slice of constant  $z$ , with colour scale in confidence interval values. The 68% ( $1\sigma$ ) and 95% ( $2\sigma$ ) confidence intervals are plotted as black lines. From left to right in the upper part: the reescalation function  $I_Q(z)$ , the Hubble Parameter, the deceleration parameter and the effective EoS parameter for DE. In the lower part: the effective EoS parameter for DM, the density for DM and DE respectively and the dimensionless interaction kernel  $\Pi_{\text{DE}}$ . The dashed black line corresponds to the standard  $\Lambda\text{CDM}$  values and the dotted line in the  $\Pi_{\text{DE}}(z)$  plot corresponds to the  $\Omega_m H(z)^2 / H_0^2$  curve.

it causes the existence of a region where the deceleration parameter equals zero,  $z \sim 0.5 - 1.2$ . Finally, the effective DE EoS parameter presents again a pole, but in this case closer to  $z = 2$ , which suggests a transition to a negative DE density,  $\rho_{\text{DE}}(z)/\rho_{c,0}$ ; and the effective DM EoS parameter shows deviations zero at more than  $1\text{-}\sigma$  level. These similar behaviors were expected as both model-independent reconstructions have similar degrees of freedom and the demeanor in which the nodes/bins are interpolated also have some visual similarities (as seen in [5.1](#) depending on the smoothness of the bins).

In [Table 5.1](#) the mean values and standard deviations for the parameter estimation procedure are presented. Every model-independent reconstruction, regardless of its improvement in the fit of the data, presents a worse Bayes' Factor when compared to  $\Lambda\text{CDM}$ , because additional degrees of freedom are penalized by the Occam's razor principle. In [Figure 5.6](#) the 1D and 2D marginalized posteriors of the parameters corresponding to  $\Pi(z)$  are plotted and in [Table 5.2](#)

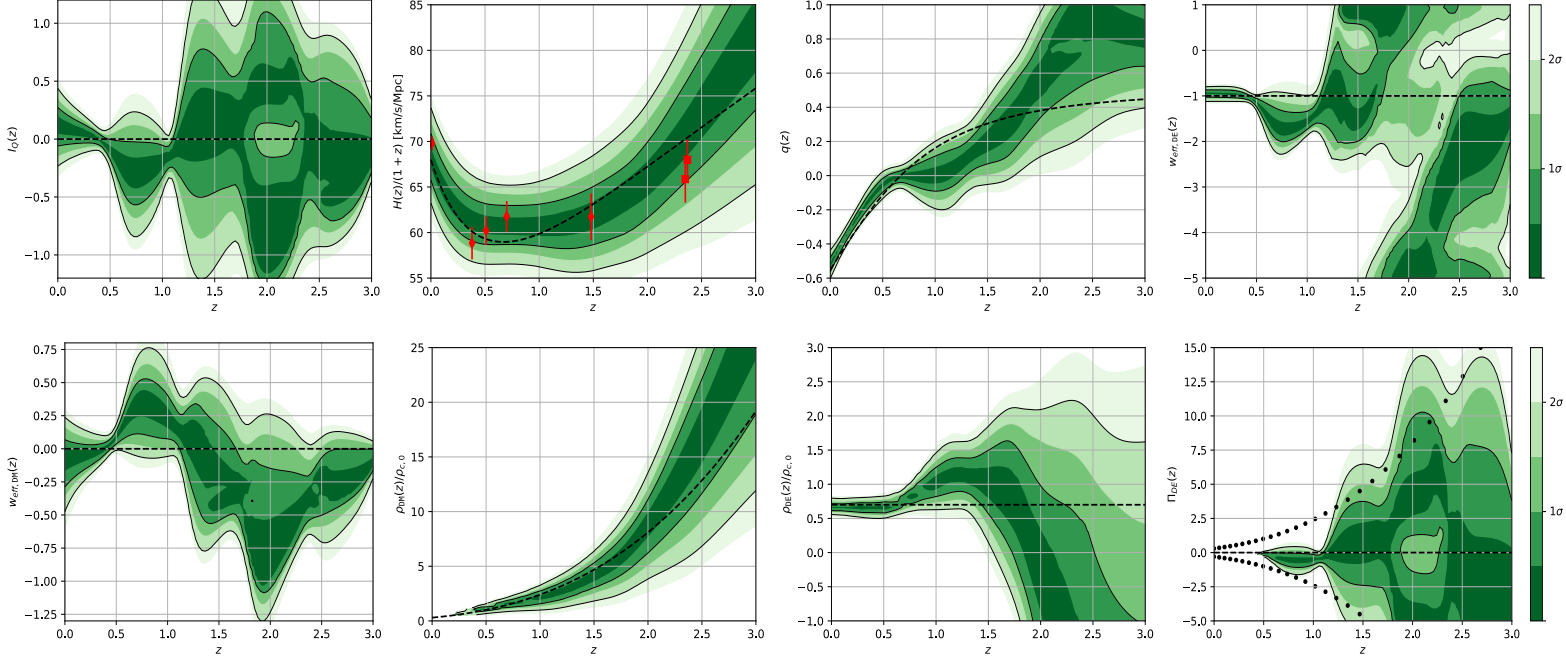


Figure 5.4: Functional posterior probability of the reconstruction by using a Binning scheme and  $w = -1$ . The probability as normalised in each slice of constant  $z$ , with colour scale in confidence interval values. The 68% ( $1\sigma$ ) and 95% ( $2\sigma$ ) confidence intervals are plotted as black lines. From left to right in the upper part: the rescaling function  $I_Q(z)$ , the Hubble Parameter, the deceleration parameter and the effective EoS parameter for DE. In the lower part: the effective EoS parameter for DM, the density for DM and DE respectively and the dimensionless interaction kernel  $\Pi_{DE}$ . The dashed black line corresponds to the standard  $\Lambda$ CDM values and the dotted line in the  $\Pi_{DE}(z)$  plot corresponds to the  $\Omega_m H(z)^2/H_0^2$  curve.

their constraints at 68% CL are reported, where the error is shown in parenthesis. The parameter  $\Pi_1$ , which is located in  $z = 0$  for GP, is clearly better constrained when taking  $w = -1$ , although its constraint is around  $\Pi_1 = 0$ , which indicates that, without a variable EoS parameter, it is pretty much forced to behave as  $\Lambda$ CDM at low redshifts.

When allowing variations on  $w_0$ , it is easy to note a separation from a  $\Lambda$ CDM-like behavior of around  $1.5\sigma$  in  $\Pi_1$  for GP. In contrast, when using bins this parameter is well constrained with or without a varying  $w_0$ . This happens because each bin spans a range ( $\Delta z = 0.6$  in this case) and, specifically the first bin, is fitting all the available data in  $0 < z < 0.6$  with a single step function making it very constrained, unlike its GP counterpart which uses both  $\Pi_1$  and  $\Pi_2$  (interpolated in  $0 < z < 0.75$ ). Another interesting observation is that the restriction in  $\Pi_1$  is reflected in the posterior of  $w_0$ , allowing it to be higher than  $-1$  and presenting a negative correlation with  $\Pi_1$  when using GP. The parameter  $\Pi_3$  on the other hand, appears to be more

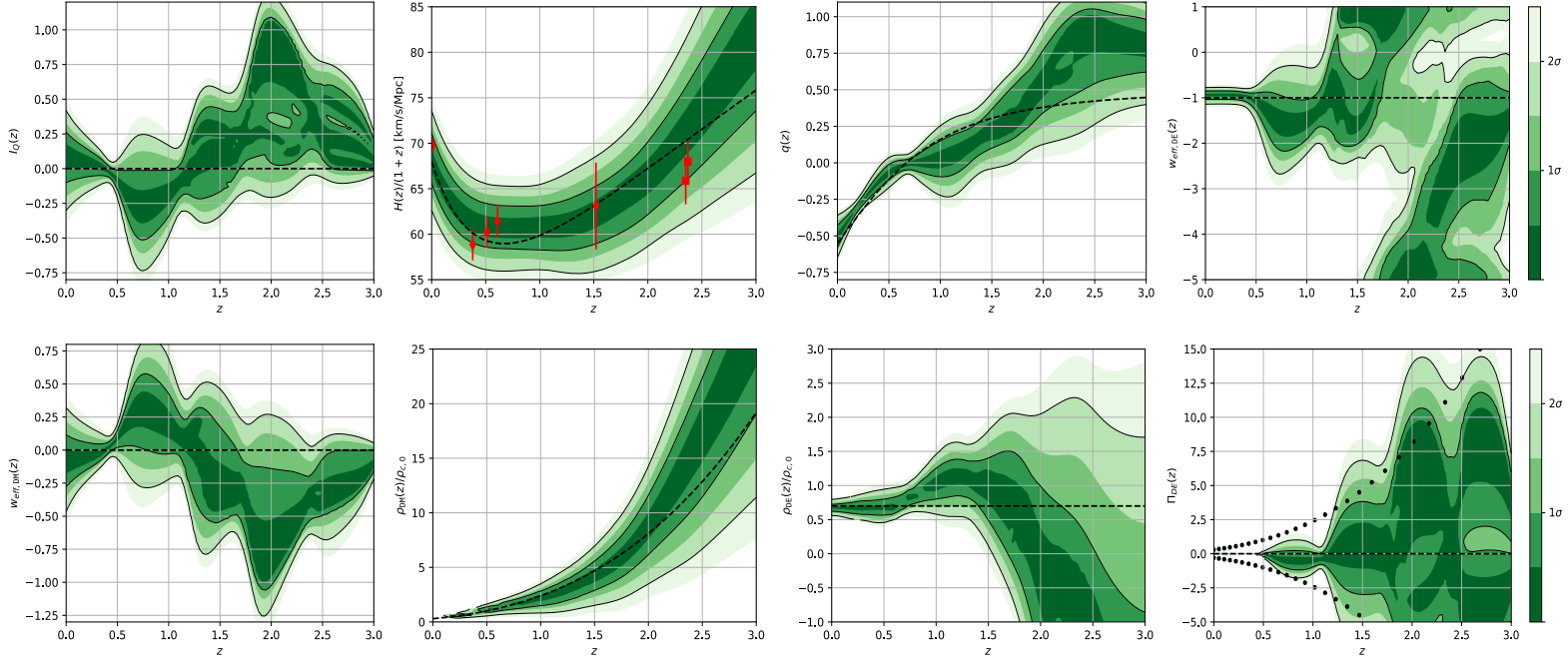


Figure 5.5: Functional posterior probability of the reconstruction by using a Binning scheme and  $w = w_0$ . The probability as normalised in each slice of constant  $z$ , with colour scale in confidence interval values. The 68% ( $1\sigma$ ) and 95% ( $2\sigma$ ) confidence intervals are plotted as black lines. From left to right in the upper part: the reescalation function  $I_Q(z)$ , the Hubble Parameter, the deceleration parameter and the effective EoS parameter for DE. In the lower part: the effective EoS parameter for DM, the density for DM and DE respectively and the dimensionless interaction kernel  $\Pi_{DE}$ . The dashed black line corresponds to the standard  $\Lambda$ CDM values and the dotted line in the  $\Pi_{DE}(z)$  plot corresponds to the  $\Omega_m H(z)^2 / H_0^2$  curve.

constrained with GP than with bins. One can also see from the marginalized 1D posteriors that the parameter  $\Pi_4$  is loosely constrained when using GP but unconstrained with bins. This different behavior could be attributed to the slight correlation imposed by the GP method, but also when  $w_0$  is allowed to vary we see it is correlated with  $\Pi_4$ , and at the same time  $\Pi_4$  is correlated with  $\Pi_1$  which is also constrained.  $\Pi_5$  is completely unconstrained in all cases, but this was expected given the lack of data in this region ( $z > 2.4$ ).

Despite the significant findings presented above, it should be noted that the standard  $\Lambda$ CDM model still remains a viable option within the  $2\sigma$  confidence level, which means that one cannot definitely exclude it with the data used in this chapter, and it is needed additional and more precise data sets to be able to say anything solid about this possibility. Let's continue with a brief discussion of the differences and similarities between the findings from the two different reconstruction approaches used. For instance, it can be easily seen that certain characteristics



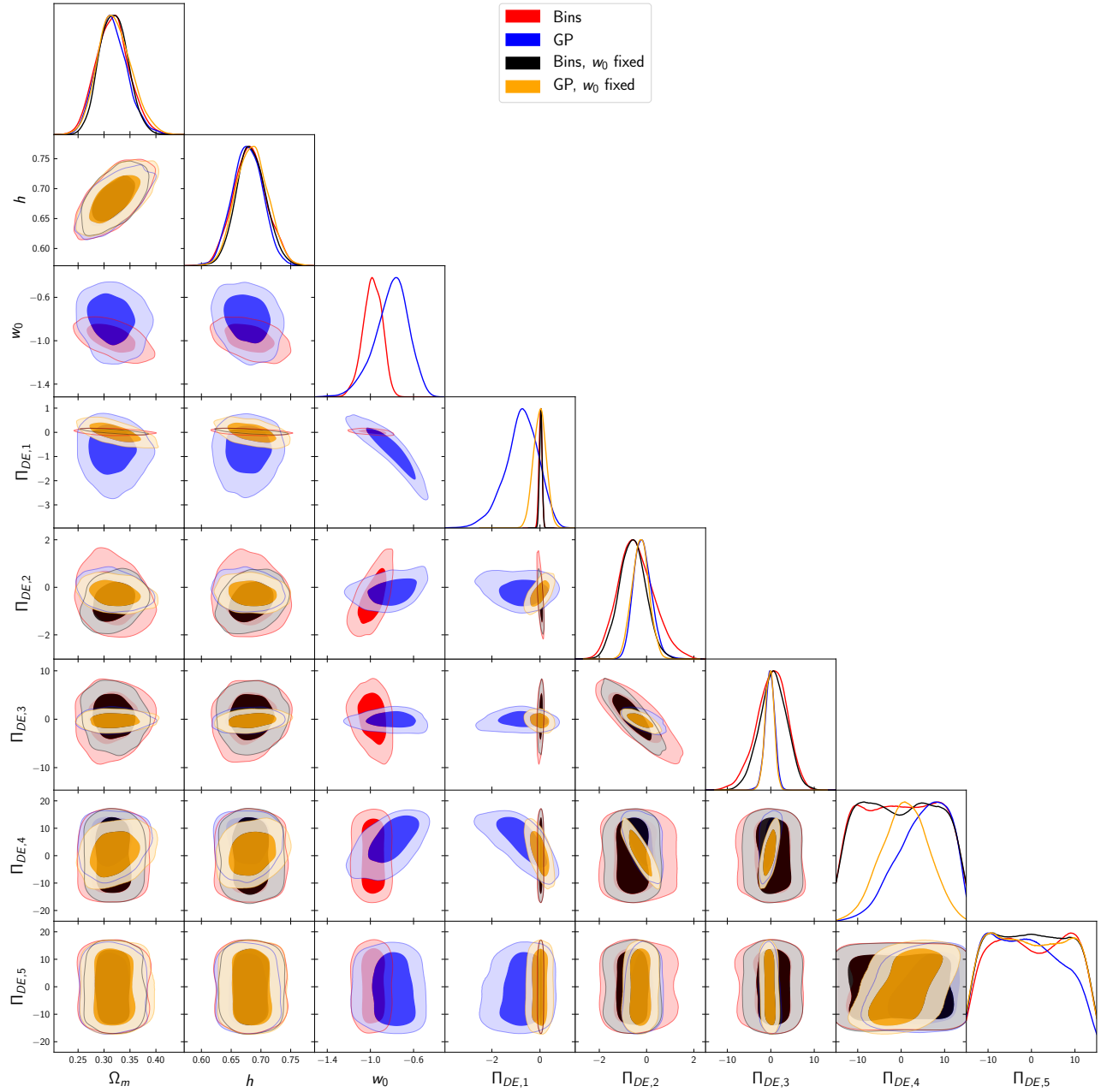


Figure 5.6: Triangle plot of every model-independent reconstruction. The parameter  $w_0$  is only present in two of the reconstructions and it is correlated with  $\Pi_{DE,1}$  when using a GP to perform the interpolation.

are more evident in the GP reconstruction than in the binning method. This discrepancy could be attributed to the inherent correlations existing within GP among nodes, a correlation that is subtly reflected in the confidence contours shown in Fig. 5.6. These correlations seem to favor the GP approach, which is evidenced by a better fit of this approach to the data as can be seen in Table 5.1. To reconcile these discrepancies among the approaches, a straightforward solution involves increasing the number of parameters, thereby achieving higher resolution. Nonetheless, this approach introduces the challenge of potential overfitting of specific characteristics and underfitting of others. To counterbalance this trade-off, one may need to incorporate a correlation function into the binning method [261, 102], but the consideration of this is beyond the scope of the present chapter although it might be a promising direction for future investigations. It seems reasonable to conclude from this discussion that some of the observed features may be influenced by the chosen reconstruction method, but certain general characteristics persist regardless of the approach. These enduring traits include the oscillatory behavior at  $1\sigma$ , the asymptotic behavior of the effective EoS and the possibility of a transition to a negative DE density.

This section will be concluded by commenting on one of the most interesting findings of this chapter, the possibility of the existence of a DE that can take negative density values at high redshifts (viz., for  $z \gtrsim 2$ ), regardless of the approach used. As seen in previous chapters this possibility may seem physically unexpected and challenging, but it is not a new finding. It has been studied in the previous literature, especially recently, to address the cosmological tensions such as the  $H_0$  and  $S_8$  tensions; see, for instance, Refs. [11, 17, 18, 14, 5] considering models that suggest such a transition at  $z \sim 2$  from their observational analysis and references therein for further reading. The findings here present a noteworthy distinction, as it was achieved a similar behavior by incorporating an interacting dark sector (dark matter+dark energy) instead of employing a direct reconstruction of the DE interacting only gravitationally. This observation holds significance as it indicates that the data sets consistently favor (or at the very least allow for) a negative DE density for  $z \gtrsim 2$ , irrespective of the method employed. This finding, combined with the model's potential to address certain cosmological tensions (as extensively discussed in [18, 14]), emphasizes the notion that this model emerges as a promising alternative to the standard  $\Lambda$ CDM model.

# Chapter 6

## Conclusions

The main goal of this thesis was to use different reconstruction methods to shed some light on what the possible nature of the Dark Energy could be, according to late-time background data. As explained before, reconstructions use observational data to infer or estimate a physical quantity or function, especially when the true underlying function is not directly observed. They are generally separated in three types: Parametric, Non-parametric and Model-Independent. The data used in this work is mainly background one and consists of: Cosmic Chronometer measurements of the Hubble Parameter, the JLA supernovae 1A catalogue, Pantheon and Pantheon Plus supernova compilation, Baryon Acoustic Oscillation data and the CMB as a high-redshift BAO. On this thesis, the main reconstruction methods used are the ones denominated as model-independent, although some parametric approaches were also used.

### 6.1 Graduated DE

The Graduated Dark Energy (gDE) can be viewed as characterising the minimum dynamical deviation from the null inertial mass density. In this case it yields an energy density that dynamically assumes negative values in the recent past, in line, for instance, with [\[34, 205, 90, 161, 190, 64, 242, 97, 234\]](#). It approximately describes the cosmological constant spontaneously switching sign at a certain redshift to become positive quite recently in the late universe.

The gDE-CDM model, replaced the  $\Lambda$  hypothesis by the gDE, was confronted with the latest (at that time at least) combined observational data sets of PLK+BAO+SN+ $H$ . When  $\lambda \leq -4$  (also when  $\lambda$  is free): that the data predicts bimodal posterior probability distributions for the parameters of the gDE-CDM model new maxima significantly far away from  $\gamma = 0$  ( $\Lambda$ CDM),

and old maxima containing  $\gamma = 0$ . The improvement in the goodness of the fit with respect to the  $\Lambda$  reaches highly significant levels –e.g.,  $\Delta\chi_{\min}^2 = 6$  when  $\lambda = -20$  and  $\Delta\chi_{\min}^2 = 6.4$  when  $\lambda$  is free– for the new maxima, while it remains always at insignificant levels  $-\Delta\chi_{\min}^2 \lesssim 0.02$ , irrespective of the value of  $\lambda$ – for the old maxima. It is shown that, in contrast to the old maxima covering the  $\Lambda$ CDM model, these new maxima of the gDE-CDM model also agree with the model-independent  $H_0$  measurements, high-precision Ly- $\alpha$  data, and model-independent  $Om h^2$  diagnostic estimates.

There are some features endowed by the new maxima of the gDE-CDM model which are due to the energy density of the gDE rapidly changing sign at the redshift  $z \approx 2.3$  and this in turn leads to a rapid drop in the total energy density of the universe, and in  $H(z)$ , at the same redshift. It has turned out that this happens for large negative values of  $\lambda$ , which renders the redshift dependency of the gDE density close to a step function, which to a good approximation describes a cosmological constant spontaneously switching sign. This can lead to a conjecture that the cosmological constant has spontaneously switched sign and became positive, namely, the universe has transitioned from AdS vacua to dS vacua, at  $z \approx 2.32$  and triggered the late-time acceleration. This could suggest looking for such mechanisms in string theory constructions. The fact that constructing metastable dS and/or AdS in string theory occupy a key place in the string theory investigations, indicates that the future confirmation or falsification of this conjecture would have far reaching implications for fundamental theoretical physics as well as for the identity of the dark energy.

## 6.2 Model-independent EoS and DE density

After characterizing and analyzing gDE the focus of this work shifted to parametric forms and model-independent reconstructions of two properties of the Dark Energy: the EoS and the energy density. Regarding the parametric forms, some attention was given to the  $w$ CDM and CPL models, whereas for the energy density a simple form given by a sigmoid function to describe a transition behaviour was introduced. Then, to allow for more flexibility for the recovered functions, two types of reconstructions were included: step functions smoothly connected (bins) and linear interpolations (nodes). Each of the reconstructions may have several amplitudes as free parameters with fixed locations, as well as variable positions to localize possible features. On the top of the bin reconstruction a floating prior that averages the set of neighboring amplitudes to behave as a mean between bins was incorporated.

The  $w$ CDM and CPL parameterizations of the EoS showed little to no improvement over

$\Lambda$ CDM. However, with just a single parameter, the sigmoid function for the energy density had a better fitness to data as well as a better Bayes' factor when compared to  $\Lambda$ CDM. Even though this parameterization is phenomenological, it could be an indication that these type of models should be further studied upon.

By adding complexity in the model-independent reconstructions, through extra amplitudes with fixed positions, the general outcome presented a dynamical behavior beyond the cosmological constant. In both reconstructed functions,  $\rho_{\text{DE}}(z)$  and  $w_{\text{DE}}(z)$ , there is a presence of a bump located at about  $z \sim 1.2$ . This feature along with a crossing to the phantom-divide-line in the EoS, and a transition to a null energy density (or even negative values) yield to deviations from a constant energy density of about  $3\sigma$ . However, for these type of reconstructions the Bayes factor penalized the incorporation of new parameters.

In order to avoid a possible bias due to the location of the amplitudes, the internal points were allowed to move freely in the  $z$ -space. The autonomy of the internal positions led to localize the features, previously mentioned, and to an improvement on the fit of about  $1\sigma$ , in comparison to the same number of amplitudes with fixed positions. Another point to stress out about the internal reconstructions, is the enhancement of the Bayes' factor which could get even negative values, i.e. for  $\rho_{\text{DE}}(z)$  with bins and the  $3y2x$  method. When considering 20 parameters in the binned reconstruction we noticed an improvement in the fitness up to about  $4\sigma$ . Nevertheless, a key result to bear in mind is that for the case of 20 bins+prior the Bayes's factor showed a strong evidence against this type of reconstruction. This is also reflected on a worse  $\Delta\chi^2$ , when compared to a reconstruction with the same number of parameters.

In general, the derived functions inherited the behaviour from the reconstructed ones: an oscillatory shape. These functions also exhibited consistency with other reconstruction methods. For instance, a dynamical DE behaviour, a different redshift transition from a decelerating universe to an accelerating one, a better agreement to the BAO data. From the energy density reconstruction, the derived EoS presents a discontinuity at redshift around  $z \sim 2$ , which is necessary if the energy density transitioned to negative values; found in several models and parameterizations.

By performing a PCA it is seen that, in both types of reconstructions, the amplitudes beyond  $z = 1.5$  are the least constrained, where the predominant data around these redshift values is the BAO Lyman- $\alpha$ . This shows that current Lyman- $\alpha$  BAO prefers a nearly null or negative energy density, or a transition from quintessence to a phantom dark energy. However, more precise data in this region is necessary to fully discern a dynamical DE, also, considering that the parameters in this region are unconstrained, it directly affects the estimation of the Bayesian Evidence, so

any remarks about the Bayes' Factor should be made carefully. Nevertheless it was found that some features could indeed be considered as signal, like the general oscillatory behaviour, the bump located at  $z \approx 1.2$  and the  $w_{\text{DE}} < -1$  at the present redshift.

### 6.3 Interacting DE with bins and GP

In chapter 5 a model-independent reconstruction of the interaction kernel between DM and DE by implementing an interpolation with both Gaussian Process and bins was made. The main results showed that particular features, such as oscillations are present, but they remain still statistically consistent with the  $\Lambda$ CDM model. Similar to the chapter before it, some derived functional posteriors were also obtained, which inherit the general characteristics of  $\Pi(z)$  (the adimensional interaction kernel). These oscillatory features can be more clearly observed through the rescaling function, and it is worth noting that similar shapes were also found in a model-independent reconstruction in [58]; (see also [12], suggesting that, in the relativistic cosmological models that deviate from  $\Lambda$ CDM, dark energies are expected to exhibit such behaviors for the consistency with CMB data). It is important to notice that the Hubble parameter was slightly modified in order to alleviate the tension created between low and high redshift BAO data (reflected in the improvement of fit) which also causes a shift, to later times, for the beginning of the acceleration epoch. When plotting the functional posterior of the DE effective EoS parameter, a quintom-like behavior at low redshift is observed, with a preference zone of the 68% confidence contour away from the  $\Lambda$ CDM. Additionally, the presence of a pole at about  $z \sim 2.3$  recovering a shape with an asymptote is observed, proposed and studied in other works [16, 17, 102, 116, 240]. This particular shape is required when having a DE energy density that presents a transition from positive to negative energy density or vice versa. This transition is present in the 68% contour of the derived DE energy density. An important implication of these reconstructions is seen with 5.8. Since the interaction kernel is non-negligible, thus the effective behavior of DM, at the largest scales, may not be described by a perfect pressure-less fluid but something around it.

### 6.4 Concluding remarks

Some concluding remarks can be summarized as follow:

- I) the gDE model presents an interesting alternative to the Cosmological Constant, specifically for its sign-switching density. Some models inspired by it are starting to show some

promise to solve the problems underlying the standard model;

- II) regarding the model-independent reconstructions: despite the positive outcomes observed in the fit of the data, we cannot ignore the Bayes' Factors, as the model-independent methods introduce several new parameters, they are expected to be in disadvantage when compared to the concordance model, but even so, some of them resulted in a better fit to the data (up to  $4\sigma$ ) and, in some cases, a better Bayes' Factor;
- III) if future surveys confirm these results, the cosmological constant and single scalar field theories (with minimal assumptions) might be in serious problems as they cannot reproduce the features presented by these reconstructions. This could be a great incentive to study DE models with some type of dynamical behavior and encourage direct reconstruction of other functions, such as those that may lead to discontinuities in the EoS;
- IV) the PCA analysis showed a great promise for some of the reconstructed features, such as the oscillations and a bump at intermediate redshifts, but at the same time it exhibited the possibility of some of them to be due to noisy data;
- finally V) it deserves a mention that both reconstructions from chapters [4](#) and [5](#), even when the reconstructions are fundamentally distinct (one directly reconstructs the EoS and density and the other an IDE model), show that a sign-switching energy density (such as the gDE model) is allowed and sometimes preferred by the datasets used.

As a future prospect, it remains the addition of other datasets that contain information from linear perturbations, such as the cosmic microwave background and the matter power spectrum data. It would also be interesting to study some alternative PCA methods that have a mathematical basis to truly discern important features from noise.





## Chapter 7

# Bibliography

- [1] A. Slosar and J. A. Vazquez. <https://github.com/ja-vazquez/SimpleMC>
- [2] T. M. C. Abbott et al. First Cosmology Results using Type Ia Supernovae from the Dark Energy Survey: Constraints on Cosmological Parameters. *Astrophys. J. Lett.*, 872(2):L30, 2019.
- [3] G. Acquaviva, O. Akarsu, N. Katirci, and J. A. Vazquez. Simple-graduated dark energy and spatial curvature. *Phys. Rev. D*, 104(2):023505, 2021.
- [4] P. A. R. Ade et al. Planck 2015 results. XIII. Cosmological parameters. *Astron. Astrophys.*, 594:A13, 2016.
- [5] S. A. Adil, O. Akarsu, E. Di Valentino, R. C. Nunes, E. Ozulker, A. A. Sen, and E. Specogna. Omnipotent dark energy: A phenomenological answer to the Hubble tension. 6 2023.
- [6] N. Aghanim et al. Planck 2018 results. VI. Cosmological parameters. *Astron. Astrophys.*, 641:A6, 2020. [Erratum: *Astron. Astrophys.* 652, C4 (2021)].
- [7] P. Agrawal, G. Obied, P. J. Steinhardt, and C. Vafa. On the Cosmological Implications of the String Swampland. *Phys. Lett. B*, 784:271–276, 2018.
- [8] C. P. Ahn, R. Alexandroff, C. A. Prieto, S. F. Anderson, T. Anderton, B. H. Andrews, É. Aubourg, S. Bailey, E. Balbinot, R. Barnes, et al. The ninth data release of the sloan digital sky survey: first spectroscopic data from the sdss-iii baryon oscillation spectroscopic survey. *The Astrophysical Journal Supplement Series*, 203(2):21, 2012.

- [9] O. Akarsu, J. D. Barrow, C. V. R. Board, N. M. Uzun, and J. A. Vazquez. Screening  $\Lambda$  in a new modified gravity model. Eur. Phys. J. C, 79(10):846, 2019.
- [10] Ö. Akarsu, J. D. Barrow, L. A. Escamilla, and J. A. Vazquez. Graduated dark energy: Observational hints of a spontaneous sign switch in the cosmological constant. Physical Review D, 101(6):063528, 2020.
- [11] O. Akarsu, J. D. Barrow, L. A. Escamilla, and J. A. Vazquez. Graduated dark energy: Observational hints of a spontaneous sign switch in the cosmological constant. Phys. Rev. D, 101(6):063528, 2020.
- [12] O. Akarsu, E. O. Colgain, E. Özulker, S. Thakur, and L. Yin. The inevitable manifestation of wiggles in the expansion of the late universe. 7 2022.
- [13] O. Akarsu and T. Dereli. Late Time Acceleration of the 3-Space in a Higher Dimensional Steady State Universe in Dilaton Gravity. JCAP, 02:050, 2013.
- [14] O. Akarsu, E. Di Valentino, S. Kumar, R. C. Nunes, J. A. Vazquez, and A. Yadav.  $\Lambda_s$ CDM model: A promising scenario for alleviation of cosmological tensions. 7 2023.
- [15] O. Akarsu, N. Katirci, and S. Kumar. Cosmic acceleration in a dust only universe via energy-momentum powered gravity. Phys. Rev. D, 97(2):024011, 2018.
- [16] O. Akarsu, N. Katirci, A. A. Sen, and J. A. Vazquez. Scalar field emulator via anisotropically deformed vacuum energy: Application to dark energy. 4 2020.
- [17] O. Akarsu, S. Kumar, E. Özulker, and J. A. Vazquez. Relaxing cosmological tensions with a sign switching cosmological constant. Phys. Rev. D, 104(12):123512, 2021.
- [18] O. Akarsu, S. Kumar, E. Özulker, J. A. Vazquez, and A. Yadav. Relaxing cosmological tensions with a sign switching cosmological constant: Improved results with Planck, BAO and Pantheon data. 11 2022.
- [19] Y. Akrami, R. Kallosh, A. Linde, and V. Vardanyan. The Landscape, the Swampland and the Era of Precision Cosmology. Fortsch. Phys., 67(1-2):1800075, 2019.
- [20] S. Alam, M. Ata, S. Bailey, F. Beutler, D. Bizyaev, J. A. Blazek, A. S. Bolton, J. R. Brownstein, A. Burden, C.-H. Chuang, et al. The clustering of galaxies in the completed sdss-iii baryon oscillation spectroscopic survey: cosmological analysis of the dr12 galaxy sample. Monthly Notices of the Royal Astronomical Society, 470(3):2617–2652, 2017.

- [21] S. Alam et al. Completed SDSS-IV extended Baryon Oscillation Spectroscopic Survey: Cosmological implications from two decades of spectroscopic surveys at the Apache Point Observatory. Phys. Rev. D, 103(8):083533, 2021.
- [22] M. Aljaf, D. Gregoris, and M. Khurshudyan. Constraints on interacting dark energy models through cosmic chronometers and gaussian process. arXiv preprint arXiv:2005.01891, 2020.
- [23] M. Aljaf, D. Gregoris, and M. Khurshudyan. Constraints on interacting dark energy models through cosmic chronometers and Gaussian process. Eur. Phys. J. C, 81(6):544, 2021.
- [24] S. W. Allen, D. A. Rapetti, R. W. Schmidt, H. Ebeling, G. Morris, and A. C. Fabian. Improved constraints on dark energy from Chandra X-ray observations of the largest relaxed galaxy clusters. Mon. Not. Roy. Astron. Soc., 383:879–896, 2008.
- [25] R. An, C. Feng, and B. Wang. Relieving the Tension between Weak Lensing and Cosmic Microwave Background with Interacting Dark Matter and Dark Energy Models. JCAP, 02:038, 2018.
- [26] L. Anderson, E. Aubourg, S. Bailey, F. Beutler, V. Bhardwaj, M. Blanton, A. S. Bolton, J. Brinkmann, J. R. Brownstein, A. Burden, et al. The clustering of galaxies in the sdss-iii baryon oscillation spectroscopic survey: baryon acoustic oscillations in the data releases 10 and 11 galaxy samples. Monthly Notices of the Royal Astronomical Society, 441(1):24–62, 2014.
- [27] L. Anderson et al. The clustering of galaxies in the SDSS-III Baryon Oscillation Spectroscopic Survey: baryon acoustic oscillations in the Data Releases 10 and 11 Galaxy samples. Mon. Not. Roy. Astron. Soc., 441(1):24–62, 2014.
- [28] D. Andriot. On the de Sitter swampland criterion. Phys. Lett. B, 785:570–573, 2018.
- [29] A. Ashtekar, T. Pawłowski, and P. Singh. Quantum Nature of the Big Bang: Improved dynamics. Phys. Rev. D, 74:084003, 2006.
- [30] A. Ashtekar and P. Singh. Loop Quantum Cosmology: A Status Report. Class. Quant. Grav., 28:213001, 2011.
- [31] G. Aslanyan, L. C. Price, K. N. Abazajian, and R. Easther. The knotted sky i: Planck constraints on the primordial power spectrum. Journal of Cosmology and Astroparticle Physics, 2014(08):052, 2014.

- [32] M. Ata, F. Baumgarten, J. Bautista, F. Beutler, D. Bizyaev, M. R. Blanton, J. A. Blazek, A. S. Bolton, J. Brinkmann, J. R. Brownstein, et al. The clustering of the sdss-iv extended baryon oscillation spectroscopic survey dr14 quasar sample: first measurement of baryon acoustic oscillations between redshift 0.8 and 2.2. Monthly Notices of the Royal Astronomical Society, 473(4):4773–4794, 2018.
- [33] É. Aubourg, S. Bailey, J. E. Bautista, F. Beutler, V. Bhardwaj, D. Bizyaev, M. Blanton, M. Blomqvist, A. S. Bolton, J. Bovy, et al. Cosmological implications of baryon acoustic oscillation measurements. Physical Review D, 92(12):123516, 2015.
- [34] E. Aubourg et al. Cosmological implications of baryon acoustic oscillation measurements. Phys. Rev. D, 92(12):123516, 2015.
- [35] A. Banihashemi, N. Khosravi, and A. H. Shirazi. Ginzburg-Landau Theory of Dark Energy: A Framework to Study Both Temporal and Spatial Cosmological Tensions Simultaneously. Phys. Rev. D, 99(8):083509, 2019.
- [36] A. Banihashemi, N. Khosravi, and A. H. Shirazi. Phase transition in the dark sector as a proposal to lessen cosmological tensions. Phys. Rev. D, 101(12):123521, 2020.
- [37] J. D. Barrow. GRADUATED INFLATIONARY UNIVERSES. Phys. Lett. B, 235:40–43, 1990.
- [38] J. D. Barrow and K.-i. Maeda. Extended inflationary universes. Nucl. Phys. B, 341:294–308, 1990.
- [39] J. D. Barrow and P. Saich. The Behavior of intermediate inflationary universes. Phys. Lett. B, 249:406–410, 1990.
- [40] S. Basilakos et al. Dark energy reconstruction based on the padé approximation; an expansion around the  $\bar{\Lambda}$ cdm. The European Physical Journal C, 78(11):889, 2018.
- [41] F. Bauer, J. Sola, and H. Stefancic. Dynamically avoiding fine-tuning the cosmological constant: The ‘Relaxed Universe’. JCAP, 12:029, 2010.
- [42] C. Bernal, V. H. Cardenas, and V. Motta. Asymmetry in the reconstructed deceleration parameter. Phys. Lett. B, 765:163–170, 2017.
- [43] A. Bernui, E. Di Valentino, W. Giarè, S. Kumar, and R. C. Nunes. Solution of  $H_0$  tension with evidence of dark sector interaction from 2D BAO measurements. 1 2023.

- [44] F. Beutler, C. Blake, M. Colless, D. H. Jones, L. Staveley-Smith, L. Campbell, Q. Parker, W. Saunders, and F. Watson. The 6df galaxy survey: baryon acoustic oscillations and the local hubble constant. Monthly Notices of the Royal Astronomical Society, 416(4):3017–3032, 2011.
- [45] M. Blomqvist, H. d. M. d. Bourboux, N. G. Busca, V. d. S. Agathe, J. Rich, C. Balland, J. E. Bautista, K. Dawson, A. Font-Ribera, J. Guy, et al. Baryon acoustic oscillations from the cross-correlation of lyman- $\alpha$  absorption and quasars in eboss dr14. arXiv preprint arXiv:1904.03430, 2019.
- [46] C. V. R. Board and J. D. Barrow. Cosmological Models in Energy-Momentum-Squared Gravity. Phys. Rev. D, 96(12):123517, 2017. [Erratum: Phys.Rev.D 98, 129902 (2018)].
- [47] B. Boisseau, G. Esposito-Farese, D. Polarski, and A. A. Starobinsky. Reconstruction of a scalar tensor theory of gravity in an accelerating universe. Phys. Rev. Lett., 85:2236, 2000.
- [48] Y. L. Bolotin, A. Kostenko, O. A. Lemets, and D. A. Yerokhin. Cosmological Evolution With Interaction Between Dark Energy And Dark Matter. Int. J. Mod. Phys. D, 24(03):1530007, 2014.
- [49] A. Bonilla, S. Kumar, and R. C. Nunes. Measurements of  $H_0$  and reconstruction of the dark energy properties from a model-independent joint analysis. Eur. Phys. J. C, 81(2):127, 2021.
- [50] A. Bonilla, S. Kumar, R. C. Nunes, and S. Pan. Reconstruction of the dark sectors’ interaction: A model-independent inference and forecast from GW standard sirens. Mon. Not. Roy. Astron. Soc., 512(3):4231–4238, 2022.
- [51] V. Bonvin and M. Millon. H0licow h0 tension plotting notebook, Feb. 2020.
- [52] A. Bouali, I. Albarran, M. Bouhmadi-López, and T. Ouali. Cosmological constraints of phantom dark energy models. Phys. Dark Univ., 26:100391, 2019.
- [53] M. Bouhmadi-Lopez, A. Errahmani, P. Martin-Moruno, T. Ouali, and Y. Tavakoli. The little sibling of the big rip singularity. Int. J. Mod. Phys. D, 24(10):1550078, 2015.
- [54] P. Brax and J. Martin. The SUGRA Quintessence Model Coupled to the MSSM. JCAP, 11:008, 2006.

- [55] P. Brax and C. van de Bruck. Cosmology and brane worlds: A Review. Class. Quant. Grav., 20:R201–R232, 2003.
- [56] P. Brax, C. van de Bruck, and A.-C. Davis. Brane world cosmology. Reports on Progress in Physics, 67(12):2183, 2004.
- [57] P. Bull, Y. Akrami, J. Adamek, T. Baker, E. Bellini, J. B. Jimenez, E. Bentivegna, S. Camera, S. Clesse, J. H. Davis, et al. Beyond  $\lambda$ cdm: Problems, solutions, and the road ahead. Physics of the Dark Universe, 12:56–99, 2016.
- [58] R.-G. Cai and Q. Su. On the Dark Sector Interactions. Phys. Rev. D, 81:103514, 2010.
- [59] R.-G. Cai and A. Wang. Cosmology with interaction between phantom dark energy and dark matter and the coincidence problem. JCAP, 03:002, 2005.
- [60] R. Caldwell and E. V. Linder. Limits of quintessence. Physical review letters, 95(14):141301, 2005.
- [61] R. R. Caldwell. A phantom menace? cosmological consequences of a dark energy component with super-negative equation of state. Physics Letters B, 545(1-2):23–29, 2002.
- [62] R. R. Caldwell and M. Kamionkowski. The Physics of Cosmic Acceleration. Ann. Rev. Nucl. Part. Sci., 59:397–429, 2009.
- [63] S. Capozziello and M. De Laurentis. Extended Theories of Gravity. Phys. Rept., 509:167–321, 2011.
- [64] S. Capozziello, Ruchika, and A. A. Sen. Model independent constraints on dark energy evolution from low-redshift observations. Mon. Not. Roy. Astron. Soc., 484:4484, 2019.
- [65] S. M. Carroll, M. Hoffman, and M. Trodden. Can the dark energy equation-of-state parameter  $w$  be less than 1? Phys. Rev. D, 68:023509, 2003.
- [66] X. Chen, G. Shiu, Y. Sumitomo, and S. H. H. Tye. A Global View on The Search for de-Sitter Vacua in (type IIA) String Theory. JHEP, 04:026, 2012.
- [67] M. Chevallier and D. Polarski. Accelerating universes with scaling dark matter. International Journal of Modern Physics D, 10(02):213–223, 2001.
- [68] M. Chevallier and D. Polarski. Accelerating universes with scaling dark matter. Int. J. Mod. Phys. D, 10:213–224, 2001.

- [69] A. Chodos and S. L. Detweiler. Where Has the Fifth-Dimension Gone? Phys. Rev. D, 21:2167, 1980.
- [70] M. Cicoli, S. De Alwis, A. Maharana, F. Muia, and F. Quevedo. De Sitter vs Quintessence in String Theory. Fortsch. Phys., 67(1-2):1800079, 2019.
- [71] T. Clifton, P. G. Ferreira, A. Padilla, and C. Skordis. Modified Gravity and Cosmology. Phys. Rept., 513:1–189, 2012.
- [72] E. O. Colgáin, M. M. Sheikh-Jabbari, R. Solomon, M. G. Dainotti, and D. Stojkovic. Putting Flat  $\Lambda$ CDM In The (Redshift) Bin. 6 2022.
- [73] E. O. Colgáin, M. M. Sheikh-Jabbari, and L. Yin. Can dark energy be dynamical? Phys. Rev. D, 104(2):023510, 2021.
- [74] E. O. Colgáin and H. Yavartanoo. Testing the Swampland:  $H_0$  tension. Phys. Lett. B, 797:134907, 2019.
- [75] P. Collaboration, Y. Akrami, M. Ashdown, J. Aumont, C. Baccigalupi, M. Ballardini, A. Banday, R. Barreiro, N. Bartolo, S. Basak, et al. Planck 2018 results. vii. isotropy and statistics of the cmb. Astronomy & Astrophysics, 2019.
- [76] R. Cooke, M. Pettini, R. A. Jorgenson, M. T. Murphy, and C. C. Steidel. Precision measures of the primordial abundance of deuterium. Astrophys. J., 781(1):31, 2014.
- [77] E. J. Copeland, M. Sami, and S. Tsujikawa. Dynamics of dark energy. Int. J. Mod. Phys. D, 15:1753–1936, 2006.
- [78] R. G. Crittenden, L. Pogosian, and G.-B. Zhao. Investigating dark energy experiments with principal components. JCAP, 12:025, 2009.
- [79] R. G. Crittenden, G.-B. Zhao, L. Pogosian, L. Samushia, and X. Zhang. Fables of reconstruction: controlling bias in the dark energy equation of state. Journal of Cosmology and Astroparticle Physics, 2012(02):048, 2012.
- [80] A. Cuceu, J. Farr, P. Lemos, and A. Font-Ribera. Baryon Acoustic Oscillations and the Hubble Constant: Past, Present and Future. JCAP, 10:044, 2019.
- [81] U. H. Danielsson, S. S. Haque, P. Koerber, G. Shiu, T. Van Riet, and T. Wrase. De Sitter hunting in a classical landscape. Fortsch. Phys., 59:897–933, 2011.

- [82] U. H. Danielsson, S. S. Haque, G. Shiu, and T. Van Riet. Towards Classical de Sitter Solutions in String Theory. JHEP, 09:114, 2009.
- [83] U. H. Danielsson, P. Koerber, and T. Van Riet. Universal de Sitter solutions at tree-level. JHEP, 05:090, 2010.
- [84] U. H. Danielsson, G. Shiu, T. Van Riet, and T. Wrase. A note on obstinate tachyons in classical dS solutions. JHEP, 03:138, 2013.
- [85] U. H. Danielsson and T. Van Riet. What if string theory has no de Sitter vacua? Int. J. Mod. Phys. D, 27(12):1830007, 2018.
- [86] K. Dasgupta, R. Gwyn, E. McDonough, M. Mia, and R. Tatar. de Sitter Vacua in Type IIB String Theory: Classical Solutions and Quantum Corrections. JHEP, 07:054, 2014.
- [87] A. De Felice and S. Tsujikawa. f(R) theories. Living Rev. Rel., 13:3, 2010.
- [88] V. de Sainte Agathe, C. Balland, H. du Mas des Bourboux, M. Blomqvist, J. Guy, J. Rich, A. Font-Ribera, M. M. Pieri, J. E. Bautista, K. Dawson, et al. Baryon acoustic oscillations at  $z=2.34$  from the correlations of Ly  $\alpha$  absorption in eboss dr14. Astronomy and Astrophysics, 629(BNL-212173-2019-JAAM), 2019.
- [89] S. del Campo, R. Herrera, and D. Pavon. Interacting models may be key to solve the cosmic coincidence problem. JCAP, 01:020, 2009.
- [90] T. Delubac et al. Baryon acoustic oscillations in the Ly $\alpha$  forest of BOSS DR11 quasars. Astron. Astrophys., 574:A59, 2015.
- [91] T. Dereli and R. W. Tucker. Dynamical Reduction of Internal Dimensions in the Early Universe. Phys. Lett. B, 125:133–135, 1983.
- [92] E. Di Valentino, A. Melchiorri, and O. Mena. Can interacting dark energy solve the  $H_0$  tension? Phys. Rev. D, 96(4):043503, 2017.
- [93] E. Di Valentino, A. Melchiorri, O. Mena, and S. Vagnozzi. Interacting dark energy in the early 2020s: A promising solution to the  $H_0$  and cosmic shear tensions. Phys. Dark Univ., 30:100666, 2020.
- [94] E. Di Valentino, A. Melchiorri, O. Mena, and S. Vagnozzi. Nonminimal dark sector physics and cosmological tensions. Phys. Rev. D, 101(6):063502, 2020.



- [95] S. Dodelson. Modern cosmology. Elsevier, 2003.
- [96] A. D. Dolgov. FIELD MODEL WITH A DYNAMIC CANCELLATION OF THE COSMOLOGICAL CONSTANT. JETP Lett., 41:345–347, 1985.
- [97] K. Dutta, Ruchika, A. Roy, A. A. Sen, and M. M. Sheikh-Jabbari. Beyond  $\Lambda$ CDM with low and high redshift data: implications for dark energy. Gen. Rel. Grav., 52(2):15, 2020.
- [98] B. Efron, A. Gous, R. Kass, G. Datta, and P. Lahiri. Scales of evidence for model selection: Fisher versus jeffreys. Lecture Notes-Monograph Series, pages 208–256, 2001.
- [99] D. J. Eisenstein. Dark energy and cosmic sound. New Astron. Rev., 49(7-9):360–365, 2005.
- [100] D. J. Eisenstein et al. Detection of the Baryon Acoustic Peak in the Large-Scale Correlation Function of SDSS Luminous Red Galaxies. Astrophys. J., 633:560–574, 2005.
- [101] G. F. R. Ellis and H. van Elst. Cosmological models: Cargese lectures 1998. NATO Sci. Ser. C, 541:1–116, 1999.
- [102] L. A. Escamilla and J. A. Vazquez. Model selection applied to reconstructions of the Dark Energy. Eur. Phys. J. C, 83(3):251, 2023.
- [103] J. Espejo, S. Peirone, M. Raveri, K. Koyama, L. Pogosian, and A. Silvestri. Phenomenology of Large Scale Structure in scalar-tensor theories: joint prior covariance of  $w_{\text{DE}}$ ,  $\Sigma$  and  $\mu$  in Horndeski. Phys. Rev. D, 99(2):023512, 2019.
- [104] J. Evslin. Isolating the Lyman Alpha Forest BAO Anomaly. JCAP, 04:024, 2017.
- [105] J. M. Ezquiaga and M. Zumalacárregui. Dark energy in light of multi-messenger gravitational-wave astronomy. Frontiers in Astronomy and Space Sciences, 5:44, 2018.
- [106] D. J. Fixsen. The Temperature of the Cosmic Microwave Background. Astrophys. J., 707:916–920, 2009.
- [107] P. H. Frampton, K. J. Ludwick, and R. J. Scherrer. The Little Rip. Phys. Rev. D, 84:063003, 2011.
- [108] S. A. Franchino-Viñas and S. Mignemi. Asymptotic freedom for  $\lambda\phi^4$  QFT in Snyder–de Sitter space. Eur. Phys. J. C, 80(5):382, 2020.
- [109] W. L. Freedman et al. The Carnegie-Chicago Hubble Program. VIII. An Independent Determination of the Hubble Constant Based on the Tip of the Red Giant Branch. Astrophys. J., 882:34, 2019.

- [110] S. K. Garg and C. Krishnan. Bounds on Slow Roll and the de Sitter Swampland. JHEP, 11:075, 2019.
- [111] F. Gerardi, M. Martinelli, and A. Silvestri. Reconstruction of the dark energy equation of state from latest data: the impact of theoretical priors. Journal of Cosmology and Astroparticle Physics, 2019(07):042, 2019.
- [112] F. Gerardi, M. Martinelli, and A. Silvestri. Reconstruction of the Dark Energy equation of state from latest data: the impact of theoretical priors. JCAP, 07:042, 2019.
- [113] M. M. G.F.R. Ellis, R. Maartens. Relativistic Cosmology. Cambridge University Press, 2012.
- [114] A. Gómez-Valent and L. Amendola.  $H_0$  from cosmic chronometers and type ia supernovae, with gaussian processes and the novel weighted polynomial regression method. Journal of Cosmology and Astroparticle Physics, 2018(04):051, 2018.
- [115] A. Gómez-Valent and L. Amendola.  $H_0$  from cosmic chronometers and Type Ia supernovae, with Gaussian Processes and the novel Weighted Polynomial Regression method. JCAP, 04:051, 2018.
- [116] A. Gomez-Valent, E. Karimkhani, and J. Sola. Background history and cosmic perturbations for a general system of self-conserved dynamical dark energy and matter. JCAP, 12:048, 2015.
- [117] A. Gómez-Valent, V. Pettorino, and L. Amendola. Update on coupled dark energy and the  $H_0$  tension. Phys. Rev. D, 101(12):123513, 2020.
- [118] I. Gómez-Vargas, R. M. Esquivel, R. García-Salcedo, and J. A. Vázquez. Neural network reconstructions for the Hubble parameter, growth rate and distance modulus. Eur. Phys. J. C, 83(4):304, 2023.
- [119] Y.-G. Gong and A. Wang. Reconstruction of the deceleration parameter and the equation of state of dark energy. Phys. Rev. D, 75:043520, 2007.
- [120] T. Gonzalez, T. Matos, I. Quiros, and A. Vazquez-Gonzalez. Self-interacting Scalar Field Trapped in a Randall-Sundrum Braneworld: The Dynamical Systems Perspective. Phys. Lett. B, 676:161–167, 2009.

- [121] J.-J. Guo, J.-F. Zhang, Y.-H. Li, D.-Z. He, and X. Zhang. Probing the sign-changeable interaction between dark energy and dark matter with current observations. Sci. China Phys. Mech. Astron., 61(3):030011, 2018.
- [122] Z.-K. Guo, Y.-S. Piao, X. Zhang, and Y.-Z. Zhang. Cosmological evolution of a quintom model of dark energy. Physics Letters B, 608(3-4):177–182, 2005.
- [123] F. S. Guzman, T. Matos, and H. Villegas. Scalar fields as dark matter in spiral galaxies: comparison with experiments. Astronomische Nachrichten: News in Astronomy and Astrophysics, 320(3):97–104, 1999.
- [124] C. Han, S. Pi, and M. Sasaki. Quintessence Saves Higgs Instability. Phys. Lett. B, 791:314–318, 2019.
- [125] W. Handley. fgivenx: A python package for functional posterior plotting. arXiv preprint arXiv:1908.01711, 2019.
- [126] W. Handley. Curvature tension: evidence for a closed universe. Phys. Rev. D, 103(4):L041301, 2021.
- [127] W. J. Handley, A. N. Lasenby, H. V. Peiris, and M. P. Hobson. Bayesian inflationary reconstructions from planck 2018 data. arXiv preprint arXiv:1908.00906, 2019.
- [128] S. Hee, J. Vázquez, W. Handley, M. Hobson, and A. Lasenby. Constraining the dark energy equation of state using bayes theorem and the kullback–leibler divergence. Monthly Notices of the Royal Astronomical Society, 466(1):369–377, 2017.
- [129] L. Heisenberg, M. Bartelmann, R. Brandenberger, and A. Refregier. Dark Energy in the Swampland. Phys. Rev. D, 98(12):123502, 2018.
- [130] A. Hernández-Almada, G. Leon, J. Magaña, M. A. García-Aspeitia, and V. Motta. Generalized Emergent Dark Energy: observational Hubble data constraints and stability analysis. Mon. Not. Roy. Astron. Soc., 497(2):1590–1602, 2020.
- [131] T. Holsclaw, U. Alam, B. Sanso, H. Lee, K. Heitmann, S. Habib, and D. Higdon. Non-parametric dark energy reconstruction from supernova data. Physical Review Letters, 105(24):241302, 2010.
- [132] T. Holsclaw, B. Sansó, H. K. Lee, K. Heitmann, S. Habib, D. Higdon, and U. Alam. Gaussian process modeling of derivative curves. Technometrics, 55(1):57–67, 2013.

- [133] D. Ida. Brane-world cosmology. Journal of High Energy Physics, 2000(09):014, 2000.
- [134] J. Speagle. <https://dynesty.readthedocs.io/en/stable/index.html>.
- [135] R. Jimenez, L. Verde, T. Treu, and D. Stern. Constraints on the equation of state of dark energy and the hubble constant from stellar ages and the cosmic microwave background. The Astrophysical Journal, 593(2):622, 2003.
- [136] Jones et. al. and Scolnic et. al. <https://archive.stsci.edu/prepds/ps1cosmo/>.
- [137] S. Kachru, R. Kallosh, A. D. Linde, and S. P. Trivedi. De Sitter vacua in string theory. Phys. Rev. D, 68:046005, 2003.
- [138] R. E. Keeley and A. Shafieloo. On the distribution of Bayesian evidence. Mon. Not. Roy. Astron. Soc., 515(1):293–301, 2022.
- [139] R. E. Keeley, A. Shafieloo, G.-B. Zhao, J. A. Vazquez, and H. Koo. Reconstructing the Universe: Testing the Mutual Consistency of the Pantheon and SDSS/eBOSS BAO Data Sets with Gaussian Processes. Astron. J., 161(3):151, 2021.
- [140] W. H. Kinney. Eternal Inflation and the Refined Swampland Conjecture. Phys. Rev. Lett., 122(8):081302, 2019.
- [141] W. H. Kinney, S. Vagnozzi, and L. Visinelli. The zoo plot meets the swampland: mutual (in)consistency of single-field inflation, string conjectures, and cosmological data. Class. Quant. Grav., 36(11):117001, 2019.
- [142] G. Kofinas, E. Papantonopoulos, and E. N. Saridakis. Modified Brans–Dicke cosmology with matter-scalar field interaction. Class. Quant. Grav., 33(15):155004, 2016.
- [143] M. Kopp, C. Skordis, D. B. Thomas, and S. Ilić. Dark Matter Equation of State through Cosmic History. Phys. Rev. Lett., 120(22):221102, 2018.
- [144] P. Kroupa. The dark matter crisis: problems with the current standard model of cosmology and steps towards an improved model. pdmg, 1:40001, 2013.
- [145] S. Kumar and R. C. Nunes. Echo of interactions in the dark sector. Phys. Rev. D, 96(10):103511, 2017.
- [146] S. Kumar, R. C. Nunes, and S. K. Yadav. Dark sector interaction: a remedy of the tensions between CMB and LSS data. Eur. Phys. J. C, 79(7):576, 2019.

- [147] J.-w. Lee and I.-g. Koh. Galactic halos as boson stars. Phys. Rev. D, 53:2236–2239, 1996.
- [148] X. Li and A. Shafieloo. Evidence for Emergent Dark Energy. Astrophys. J., 902(1):58, 2020.
- [149] Y.-H. Li and X. Zhang. Running coupling: Does the coupling between dark energy and dark matter change sign during the cosmological evolution? Eur. Phys. J. C, 71:1700, 2011.
- [150] M. Lucca and D. C. Hooper. Shedding light on dark matter-dark energy interactions. Phys. Rev. D, 102(12):123502, 2020.
- [151] M. Moresco. <https://gitlab.com/mmoresco/CCcovariance>.
- [152] J. M. Maldacena. The Large N limit of superconformal field theories and supergravity. Adv. Theor. Math. Phys., 2:231–252, 1998.
- [153] J. M. Maldacena and C. Nunez. Supergravity description of field theories on curved manifolds and a no go theorem. Int. J. Mod. Phys. A, 16:822–855, 2001.
- [154] A. A. Mamon and S. Das. A parametric reconstruction of the deceleration parameter. Eur. Phys. J. C, 77(7):495, 2017.
- [155] M. Marciu. Quintom dark energy with nonminimal coupling. Phys. Rev. D, 93(12):123006, 2016.
- [156] T. Matos, A. Vazquez-Gonzalez, and J. Magana.  $\phi^2$  as Dark Matter. Mon. Not. Roy. Astron. Soc., 393:1359–1369, 2009.
- [157] A. Montiel, R. Lazkoz, I. Sendra, C. Escamilla-Rivera, and V. Salzano. Nonparametric reconstruction of the cosmic expansion with local regression smoothing and simulation extrapolation. Phys. Rev. D, 89(4):043007, 2014.
- [158] M. Moresco. Raising the bar: new constraints on the hubble parameter with cosmic chronometers at  $z \sim 2$ . Monthly Notices of the Royal Astronomical Society: Letters, 450(1):L16–L20, 2015.
- [159] M. Moresco, L. Pozzetti, A. Cimatti, R. Jimenez, C. Maraston, L. Verde, D. Thomas, A. Citro, R. Tojeiro, and D. Wilkinson. A 6% measurement of the hubble parameter at  $z \sim 0.45$ : direct evidence of the epoch of cosmic re-acceleration. Journal of Cosmology and Astroparticle Physics, 2016(05):014, 2016.

- [160] M. Moresco, L. Verde, L. Pozzetti, R. Jimenez, and A. Cimatti. New constraints on cosmological parameters and neutrino properties using the expansion rate of the universe to  $z = 1.75$ . Journal of Cosmology and Astroparticle Physics, 2012(07):053, 2012.
- [161] E. Mörtzell and S. Dhawan. Does the Hubble constant tension call for new physics? JCAP, 09:025, 2018.
- [162] E. Mörtzell and S. Dhawan. Does the hubble constant tension call for new physics? Journal of Cosmology and Astroparticle Physics, 2018(09):025, 2018.
- [163] A. Mukherjee. Kinematical models of late-time cosmology and the statefinder diagnostic. Eur. Phys. J. Plus, 136(3):300, 2021.
- [164] A. Mukherjee and N. Banerjee. Parametric reconstruction of the cosmological jerk from diverse observational data sets. Phys. Rev. D, 93(4):043002, 2016.
- [165] P. Mukherjee and N. Banerjee. Nonparametric reconstruction of interaction in the cosmic dark sector. Phys. Rev. D, 103(12):123530, 2021.
- [166] H. Murayama, M. Yamazaki, and T. T. Yanagida. Do We Live in the Swampland? JHEP, 12:032, 2018.
- [167] K. Naidoo, M. Jaber, W. A. Hellwing, and M. Bilicki. A dark matter solution to the  $H_0$  and  $S_8$  tensions, and the integrated Sachs-Wolfe void anomaly. 9 2022.
- [168] A. Navarro-Bouloosa, A. Bernal, and J. A. Vazquez. Bayesian analysis for rotational curves with  $\ell$ -boson stars as a dark matter component. JCAP, 09:031, 2023.
- [169] S. Nesseris and J. Garcia-Bellido. Is the Jeffreys' scale a reliable tool for Bayesian model comparison in cosmology? JCAP, 08:036, 2013.
- [170] S. Nojiri and S. D. Odintsov. The Final state and thermodynamics of dark energy universe. Phys. Rev. D, 70:103522, 2004.
- [171] S. Nojiri and S. D. Odintsov. Introduction to modified gravity and gravitational alternative for dark energy. International Journal of Geometric Methods in Modern Physics, 4(01):115–145, 2007.
- [172] S. Nojiri and S. D. Odintsov. Unified cosmic history in modified gravity: from  $f(r)$  theory to lorentz non-invariant models. Physics Reports, 505(2-4):59–144, 2011.

- [173] S. Nojiri and S. D. Odintsov. Unified cosmic history in modified gravity: from F(R) theory to Lorentz non-invariant models. Phys. Rept., 505:59–144, 2011.
- [174] S. Nojiri, S. D. Odintsov, and V. K. Oikonomou. Modified Gravity Theories on a Nutshell: Inflation, Bounce and Late-time Evolution. Phys. Rept., 692:1–104, 2017.
- [175] R. C. Nunes and E. Di Valentino. Dark sector interaction and the supernova absolute magnitude tension. Phys. Rev. D, 104(6):063529, 2021.
- [176] R. C. Nunes, S. Vagnozzi, S. Kumar, E. Di Valentino, and O. Mena. New tests of dark sector interactions from the full-shape galaxy power spectrum. Phys. Rev. D, 105(12):123506, 2022.
- [177] E. Ó Colgáin, M. H. P. M. van Putten, and H. Yavartanoo. de Sitter Swampland,  $H_0$  tension & observation. Phys. Lett. B, 793:126–129, 2019.
- [178] G. Obied, H. Ooguri, L. Spodyneiko, and C. Vafa. De Sitter Space and the Swampland. 6 2018.
- [179] G. Olivares, F. Atrio-Barandela, and D. Pavon. Dynamics of Interacting Quintessence Models: Observational Constraints. Phys. Rev. D, 77:063513, 2008.
- [180] H. Ooguri, E. Palti, G. Shiu, and C. Vafa. Distance and de Sitter Conjectures on the Swampland. Phys. Lett. B, 788:180–184, 2019.
- [181] E. Ozulker. Is the dark energy equation of state parameter singular? Phys. Rev. D, 106(6):063509, 2022.
- [182] L. E. Padilla, L. O. Tellez, L. A. Escamilla, and J. A. Vazquez. Cosmological Parameter Inference with Bayesian Statistics. Universe, 7(7):213, 2021.
- [183] L. E. Padilla, J. A. Vázquez, T. Matos, and G. Germán. Scalar Field Dark Matter Spectator During Inflation: The Effect of Self-interaction. JCAP, 05:056, 2019.
- [184] E. Palti. The Swampland: Introduction and Review. Fortsch. Phys., 67(6):1900037, 2019.
- [185] S. Pan, G. S. Sharov, and W. Yang. Field theoretic interpretations of interacting dark energy scenarios and recent observations. Phys. Rev. D, 101(10):103533, 2020.
- [186] S. Pan, W. Yang, E. Di Valentino, D. F. Mota, and J. Silk. IWDM: the fate of an interacting non-cold dark matter — vacuum scenario. JCAP, 07:064, 2023.

- [187] S. Pan, W. Yang, E. Di Valentino, E. N. Saridakis, and S. Chakraborty. Interacting scenarios with dynamical dark energy: Observational constraints and alleviation of the  $H_0$  tension. Phys. Rev. D, 100(10):103520, 2019.
- [188] L. Pogosian, M. Raveri, K. Koyama, M. Martinelli, A. Silvestri, G.-B. Zhao, J. Li, S. Peirone, and A. Zucca. Imprints of cosmological tensions in reconstructed gravity. Nature Astron., 6(12):1484–1490, 2022.
- [189] D. Posada and T. R. Buckley. Model selection and model averaging in phylogenetics: advantages of akaike information criterion and bayesian approaches over likelihood ratio tests. Systematic biology, 53(5):793–808, 2004.
- [190] V. Poulin, K. K. Boddy, S. Bird, and M. Kamionkowski. Implications of an extended dark energy cosmology with massive neutrinos for cosmological tensions. Phys. Rev. D, 97(12):123504, 2018.
- [191] V. Poulin, T. L. Smith, D. Grin, T. Karwal, and M. Kamionkowski. Cosmological implications of ultralight axionlike fields. Phys. Rev. D, 98(8):083525, 2018.
- [192] V. Poulin, T. L. Smith, T. Karwal, and M. Kamionkowski. Early dark energy can resolve the hubble tension. Physical review letters, 122(22):221301, 2019.
- [193] A. Poursidou and T. Tram. Reconciling CMB and structure growth measurements with dark energy interactions. Phys. Rev. D, 94(4):043518, 2016.
- [194] J.-Z. Qi, S. Cao, M. Biesiada, T. Xu, Y. Wu, S. Zhang, and Z.-H. Zhu. What is parameterized  $om(z)$  diagnostics telling us in light of recent observations? arXiv preprint arXiv:1803.04109, 2018.
- [195] A. L. Ratsimbazafy, S. I. Loubser, S. M. Crawford, C. M. Cress, B. A. Bassett, R. C. Nichol, and P. Väisänen. Age-dating Luminous Red Galaxies observed with the Southern African Large Telescope. Mon. Not. Roy. Astron. Soc., 467(3):3239–3254, 2017.
- [196] M. Raveri, P. Bull, A. Silvestri, and L. Pogosian. Priors on the effective Dark Energy equation of state in scalar-tensor theories. Phys. Rev. D, 96(8):083509, 2017.
- [197] M. Raveri, L. Pogosian, M. Martinelli, K. Koyama, A. Silvestri, G.-B. Zhao, J. Li, S. Peirone, and A. Zucca. Principal reconstructed modes of dark energy and gravity. JCAP, 02:061, 2023.



- [198] A. G. Riess, S. Casertano, W. Yuan, L. M. Macri, and D. Scolnic. Large Magellanic Cloud Cepheid Standards Provide a 1% Foundation for the Determination of the Hubble Constant and Stronger Evidence for Physics beyond  $\Lambda$ CDM. *Astrophys. J.*, 876(1):85, 2019.
- [199] A. G. Riess et al. A 2.4% Determination of the Local Value of the Hubble Constant. *Astrophys. J.*, 826(1):56, 2016.
- [200] A. G. Riess et al. Milky Way Cepheid Standards for Measuring Cosmic Distances and Application to Gaia DR2: Implications for the Hubble Constant. *Astrophys. J.*, 861(2):126, 2018.
- [201] A. G. Riess, A. V. Filippenko, P. Challis, A. Clocchiatti, A. Diercks, P. M. Garnavich, R. L. Gilliland, C. J. Hogan, S. Jha, R. P. Kirshner, et al. Observational evidence from supernovae for an accelerating universe and a cosmological constant. *The Astronomical Journal*, 116(3):1009, 1998.
- [202] J. G. Russo and P. K. Townsend. Late-time Cosmic Acceleration from Compactification. *Class. Quant. Grav.*, 36(9):095008, 2019.
- [203] V. Sahni. The cosmological constant problem and quintessence. *Classical and Quantum Gravity*, 19(13):3435, 2002.
- [204] V. Sahni, A. Shafieloo, and A. A. Starobinsky. Two new diagnostics of dark energy. *Phys. Rev. D*, 78:103502, 2008.
- [205] V. Sahni, A. Shafieloo, and A. A. Starobinsky. Model independent evidence for dark energy evolution from Baryon Acoustic Oscillations. *Astrophys. J. Lett.*, 793(2):L40, 2014.
- [206] V. Sahni and Y. Shtanov. Brane world models of dark energy. *JCAP*, 11:014, 2003.
- [207] V. Sahni and A. Starobinsky. Reconstructing dark energy. *International Journal of Modern Physics D*, 15(12):2105–2132, 2006.
- [208] V. Sahni and A. Starobinsky. Reconstructing Dark Energy. *Int. J. Mod. Phys. D*, 15:2105–2132, 2006.
- [209] V. Salvatelli, N. Said, M. Bruni, A. Melchiorri, and D. Wands. Indications of a late-time interaction in the dark sector. *Phys. Rev. Lett.*, 113(18):181301, 2014.

- [210] D. Scolnic et al. The Pantheon+ Analysis: The Full Data Set and Light-curve Release. *Astrophys. J.*, 938(2):113, 2022.
- [211] D. M. Scolnic, D. Jones, A. Rest, Y. Pan, R. Chornock, R. Foley, M. Huber, R. Kessler, G. Narayan, A. Riess, et al. The complete light-curve sample of spectroscopically confirmed sne ia from pan-starrs1 and cosmological constraints from the combined pantheon sample. *The Astrophysical Journal*, 859(2):101, 2018.
- [212] D. Scott. The standard model of cosmology: A skeptic’s guide. arXiv preprint arXiv:1804.01318, 2018.
- [213] M. Seikel, C. Clarkson, and M. Smith. Reconstruction of dark energy and expansion dynamics using gaussian processes. *Journal of Cosmology and Astroparticle Physics*, 2012(06):036, 2012.
- [214] E. Silverstein. Simple de Sitter Solutions. *Phys. Rev. D*, 77:106006, 2008.
- [215] J. Simon, L. Verde, and R. Jimenez. Constraints on the redshift dependence of the dark energy potential. *Physical Review D*, 71(12):123001, 2005.
- [216] S.-J. Sin. Late-time phase transition and the galactic halo as a bose liquid. *Physical Review D*, 50(6):3650, 1994.
- [217] J. Skilling. Nested sampling. In *AIP Conference Proceedings*, volume 735, pages 395–405. American Institute of Physics, 2004.
- [218] F. C. Solano and U. Nucamendi. Reconstruction of the interaction term between dark matter and dark energy using SNe Ia, BAO, CMB,  $H(z)$  and X-ray gas mass fraction. 7 2012.
- [219] J. S. Speagle. dynesty: a dynamic nested sampling package for estimating bayesian posteriors and evidences. *Monthly Notices of the Royal Astronomical Society*, 493(3):3132–3158, 2020.
- [220] D. N. Spergel and P. J. Steinhardt. Observational evidence for selfinteracting cold dark matter. *Phys. Rev. Lett.*, 84:3760–3763.
- [221] H. Stefancic. Dark energy transition between quintessence and phantom regimes - An Equation of state analysis. *Phys. Rev. D*, 71:124036, 2005.

- [222] H. Stefancic. Expansion around the vacuum equation of state - Sudden future singularities and asymptotic behavior. Phys. Rev. D, 71:084024, 2005.
- [223] D. Stern, R. Jimenez, L. Verde, M. Kamionkowski, and S. A. Stanford. Cosmic chronometers: constraining the equation of state of dark energy. i:  $H(z)$  measurements. Journal of Cosmology and Astroparticle Physics, 2010(02):008, 2010.
- [224] C.-Y. Sun and R.-H. Yue. New Interaction between Dark Energy and Dark Matter Changes Sign during Cosmological Evolution. Phys. Rev. D, 85:043010, 2012.
- [225] N. Suzuki, D. Rubin, C. Lidman, G. Aldering, R. Amanullah, K. Barbary, L. Barrientos, J. Botyanszki, M. Brodwin, N. Connolly, et al. The hubble space telescope cluster supernova survey. v. improving the dark-energy constraints above  $z > 1$  and building an early-type-hosted supernova sample. The Astrophysical Journal, 746(1):85, 2012.
- [226] D. Tamayo and J. A. Vazquez. Fourier-series expansion of the dark-energy equation of state. Mon. Not. Roy. Astron. Soc., 487(1):729–736, 2019.
- [227] L. O. Téllez-Tovar, T. Matos, and J. A. Vázquez. Cosmological constraints on the multi-scalar field dark matter model. Phys. Rev. D, 106(12):123501, 2022.
- [228] R. Trotta. Bayes in the sky: Bayesian inference and model selection in cosmology. Contemporary Physics, 49(2):71–104, 2008.
- [229] C. Vafa. The String landscape and the swampland. 9 2005.
- [230] J. A. Vazquez, M. Bridges, M. Hobson, and A. Lasenby. Model selection applied to reconstruction of the primordial power spectrum. Journal of Cosmology and Astroparticle Physics, 2012(06):006, 2012.
- [231] J. A. Vazquez, M. Bridges, M. Hobson, and A. Lasenby. Reconstruction of the dark energy equation of state. Journal of Cosmology and Astroparticle Physics, 2012(09):020, 2012.
- [232] J. A. Vázquez, D. Tamayo, G. Garcia-Arroyo, I. Gómez-Vargas, I. Quiros, and A. A. Sen. Coupled Multi Scalar Field Dark Energy. 5 2023.
- [233] A. Velásquez-Toribio and J. C. Fabris. The growth factor parametrization versus numerical solutions in flat and non-flat dark energy models. arXiv preprint arXiv:2008.12741, 2020.
- [234] L. Visinelli, S. Vagnozzi, and U. Danielsson. Revisiting a negative cosmological constant from low-redshift data. Symmetry, 11(8):1035, 2019.

- [235] L. Visinelli, S. Vagnozzi, and U. Danielsson. Revisiting a negative cosmological constant from low-redshift data. Symmetry, 11(8):1035, 2019.
- [236] R. von Marttens, J. E. Gonzalez, J. Alcaniz, V. Marra, and L. Casarini. Model-independent reconstruction of dark sector interactions. Phys. Rev. D, 104(4):043515, 2021.
- [237] R. von Marttens, L. Lombriser, M. Kunz, V. Marra, L. Casarini, and J. Alcaniz. Dark degeneracy I: Dynamical or interacting dark energy? Phys. Dark Univ., 28:100490, 2020.
- [238] B. Wang, E. Abdalla, F. Atrio-Barandela, and D. Pavon. Dark Matter and Dark Energy Interactions: Theoretical Challenges, Cosmological Implications and Observational Signatures. Rept. Prog. Phys., 79(9):096901, 2016.
- [239] D. Wang and X.-H. Meng. Improved constraints on the dark energy equation of state using gaussian processes. Physical Review D, 95(2):023508, 2017.
- [240] D. Wang, W. Zhang, and X.-H. Meng. Searching for the evidence of dynamical dark energy. Eur. Phys. J. C, 79(3):211, 2019.
- [241] G.-J. Wang, X.-J. Ma, S.-Y. Li, and J.-Q. Xia. Reconstructing functions and estimating parameters with artificial neural networks: A test with a hubble parameter and sne ia. apjsupp, 246(1):13, 2020.
- [242] Y. Wang, L. Pogosian, G.-B. Zhao, and A. Zucca. Evolution of dark energy reconstructed from the latest observations. Astrophys. J. Lett., 869:L8, 2018.
- [243] Y. Wang, L. Pogosian, G.-B. Zhao, and A. Zucca. Evolution of dark energy reconstructed from the latest observations. The Astrophysical Journal Letters, 869(1):L8, 2018.
- [244] H. Wei, X.-P. Yan, and Y.-N. Zhou. Cosmological applications of pade approximant. Journal of Cosmology and Astroparticle Physics, 2014(01):045, 2014.
- [245] E. Witten. Anti-de Sitter space and holography. Adv. Theor. Math. Phys., 2:253–291, 1998.
- [246] T. Wrase and M. Zagermann. On Classical de Sitter Vacua in String Theory. Fortsch. Phys., 58:906–910, 2010.
- [247] T. Yang, Z.-K. Guo, and R.-G. Cai. Reconstructing the interaction between dark energy and dark matter using gaussian processes. Physical Review D, 91(12):123533, 2015.

- [248] T. Yang, Z.-K. Guo, and R.-G. Cai. Reconstructing the interaction between dark energy and dark matter using Gaussian Processes. Phys. Rev. D, 91(12):123533, 2015.
- [249] W. Yang, E. Di Valentino, S. Pan, A. Shafieloo, and X. Li. Generalized emergent dark energy model and the hubble constant tension. arXiv preprint arXiv:2103.03815, 2021.
- [250] W. Yang, A. Mukherjee, E. Di Valentino, and S. Pan. Interacting dark energy with time varying equation of state and the  $H_0$  tension. Phys. Rev. D, 98(12):123527, 2018.
- [251] W. Yang, S. Pan, E. Di Valentino, E. N. Saridakis, and S. Chakraborty. Observational constraints on one-parameter dynamical dark-energy parametrizations and the  $h_0$  tension. Physical Review D, 99(4):043543, 2019.
- [252] W. Yang, S. Pan, O. Mena, and E. Di Valentino. On the dynamics of a dark sector coupling. JHEAp, 40:19–40, 2023.
- [253] W. Yang, S. Pan, L. Xu, and D. F. Mota. Effects of anisotropic stress in interacting dark matter – dark energy scenarios. Mon. Not. Roy. Astron. Soc., 482(2):1858–1871, 2019.
- [254] Y. Yang and Y. Gong. The evidence of cosmic acceleration and observational constraints. Journal of Cosmology and Astroparticle Physics, 2020(06):059, 2020.
- [255] G. Ye and Y.-S. Piao. Is the Hubble tension a hint of AdS phase around recombination? Phys. Rev. D, 101(8):083507, 2020.
- [256] H.-R. Yu, S. Yuan, and T.-J. Zhang. Nonparametric reconstruction of dynamical dark energy via observational hubble parameter data. Physical Review D, 88(10):103528, 2013.
- [257] W. Yu-Ting, X. Li-Xin, L. Jian-Bo, and G. Yuan-Xing. Reconstructing dark energy potentials from parameterized deceleration parameters. Chin. Phys. B, 19:019801, 2010.
- [258] M. A. Zadeh, A. Sheykhi, and H. Moradpour. Ghost dark energy with sign-changeable interaction term. Int. J. Theor. Phys., 56(11):3477–3495, 2017.
- [259] Y. Zhai, W. Giarè, C. van de Bruck, E. Di Valentino, O. Mena, and R. C. Nunes. A Consistent View of Interacting Dark Energy from Multiple CMB Probes. 3 2023.
- [260] C. Zhang, H. Zhang, S. Yuan, S. Liu, T.-J. Zhang, and Y.-C. Sun. Four new observational  $h(z)$  data from luminous red galaxies in the sloan digital sky survey data release seven. Research in Astronomy and Astrophysics, 14(10):1221, 2014.

- [261] G.-B. Zhao, M. Raveri, L. Pogosian, Y. Wang, R. G. Crittenden, W. J. Handley, W. J. Percival, F. Beutler, J. Brinkmann, C.-H. Chuang, et al. Dynamical dark energy in light of the latest observations. Nature Astronomy, 1(9):627–632, 2017.
- [262] S.-Y. Zhou, E. J. Copeland, and P. M. Saffin. Cosmological Constraints on  $f(G)$  Dark Energy Models. JCAP, 07:009, 2009.